9-15-2016 12:00 AM

Microstructural Geochronology of Zircon Across the Central Uplift of the Vredefort Impact Structure, South Africa

Connor Lawrence Davis
The University of Western Ontario

Supervisor
Dr. Desmond Moser
The University of Western Ontario

Graduate Program in Geology
A thesis submitted in partial fulfillment of the requirements for the degree in Master of Science

Abstract

The Vredefort central uplift, or ‘dome,’ represents the erosional remnant of one of the largest (~300 km diameter) and oldest (~2.020 Ga) terrestrial impact structures. This investigation was performed to help elucidate the complexity of the shock process on zircon, incorporating various electron beam methods, including BSE and SE imaging, EBSD, CL, and EDS (mapping and semi-quantitative compositional analysis). A new shock microstructural progression in terrestrial zircon is suggested, as well as a complete structure-wide analysis of impact melt inclusions in zircon. Regional trends in the effects of shock on zircon are included. Impact melt glass inclusion compositions vary widely, from felsic to mafic inclusions, and are related to the partial melting of local minerals. This study is significant for the future study of similar impact structures on other rocky planets, and the quantification and qualification of shock conditions as recorded in zircon.

Keywords

Vredefort impact structure, zircon, impact melting, shock microstructures, shock metamorphism, impact melt glass inclusions.

Acknowledgments

First and foremost, I would like to acknowledge Desmond Moser for his incredible support and guidance over the past two years. His passion and insight into the geology of Vredefort has been invaluable to the success of my thesis. I sincerely thank Des for providing me the opportunity to do field work in South Africa, and for all the other opportunities to attend conferences, field camps, and extracurricular courses. Thank you also for the help in editing and tying this thesis together.

I would also like to thank Ivan Barker, who's technical assistance in the ZAPLab was instrumental to my success. Thank you for putting up with my questions, and always being there to help me figure out the numerous issues we encountered.

I appreciate the help of the ASTRO-CSA group for funding some of my conference travel, such as the ASTRO short course in Edmonton, AB. I am also thankful for all the other field trips I was a part of, including Oman, southwest U.S., and across Canada. It was the opportunities like this that truly made my graduate experience.

I thank the members of my thesis defense committee, Sean Shieh, Robert Klassen, and Kim Tait, for their efforts in critiquing my thesis. Thank you also to the defense chair, Bill Church.

I could not have gotten through the last two years without the support of my friends and family. Thank you to my family, Rita, Jim, and Corrin, whose support has been so important to me. Thank you to all my fellow graduated (and soon to be) Western friends, specifically Marcus, Taylor, and Diego, as well as many others. The practical jokes will never be forgotten. And finally, thanks, Obama, for providing the inspiration to rise above and prove your harshest critics wrong (Diego).

Table of Contents

List of Tables

List of Figures

List of Appendices

Chapter 1

1 Introduction

1.1 Introduction

A fundamental principle of geology is that Earth was formed from gradual, endogenic processes occurring over an appreciable amount of geological time. This concept, aptly named uniformitarianism, was proposed by James Hutton in 1785, and later popularized by Charles Lyell. Starkly distinguishable from catastrophism, the popularity of uniformitarianism pushed the scientific community away from the study of catastrophic processes such as impact cratering. It may come as some surprise, then, that Alfred Wegener (the architect of the plate tectonic theory, a distinctly gradual process) was one of the first to publish his belief that the familiar craters on the lunar surface were of an exogenic, impact origin (Wegener, 1921). Still, it was not until relatively recently that impact cratering, and catastrophism as a whole, became recognized by the geological community as a significant contributing process to the formation of the inner solar system. This relatively newfound interest has been encouraged by the notion that large impacts have also played an important role in Earth's biological evolution, as demonstrated by the temporal relation between Mexico's Chicxulub impact structure and the Cretaceous-Paleogene (K-Pg), formerly known as the Cretaceous-Tertiary (K-T) boundary extinction (Alvarez et al. 1980; Hildebrand et al. 1991; Vellekoop et al. 2014). The key linkage between the boundary layer and the location of the impact crater was established with dating of shocked zircon (Krogh et al., 1993).

Impact craters are roughly circular depressions in the surface of a solid planetary body, formed instantaneously by the hypervelocity impact of a cosmic projectile impacting a

solid target (French, 1998). Often confused with volcanic craters, impact craters are differentiated by their raised outer rims, and a crater floor that is lower than the nearby unaltered terrain. While impact craters may be easily recognizable on extraterrestrial bodies such as the Moon, Mars and Mercury, significant tectonic and erosional activity on Earth has masked many of the visual macro-scale indicators of an impact crater. Predominantly due to extensive ocean cover (over 70% of the Earth is covered by water), and the adverse effects of tectonics and erosion, there are only 188 confirmed impact craters on Earth, situated primarily on the stable cratons of the Americas, Australia, and Europe. Additionally, many of these craters are very young, such as the ~49 kyr Meteor Crater, near Flagstaff, Arizona. The recent development of satellite imagery has contributed greatly to the discovery of many new impact craters on Earth, however diagnostic microstructural features are often the best way to confirm the presence of an impact crater.

The precise chronology of impact events on planetary surfaces has implications for the understanding of crustal and bio-evolution on Earth and other planetary bodies. U-Pb isotopic dating of minerals such as zircon has proved valuable in the pursuit of an improved impact chronology, as sufficient shock damage and heating can cause up to 100% Pb-loss while preserving microstructures diagnostic of specific shock environments (Moser et al., 2011). Fitting such minerals into their corresponding crater setting (*in-situ*) is also important to the success of crater studies. Unfortunately, exploration projects to study craters on planetary bodies other than Earth are not currently feasible. With the exception of rare meteorite finds and sample returns, it is very difficult to determine how they relate to their genetic extraterrestrial impact environment(s).

Terrestrial analogues are therefore quite useful to establish a calibration set for the effects of cratering processes on minerals that can be applied in the rest of the inner solar system. The Vredefort impact structure, South Africa, is a unique terrestrial analogue site. Its size and morphology provide the best insight into the types of large, complex impact events that played a role in the crustal evolution of planetary bodies in the state of the inner solar system.

1.2 The importance of impact cratering

The evolution of the inner solar system has been immensely affected by impact cratering, largely relating to a period of heavy bombardment early in Earth's history (Late Heavy Bombardment (LHB) ca. 3.9 Ga) (Ryder et al., 2000). It has been suggested that the Earth would have experienced many more impacts than the lunar surface (Koeberl et al., 2006), possibly as many as 1.3-1.5 times the impacts per unit area (Frey, 1980). Impact-driven crustal evolution is responsible for the terrestrial surface we observe today, including the origin of the dichotomy between the lower density continental and higher density oceanic crust that is now maintained by modern plate tectonics (Frey, 1980). Biologically, this intense period of impact cratering would have had significant effects as well. Despite the obvious negative aspects of bombardment (i.e. impact-driven mass extinction), it is believed that impacts also produced thermophilic niches that eventually gave rise to the beginning of life on Earth (Pace, 1997). The early atmosphere was presumably affected by a high impact flux during the LHB (Ahrens, 1993). Of course, making assumptions about processes that would have shaped the crustal and biological profile of Early Earth is relatively difficult without a rock record. This is why we look to other rocky surfaces, especially ones which are smaller and thus, less likely to have large-scale resurfacing due

to erosion or tectonism. Two prime examples are the lunar and Martian surfaces, where the increased impact record provides an exceptional insight into the processes that would have shaped the Early Earth. In fact, the very existence of the Moon is believed to be the product of a collision between a Mars-sized impactor and Earth (Canup and Asphaug, 2001). Understanding the timing and magnitude of impacts on Earth is vital to piece together the development of our inner solar system.

1.3 The impact cratering process

Impact cratering is a very complex process which is regionally and locally heterogeneous.

This complexity is an important factor to consider when analyzing any data related to impact cratering. Outlined in this section is a description of the major stages in the progression of the impact cratering process.

1.3.1 The shock wave

The impactor generally does not penetrate very deeply in the target, perhaps penetrating ~1-2 times its diameter, dependent primarily upon on the impacting velocity and target rock composition (Kieffer and Simonds, 1980; O'Keefe and Ahrens, 1982; Melosh, 1989). After the projectile has ceased its downward movement, the energy from the initial impact is released as intense shock waves, which propagate radially throughout the target rock at high velocities. The kinetics of the shock wave are illustrated in Figure 1-1, below. The stages listed in the sections below are the product of the propagation of the shock waves and the resultant modification effects of the unstable crater.

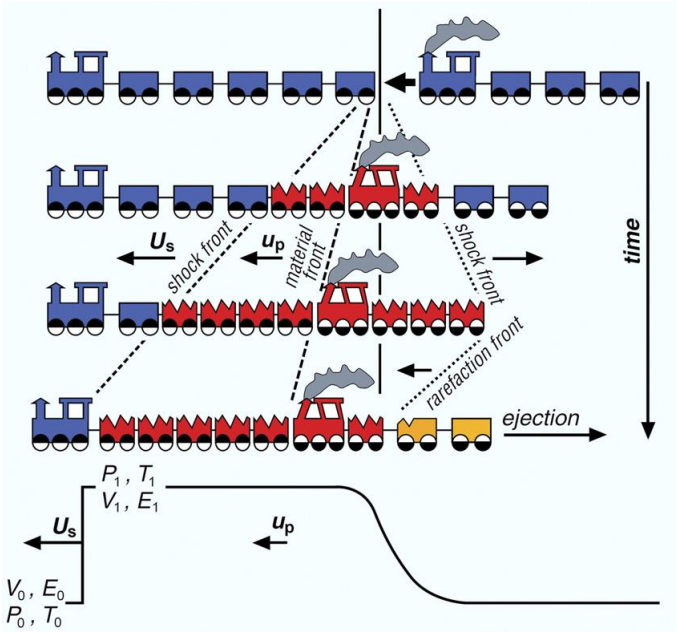

Figure 1-1: A visual aid used to describe the progression of a shock wave. The two blue trains are used to show the target and impactor, which, upon collision, releases a roughly hemispherical shock wave, known as the shock front. This shock front travels through the target, subsequently moving the material front forwards. The shock front also moves backward into the impactor, until it reaches the other side of the impactor, where it transforms into a rebounding rarefaction front that acts to decompress the impactor and target material, leading to the vaporization, melting, and ejection of that material (Langenhorst, 2002).

1.3.2 Stage 1: Contact and Compression

Stage 1 commences immediately at the moment of contact between the impacting projectile and its target. As mentioned above, the projectile is unable to penetrate more than 1-2x its diameter, and instead generates shock waves (Kieffer and Simonds, 1980; O'Keefe and Ahrens, 1982, 1993; Melosh, 1989). Once the shock waves reach the top of the projectile, they rebound or reflect off the surface and return as a rarefaction wave. These rarefaction waves act to rapidly decompress the projectile, explaining why the projectile is often completely melted or vaporized and solid remnants are rarely found

(French, 1998). The primary shock front, which may have original shock pressures of up to or exceeding 100 GPa, attenuates quickly with distance; a result of both the decrease in shock density with increasing hemispherical area upon expansion as well as the energy lost to the target rocks through deformation and heating (French, 1998). A record of the energy lost from the shock waves is often preserved as shock features.

At a distance defined primarily by the target rock composition and original shock wave velocity, the shock waves will transform into elastic or seismic waves, travelling approximately at the speed of sound (~5-8 km/s) and with pressures of ~1-2 GPa, which are low enough to not cause significant shock transformation (Kieffer & Simonds, 1980). The contact and compression stage ends when the release or rarefaction wave has passed through the projectile and is at the contact between the projectile and the impacted surface. This entire process typically takes a fraction of a second, even for large, complex impact events (Melosh, 1989).

1.3.3 Stage 2: Excavation

The excavation stage commences directly after the completion of the contact and compression stage. The excavation stage can be described as the stage where the crater is actually formed, developing due to a number of complicated interactions between the propagating shock and rarefaction waves and the original target surface (Melosh, 1989; Grieve, 1991). For example, the reflected wave from the contact and compression stage is converted into kinetic energy, which causes the affected rock to accelerate outwards as an excavation flow. As long as the energy is high enough, the crater will expand to sizes of up to 20-30x the size of the original projectile (French, 1998). Once the energy is low enough such that excavated debris is not able to reach past the developing crater rim, the

excavation stage ends, and the near surface rocks are uplifted to form the crater rim. For large craters (~200 km, in the realm of the size of Vredefort), this stage takes about 90 seconds to complete (Melosh 1989; French 1998).

1.3.4 Stage 3: Modification and collapse

As soon as the transient crater has reached its maximum diameter, the modification stage commences. The beginning of the modification stage occurs when the expanding shock waves transform into lower pressure elastic waves, forming the transient crater rim (French, 1998). The degree of modifications to the transient crater is primarily a function of the planet's gravity and size of the transient crater itself. The most significant parts of the modification stage, where the major structural transformations occur, typically take less than one minute for small structures and as little as a few minutes for larger structures (Melosh, 1989). Major post-impact modifications in a small, simple impact crater are relatively absent, leaving the transient crater structure well preserved. In larger complex craters, however, post-impact modifications are quite dramatic. Driven by gravity, two primary modifications occur: the in folding and collapse of crater wall rocks, mostly by down-faulting to infill the transient crater; and the uplift of rocks in the center of the structure, called the central uplift. The end of the modification stage is difficult to determine, as post-impact modifications can continue for millions of years, however this stage is typically considered to be the time when the majority of the bulk of the structural changes have completed in the seconds to minutes after impact.

1.3.5 Types of impact craters

When a meteorite impacts a solid surface, it first creates a bowl-shaped depression. Mainly dependent upon impact velocity, impactor size, and surface geology, this bowl-

shaped depression has the ability to transform into a much larger structure, or remain relatively unmodified.

A. Simple Craters

The formation of a simple crater involves only minor transformations from the original transient crater. Typically, these transformations will involve collapse of the steep upper walls of the crater, and by re-deposition of ejected crater debris (French, 1998). This collapse may increase the measured diameter of the crater by up to 20%, however, the depth of the transient crater remains essentially unchanged (Melosh, 1989). Dependent primarily upon the target material and gravity, simple craters are typically small in diameter, often less than between 2 km (for sedimentary target rocks) and 4 km (for crystalline targets) on Earth (Grieve, 1987). An example of a simple crater on Earth is Meteor Crater, shown in Figure 1-2.

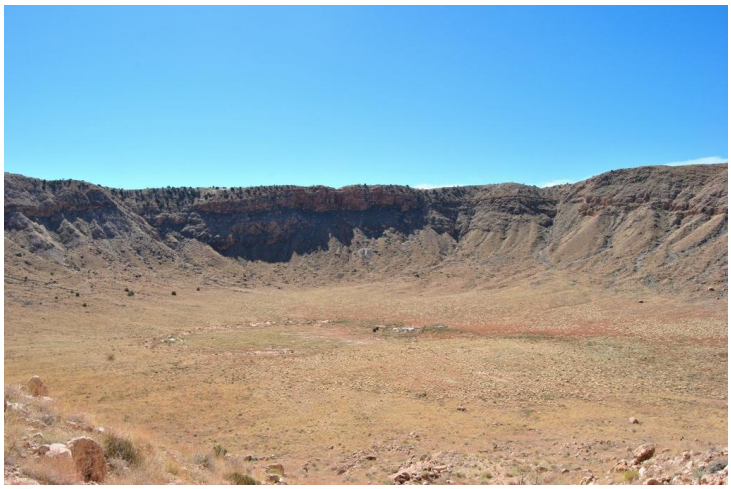

Figure 1-2: Example of a simple crater at Meteor Crater, Arizona. Note the absence of a prominent central uplift and the relatively small diameter of the crater. Photo taken in October, 2014 (C. Davis).

B. Complex Craters

Above the transition diameter (Grieve, 1987), a transient crater will collapse in a much more dramatic and extensive fashion than that of a simple crater. This transformation is characterized by the upheaval and exhumation of the deep, central target and the collapse of the outer rim, creating unique features such as a prominent central uplift, extensive and shallow crater floors, and terraced walls, as seen in Figure 1-3. Another distinguishable feature of a complex impact crater is the presence of a cohesive impact melt sheet, as seen in many large impact craters on Earth. This melt sheet, however, is often missing in ancient impacts due to preferential erosion.

At the intermediate sizes, the central uplift of a complex crater reaches its maximum stable height, thus collapsing and forming what is known as a peak-ring basin. A peak-ring basin is the transitional stage between typical complex craters and multi-ring basins (Baker et al., 2011). For the largest complex craters, these “peak rings basins” fade from prominence, transitioning into multi-ring basins.

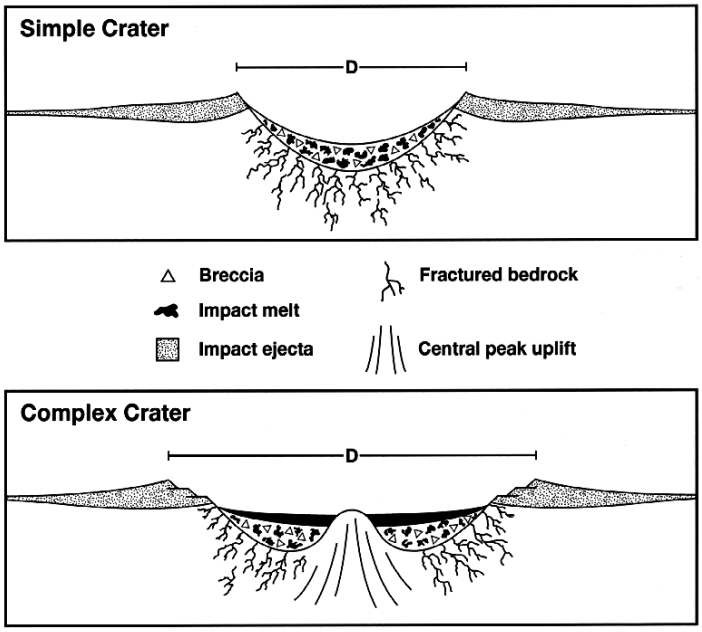

Figure 1-3: Simple crater vs. complex crater morphology (NASA, 2004).

1.3.6 Impact Melting

A common characteristic of most simple and complex impact craters is the presence of a cohesive melt sheet, melt glass spherules (tektites, etc.), or melt injection dykes (Osinski et al., 2013). Impact melt sheets have been documented at ~60% of terrestrial impact craters (Grieve et al., 1977), and are presumed to have been present at more craters if not for the adverse effects of erosion. Impact-related melting is invariably related to unloading (decompression) of intense shock pressures and temperatures related to the shockwave (Grieve et al., 1977). This decompression occurs upon passage of the rarefaction wave mentioned previously. Figure 1-4 displays the P-T conditions necessary for complete shock melting in comparison to normal crustal metamorphism conditions and common polymorphs and shock features. A standard impact melt rock should bear no shock deformation features, and is often quite homogeneous. For example, the Vredefort Granophyre represents an impact melt rock (Koeberl et al., 1996). It should be noted that

partial melting has been related to the impact process as well, and can occur at lower P-T conditions than those shown in this figure. Macro-scale evidence of impact-related partial melting at Vredefort is seen at the Central Anatectic Granite, which represents partial melt of the surrounding ILG host rock (Gibson et al., 1997; Cupelli et al., 2014).

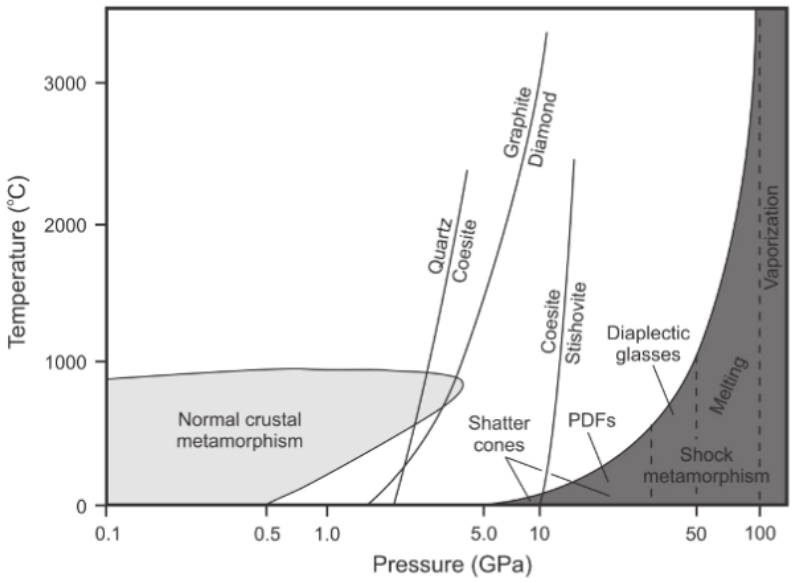

.

Figure 1-4: P-T plot displaying the shock pressure and temperatures necessary for shock melting, in comparison with 'normal crustal metamorphism.' (Osinski & Pierazzo, 2013).

1.4 The Vredefort impact structure, South Africa

The Vredefort impact structure (S27°0', E27°30') is located approximately 120 km southwest of Johannesburg, South Africa (Fig. 1-5). Estimates place the original crater at approximately 250-300 km wide (Therriault et al, 1997), and 2.020 Ga (Spray et al., 1995; Kamo et al. 1996). The original crater would have been the largest, and second oldest (only to the ~2.400 Ga Suavjärvi Crater in Russia) on Earth. What remains, aptly named the Vredefort dome, is the ~90 km wide remnant of the central uplift of that original, eroded structure. The presence of this central uplift deems Vredefort a complex

crater, and it has been suggested that Vredefort represents one of the few multi-ring basins remaining on Earth (Grieve et al., 1981). Estimates suggest that the rocks of the central uplift have been exhumed from a depth of up to 36 km, based on exposure of both Precambrian and Archean rocks (Moser et al., 2001; Hart et al., 2004). Further study by Tredoux et al. (1999) discovered the presence of ~3.5 Ga mantle ultramafic at the center of the impact, thus promoting the ~36 km "crust on edge" model. The "crust on edge" model proposes that a radial traverse from the collar to the core of the dome represents a journey through progressively deeper sections of the Archean crust. The estimated degree of erosion based on geobarometric studies of between 7-10 km (Stevens et al., 1997; Gibson et al., 1998), also allows for a unique view into the roots of a giant impact structure. Figure 1-6 provides a visual depiction of the Vredefort area pre-impact, directly post-modification, and at the currently accepted estimates of erosion.

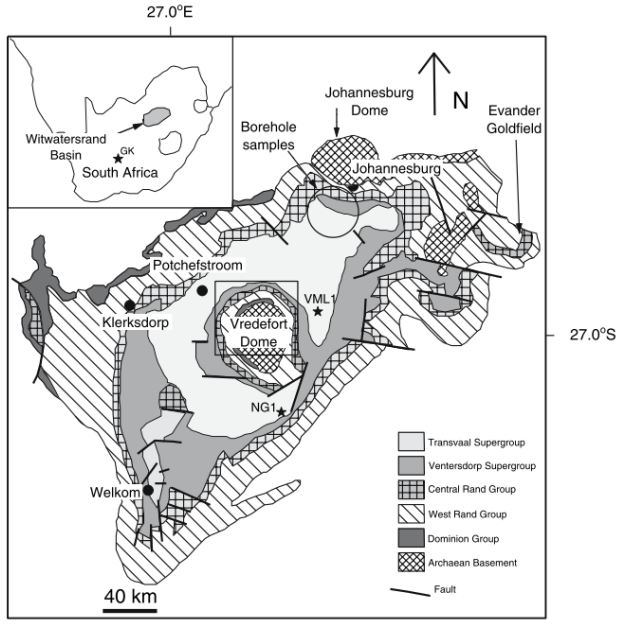

Figure 1-5: Map indicating the location of the Vredefort dome within the greater Witwatersrand Basin (Fagereng et al., 2008).

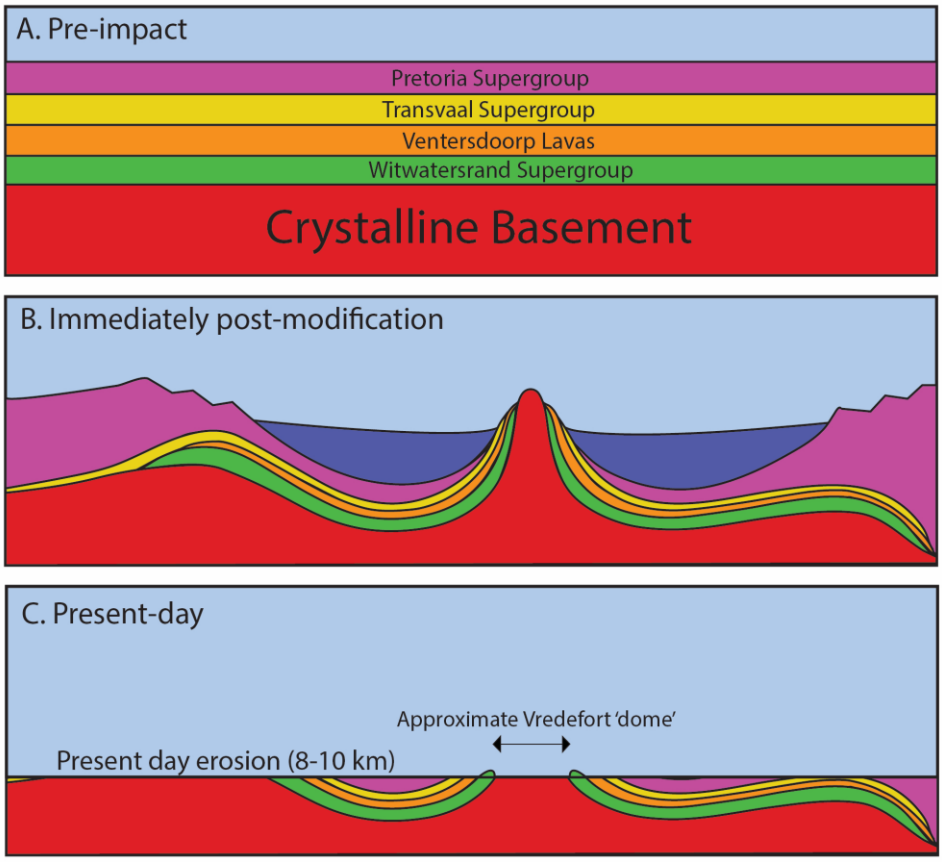

Figure 1-6: A visual depiction of local geology at the site of the Vredefort impact A) pre-impact (pre-2.020 Ga), B) immediately after modification (~2.020 Ga), and C) at the present level of erosion. Stratigraphic units are not to scale, and these images are only to be used as a rough guide. Images modified from Oggmus (2014).

1.4.1 Geology of the Vredefort central uplift or 'dome'

The Vredefort dome is the ~90 km wide central uplift left behind from the post-impact rebound of Archean crystalline basement rocks from the original transient crater floor. The dome itself is comprised of an ~40 km wide core of Mesoarchean gneisses (from the Archean Basement Complex), as well as an ~20-25 km outer collar of topographically high metasediments and metavolcanics (Henkel & Reimold, 1998). The southeastern portion of the dome is completely covered by ~300-180 Ma Karoo sediments and dolerite sills, and general exposure of the impact structure is quite limited throughout the entire

dome (Henkel & Reimold, 1998). The gneisses in the center of the dome have been metamorphosed to amphibolite to granulite facies, and can be further divided on the basis of geochemical studies (Hart, 1978; Stepto, 1990) and metamorphic grade, into the Outer Granite Gneiss (OGG) and Inlandsee Leucogranofels (ILG).

Single-zircon U-Pb dating (Kamo et al., 1996) and 40^{Ar} - 39^{Ar} dating of an OGG amphibolite (Reimold et al., 1992) from the core of the dome indicated that the Archean core is between 3.2 and 3.1 Ga, and underwent a stage of metamorphism at ~3.08 Ga. There is a component of granitoid that is approximately 3.3-3.4 Ga, as indicated by U-Pb zircon dating by Armstrong et al. (2006). The OGG region is typified by amphibolite grade migmatitic gneisses, typically of granodioritic, adamellitic, and tonalitic composition (Hart, 1978; Stepto, 1990). The OGG is thought to represent the middle to upper crust. The ILG region is defined by granulite grade metamorphism, comprising the inner annulus of the crystalline core. The gneisses of the ILG are typically strongly banded and often folded, felsic, tonalitic gneisses (Hart, 1978; Stepto, 1990). An early theory that the ILG represented portions of an impact melt that was subsequently crystallized was disproved based on the lack of a considerable Ni values in the leucogranofels that would have provided evidence of a meteoritic component (Palme, 1980; Schreyer, 1983). The ILG rocks are often found to have an overprinting granophyric texture, displaying an intergrowth of feldspar and quartz formed as a direct result of a cotectic or eutectic crystallization from a melt (Schreyer, 1983). At the same time, the ILG is well-known for its intensely recrystallized grains and glomerogranular quartz texture that nevertheless decorates rather than erases the dm-scale compositional layering and gneissic fabric of their Archean protolith (Reimold & Gibson, 2010). The

interesting spatial relationship between granophyric textures and fabric unit textures in the ILG rocks suggests that they contained a component of granitic melt formed by anatectic melting within the ILG host rocks (Schreyer, 1983). A large-scale surface expression of this partial melting, called the Central Anatectic Granite, can be found near the Inlandsee Pan (Hart et al., 1991). Near the center of impact, within the ILG zone, borehole drilling exposed serpentinized amphibole-bearing harzburgite of 3.3-3.5 Ga (Tredoux et al., 1999). When combined, the evidence indicates a "crust-on-edge" model, with the OGG representing middle-upper crust, the ILG representing lower crust, and harzburgites in the core representing possible Archaean upper mantle material (Hart et al., 1990; Tredoux et al., 1999; Hart et al., 2004). This evidence signifies that the exposed central uplift of the dome uplifted rocks from the lower crust, comparable to some of the large impacts on other planetary bodies.

The transition zone between the OGG and ILG has been the subject of numerous formation propositions. Fletcher & Reimold (1989) proposed that the transition zone represented a mega-shear zone, while Hart et al. (1990) calls the transition zone the Vredefort discontinuity, asserting that the abutment of the OGG and ILG terranes represents the upper and lower crust, respectively. More recently, it was suggested that this transition likely resembles that of a more gradual change in lithologies rather than a structural discontinuity, demonstrated by the melt-rich amphibolites and melt-depleted granulites created during the high-grade metamorphic event at ~3.09-3.08 Ga (Gibson & Reimold, 1996; Hart et al., 1999; Lana et al., 2003, 2004). This is what would be expected by a traverse from upper to lower crustal levels (Reimold & Koeberl, 2014).

Exposed along the northwestern, western, northeastern, and northern arcs of the Vredefort dome are the subvertical to overturned collar rocks. These metasedimentary and metavolcanic rocks have the same general geology as the rest of the Witwatersrand Basin, shown in Figure 1.5. The strata of the collar can be divided into the basaltic andesites, felsic lavas, and rift-related clastic sediments of the Dominion Group (~3074 ± 6 Ma, Armstrong et al., 1991), overlain by the clastic sediments of the Witwatersrand (~2.97-2.71 Ga, Robb et al., 1997; Robb and Robb, 1998; McCarthy et al., 2006), the tholeiitic flood basalts of the Ventersdorp (~2.714 Ga, Armstrong et al., 1991), and the shales, dolomites, and volcanics of the Transvaal Supergroup (~2.5-2.25 Ga, Walraven et al., 1990). Subsidiary intrusions, possibly related to the Bushveld event at ~2.06 Ga, also intrude the collar rocks (i.e. Schurwedraai) (Gibson & Reimold, 2008). At the contact of the core and collar, the collar strata are upturned 80 degrees (and overturned in places), and at 50 degrees at areas higher in the Witwatersrand sequence (Lilly, 1980).

The entire region was overprinted by a later metamorphic event induced by the Kibaran orogeny ca. 1.110-1.021 Ga. This event is the cause of U-Pb resetting in some zircons yielding a younger, secondary ~1.0 Ga age (Moser et al., 2011).

1.4.2 Evidence of an impact origin for Vredefort

The origin of the Vredefort impact structure was a hotly debated topic for quite some time, outlining the difficulties in early studies of impact craters. Early work by the likes of Shand (1916), Hall & Molengraaff (1925), Nel (1927), and Boon & Albritton (1936) proposed a possible impact origin for Vredefort, and their work gained some traction when Daly (1947) reiterated their findings, placing an estimate of minimum structure diameter at approximately 50 km. However, the origin of Vredefort remained enigmatic

for quite some time. Many suggested that the crater was endogenic, forming from one of or a series of mantle explosions (Nicolaysen et al., 1963). Many of the early studies focused on the macro-evidence of impact cratering. Fortunately, as science and technology have evolved, so too has the ability to identify key indicators of shock on the micro-scale. Evidence which is often invisible to the naked eye is now being used in the forefront of identifying impact craters and ejecta layers across the world, and was used to verifiably attribute the formation of the Vredefort dome to a hypervelocity impact.

In order for a transient crater the size of Vredefort to form, there must be an immense amount of energy released upon impact from a hypervelocity bolide. The impact instantaneously transforms the consolidated target rock into the rheology of a Bingham fluid (Morgan et al., 2000). This incredible energy release also creates many macroscopic and microscopic shock features that are indicators of a shock event. Some of these impact features at Vredefort are shown in Figure 1.7 and include but are not limited to: planar features in quartz that turned out to be distinctive planar deformation features (Carter, 1965, 1968; French, 1972; Grieve et al., 1990; Leroux et al., 1994) (Fig. 1-7a); granophyre with a meteoritic component demonstrated by increased siderophile-element abundances (Koeberl et al., 1996) (Fig. 1-7b); pseudotachylite (Shand, 1916; Killick & Reimold, 1990; Schwarzman et al., 1983; Reimold & Colliston, 1992) (Fig. 1-7c); foliated norite impact melt rocks (Moser, 1997); possible impact ejecta in the form of spherules found in Russia (Huber et al., 2014)(Fig. 1-7d); shatter cones (Hargraves, 1961; Dietz, 1961)(Fig. 1-7e); zircon crystallized from impact norite (Moser, 1997) (Fig. 1-7f) and high-pressure quartz phases such as coesite and stishovite (Martini, 1978; Martini, 1991). The presence of these features now substantiates earlier exogenic origin claims

with irrefutable evidence that is not solely based on the circular shape of the structure or overturned strata observations in the collar (Boon & Albritton, 1936).

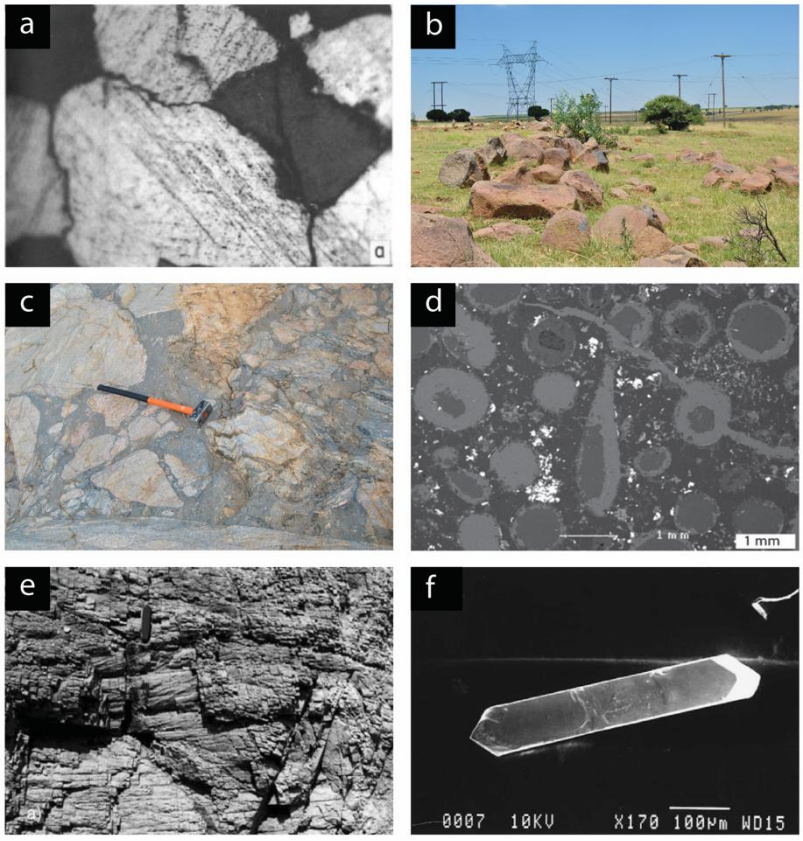

Figure 1-7: Shock evidence at Vredefort, including: a) petrographic image of quartz PDF's (Grieve et al., 1990), b) granophyre (Davis, 2014), c) pseudotachylite (Davis, 2014), d) BSE image of impact ejecta spherules (Huber et al., 2014), e) shattercones (Hargraves, 1961), and f) newly crystallized zircon from impact-related norite (Moser, 1997).

1.4.3 Shock microstructures in quartz and other minerals

Often the most useful indicator of a shock event are the shock microstructures contained in rock-forming and accessory minerals. Microstructures have been documented extensively in minerals throughout impact structures, including Vredefort, Chicxulub, and Sudbury. Early microstructural studies of minerals at Vredefort focused primarily on

rock-forming shock-indicator minerals such as quartz and feldspars. Planar features (later named planar deformation features (PDF's)) in quartz were shown to be extensively present across the Vredefort dome by Carter (1965, 1968). Lilly (1981) noted that there was a correlation between estimated shock pressures and the average sets of planar deformation features per grain, based on the shock pressure calibration system of Robertson (1975) and Grieve & Robertson (1976). He also noted that there was an increase in the degree of recrystallization in quartz moving from the collar to the core, typical of increased shock temperature gradients. The confusion imposed by the troublesome quartz planar features led Lilly (1981) to propose multiple shock events associated with some form of a cryptoexplosion event. Grieve et al. (1990) reconciled the controversy suggesting that the relative lack of planar deformation features (Grieve et al., 1990a-shocked minerals and K/T controversy) in quartz from the core was due to post-impact recrystallization due to high post-shock temperatures. This recrystallization was present extensively in the core of the impact, leading to the skewed and confusing shock pressure calculations. His conclusion, however, led to another problem; quartz, although fairly refractory, was often overprinted by metamorphism and/or alteration, making it unreliable as a shock indicator. Leroux et al. (1994) subsequently confirmed the presence of impact-induced planar features in quartz that are locally overprinted by the post-shock annealing effects of high temperatures. In some cases, remnants of planar elements in the quartz hosted trails of fluid inclusions, thought to be annealed planar deformation features. Because of the moderate susceptibility of quartz and feldspars to erosion, annealing, and recrystallization, a better shock indicator mineral was necessary.

1.5 Zircon

Zircon ($ZrSiO_4$) is a highly refractory and chemically inert nesosilicate mineral, making it extremely resilient to weathering, transport, and intense metamorphism. Zircon is also quite common in the Earth's crust, as it forms ubiquitously in silicate melts which are the foundation of igneous rocks. These characteristics have allowed zircon to become an important tool in determining geological history, including various igneous and metamorphic episodes that the mineral has recorded. These episodes include primary crystallization, secondary igneous crystallization, and metamorphic recrystallization, allowing for a single zircon to contain individual parts of a crystal with entirely different origins (Hinton & Upton, 1991). This is especially true for shocked zircons, which are known to recrystallize under high post-shock temperatures (Bohor et al., 1993; Kamo et al., 1996).

Zircon has two different cation substitution sites, including a tetragonal and a triangular dodecahedral site, hosting Si and Zr, respectively (Speer, 1980). Chemically, zircons are quite elementary, with ZrO_2, HfO_2, and SiO_2 making up the majority of the oxide component. Hafnium is always present in some respect, acting as a substitute for Zr. A typical zircon does not have a significant amount of Hf, with HfO_2/ZrO_2 ratios on the order of 0.01, and metamict varieties having slightly more (Rankama & Sahama, 1950).

Much of the effectiveness of zircon in piecing together geological history is related to the mineral's ability to act as an incredibly accurate and superior geochronometer. Although many minerals have been used as reliable shock indicators, including quartz and feldspars, they are far less refractory than zircon, and are at a significant disadvantage for use in geochronometry. Zircon has the ability to both preserve shock microstructures and

primary and secondary U-Pb ages, effectively dating the event that generated the shock microstructures.

1.5.1 Shock microstructures in zircon

Shock microstructures in zircon were first described by Krogh et al. (1984). Many of these microstructures have been found to survive billions of years of erosion (Cavosie et al., 2010), tectonism and metamorphism, even up to granulite facies. A number of zircon microstructures have been used as diagnostic indicators of shock metamorphism, including planar and curviplanar features/fractures (Moser et al., 2011), granular zircon (Bohor et al., 1993), decomposition of zircon to its oxide constituents baddeleyite and silica (El Goresy, 1965; Kleinmann, 1968; Glass et al., 1990), the presence of high-pressure zircon polymorph reidite (Cavosie et al., 2015), and microtwinning (Moser et al., 2011; Erickson et al., 2013). It has, conversely, also been suggested that the presence of planar and curviplanar fractures are, in fact, not diagnostic of a shock environment, and that these microstructures may also be indicative of a highly seismically active area (Kovaleva et al., 2015). The question of whether these planar and curviplanar fractures are similar to the previously accepted diagnostic planar and curviplanar fractures is still to be determined. A comprehensive overview of the progression of shock microstructures in zircon from the Vredefort dome (Moser et al., 2011) revealed the following 5 phases: 1) planar fracturing in {1K0} and {1K2} due to initial shock compression; 2) curviplanar fractures in {1K1} that have been annealed and now host melt glass inclusions; 3) microtwins oriented 65° about [110] due to rarefaction of the shockwave; 4) impact age crystallites recrystallized due to high post-shock heating by intruding impact melt; and 5) crystal plastic deformation associated with post-impact crater modification. Erickson et

al. (2013) were successful in correlating planar microstructures from exterior scanning electron images to submicron-scale transmission electron and electron backscatter diffraction images. Similar to Moser et al. (2011), they proposed the following chronology of shock microstructures: 1) c-axis parallel PF's (010) and (100), 2) four {112} PF's, some including microtwins, 3) curviplanar fractures and impact melt inclusions, 4) (011) PF's from compression, and 5) crystal plastic deformation. Krogh et al. (1984) established a link between shock microstructures in zircon and U-Pb systematics, where they attributed an ~1850 Ma isotopic disturbance to impact-induced planar microstructures at the Sudbury impact structure, Canada. This interpretation was reinforced with studies by Bohor et al. (1993), Moser et al. (2011) and Cavosie et al. (2015). Completely recrystallized zircon (granular/polycrystalline zircon), and zircon crystallized from impact melt have been identified as the best targets for complete U-Pb impact resetting (Moser et al., 2011; Cavosie et al., 2015). Zircons which are not recrystallized, but host microtwins, planar fractures, or low angle boundaries are commonly partially reset (Moser et al., 2011; Cavosie et al., 2015).

A significant setback in the progress of shock microstructural studies in zircon is the confusion over terminology. An attempt is made in this thesis to elucidate this confusion and provide a suggestion for a set of guidelines for the classification of terrestrial shock microstructures. For the purposes of this study, we recommend the following terminology:

A) Planar features: Defined as any crystallographically-controlled planar element in zircon. Planar features can be divided in the following ways:

a. Microtwins: Planar ‘features,’ which appear as a doublet of lamellae composed of zircon in twinned orientation relative to the surrounding crystal. Microtwins, oriented {112} have angle-axis pair values of 65° about [110] (Moser et al., 2011).
b. Planar fractures (PF’s)- Crystallographically-controlled planar elements that originally appear as open cracks or fractures in the zircon lattice. Planar fractures can be either:
    i. *Open: Completely open fractures that are not filled.*
    ii. *Closed: Infilled by melt, and commonly at least partially annealed. Very similar to curviplanar ‘features’ defined below.Referred to as annealed or filled-fractures.*
c. “Microcleavage”- Planar elements representing low angle boundaries (<10°) that remain closed, but are not filled by melt. ‘Microcleavage’ is similar to those described by Leroux et al. (1999).
d. Planar deformation bands (PDB’s): can be divided into two types:
    i. Kinks: PDB ‘kinks’ have been previously documented in zircon, however they have not been called ‘PDB kinks.’ They are displayed as small bars of colour change in EBSD misorientation maps, often associated with other planar features.
    ii. Twists: PDB ‘twists’ are a newly documented zircon microstructure that is described fully in Chapter 2. Tapered planar bands are referred to as ‘twists’ because of the twisted appearance in EBSD misorientation maps.

B) Curviplanar features-Through-going fractures that are not planar. In previous publications, these were referred to as ‘fractures,’ however because of the common infilling by impact melt and subsequent annealing, we recommend that they be called ‘features’. They should also be differentiated from NPF’s (Timms et al., 2012), which are not impact-related. Curviplanar features can be divided into two types for the purposes of this study:

   a. Closed (annealed) and in-filled by melt (IMG inclusions).
   b. Closed, but offsetting grain boundaries due to increased strain exerted on the zone of weakness.

C) Granular-textured zircon: Recrystallized zircon can be divided into three types for the purposes of this study:

   a. Fine-granular zircon: Identified as a decomposition feature of zircon (French, 1998). Often associated with decomposition to baddeleyite.
   b. Fine (ejecta-type) granular zircon- Similar to that identified by (Bohor et al., 1993; Timms et al., 2012), finer-scale granular zircon is induced by incredibly high instantaneous shock P/T conditions, rather than long-term exposure to high post-shock temperatures (as in coarse-granular zircon).
   c. Coarse-granular zircon- Identified in this study, coarsely granular zircon appears as polycrystalline zircon. This zircon recrystallizes into coarse granules under high post-shock temperatures common in the core of the Vredefort dome.

1.5.2 Melt inclusions in zircon

Melt inclusions in zircon are well-documented, and typically take the form of primary inclusions of silicate melt separated from the bulk melt during zircon crystallization (Thomas et al., 2003). These melt inclusions (MI's) have been found in zircon from various rock-types, such as gneisses, granitoids, basalts, and sandstones (Li, 1994; Chupin et al., 1998; Chesner, 1998). MI's are typically trapped at magmatic conditions, therefore capturing a glimpse of the original melt composition. A unique quality of zircon is that it has the ability to preserve these melt inclusions unlike any other mineral, meaning that zircon can often provide insight into original melt composition and evolution. The presence of melt inclusions in detrital zircons found in sandstones (Thomas et al., 2003) is especially remarkable because it displays the preservation potential of melt inclusions in zircon. Chupin et al. (1998) was even able to use MI's in zircon to correlate zircons to their host terranes, by studying melt compositions. Melt inclusions (MI's) in zircon have been described by Li (1994), Chesner (1998), Chupin et al. (1998), Hoskin and Black (2000) and Frezzotti (2001). These melt inclusions have been observed as both glass and crystalline inclusions, which is primarily a function of cooling rate and composition of the melt (Roedder, 1979). Crystalline melt inclusions in zircon tend to form in slow-cooling environments such as in plutonic rocks, whereas glassy primary inclusions are often found in volcanic rocks, where the melt is rapidly cooled. The study of MI's in accessory minerals such as zircon provide the opportunity to constrain igneous processes that are difficult to understand via conventional methods (Thomas et al., 2003).

Impact-related melt inclusions have been documented in zircons from the Vredefort impact structure, South Africa (Moser et al., 2011). These inclusions were suggested to

be glass, based on their amorphous electron backscatter patterns (EBSP's). The connection of these melt inclusions to impact-induced melting was their preservation along curviplanar and planar fractures which are diagnostically generated by the shockwave. Similar melt inclusions have been recently reported in Apollo zircon grains by Crow (2015), who found both glass and crystalline impact melt inclusions.

1.5.3 Alkali mobility in glasses under an electron beam

When put under the stress of an electron beam, alkali elements (specifically Na and K) in glasses often become mobile. This is a direct result of beam heating and charging effects within the sample (Spray & Rae, 1995). The mobility phenomenon is observed even under low-energy beams (Gedeon et al., 2008), and therefore must be considered in compositional analysis (EPMA, EDS, etc.). The decay line of alkali elements begins as a linear trend during the incubation time, but progresses to an exponential trend as time continues (Gideon et al., 2008). In an effort to diminish the effects of alkali mobility in glasses, various authors have attempted to adjust settings and parameters. For example, Morgan & London (2005) suggest using a wider or defocused beam or lower current densities for the compositional analysis of melt glass inclusions. Reducing the beam current will reduce heating within the irradiated volume (Spray & Rae, 1995). Defocusing or widening the beam itself will also reduce heating and charging effects.

The settings used in this study are listed in Tables C-5 & C-6, and discussed in the Methods section.

1.5.4 Geochronology of zircon

1.5.4.1 Microstructural geochronology

One aspect that will be discussed in this thesis is the geochronology of zircon microstructures. In a sense, shock microstructural geochronology provides a relative timeline of very tightly spaced events, and can help distinguish between the different formational mechanisms. Crosscutting relationships are used to understand the order of formation for shock microstructures, and how they are interrelated. Moser et al. (2011) provided a very comprehensive review of microstructural geochronology in zircons from the Vredefort dome, South Africa, in which he distinguished five different 'phases' of shock microstructure progression in zircon (outlined in section 1.4.1).

1.5.4.2 U-Pb geochronology

The ability of zircon to remain a relatively closed system for millions and even billions of years, combined with the exclusion of Pb from its initial crystal structure, makes it a formidable geochronometer (Bowen, 1988). The decay of U^{238} to Pb^{206} and U^{235} to Pb^{207} provides a double decay chain that is used to pinpoint the age of Pb-loss, attributable to events such as metamorphism or impacts. When combined with geologic and microstructural evidence, U-Pb ages can be used to deduce the timing and type of Pb-loss, a valuable asset to understanding impact events or other geological events.

An example of the link of microstructures and U-Pb ages was provided by Moser et al. (2011). In this study, they suggested the existence of a "hot-shock" and "cold-shock" zone at Vredefort. The "hot-shock" zone consisted of zircons that are shocked and had complete to partial age resetting related to the impact, whereas the cold shock zircons had many shock microstructures (i.e. twins, planar fractures), yet were not age-reset by the

impact. This relationship suggests that temperature may be a major player in the resetting of zircon U-Pb ages, and that shock microstructures, in the absence of necessary temperatures do not always provide a Pb-loss pathway.

1.6 Sample Suites

All samples analyzed in this thesis have been summarized in Appendix C, and described geographically in Appendix B. The majority of the samples collected were of varying granitoid composition, as granitoid rocks constitute the bulk of the exposure of the Vredefort dome. An effort was made to cover as much ground as possible with sample collection, despite relatively poor exposure. This poor rock exposure is the major reason that there remain ‘gaps’ in the sample record across the dome. A visual representation of sample locations is provided in Figure 1-8, below. To help produce this map, a Google Earth map showing the location of all samples collected from this study and any related ZAPLab field excursions was created.

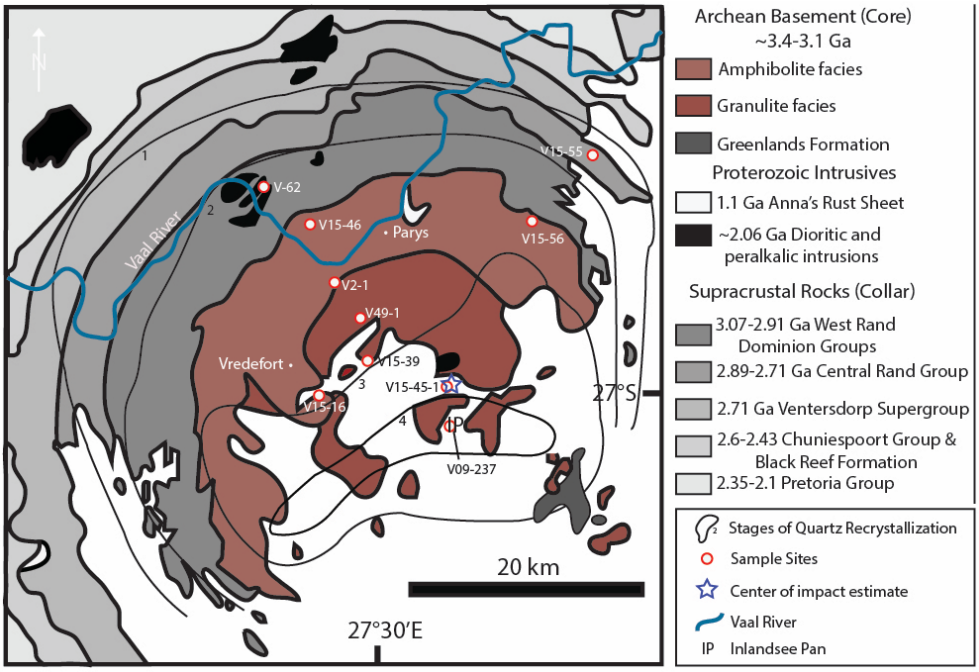

Figure 1-8: Geologic bedrock map of Vredefort impact structure, South Africa, showing the locations of samples used in this study. Map adapted from Moser et al. (2011) and Grieve et al. (1977).

1.7 Overview of thesis

This thesis presents a variety of integrated electron beam techniques that were used to further the understanding of some of the microstructures in zircon from the Vredefort impact structure, South Africa. This thesis can be divided into two distinct sections, or papers:

Chapter 2: Microstructural evolution of *in-situ* zircon across the central uplift of highly shocked Archean crust at the Vredefort impact structure, South Africa.

- The results of an extensive core-to-collar study of zircon microstructures from the Vredefort impact structure will be presented, including some of the trends and disparities in the formation of shock microstructures.

- A quantitative study of shock feature prevalence at multiple sites across the dome is established, and shock microstructures are placed into a chronological order.

Chapter 3: Impact melt glass inclusions in zircon from the central uplift of the Vredefort impact structure, South Africa.

- We have established a best method for the semi-quantitative analysis of melt inclusions in zircon using standard SEM-EDS technology.
- Multiple impact melt inclusion compositions are documented, and compositions are compared to local mineralogy.

Chapter 4 integrates the findings presented in Chapter 1 and 2 and discusses the implications for future research of shock microstructures in zircon. Suggestions are provided for future work in this field, and how to best develop the methods for these analyses.

The purpose of this thesis is to present the analysis and findings represented in both papers to further the understanding of shock microstructures in zircon from the Vredefort dome, South Africa. These findings will be used to further establish Vredefort as an analogue to other large, complex impact structures and even zircons from *ex-situ* solar system samples (i.e. meteorites, breccias). Fitting the microstructures of zircon into a relatively well-constrained regional P/T shock environment will be useful for the study of other impact environments. This study will contribute to the development of zircon as a tool for the reconstruction of planetary history by advancing our knowledge of shock effects on zircon, including the incorporation of impact melt inclusions.

1.8 References

Ahrens, T.J., 1993. Impact erosion of terrestrial planetary atmospheres. *Annual Review of Earth and Planetary Sciences*, *21*, 525-555.

Alvarez, L.W., Alvarez, W., Asaro, F., & Michel, H.V., 1980. Extraterrestrial cause for the Cretaceous-Tertiary extinction. *Science*, *208*(4448), 1095-1108.

Armstrong, R.A., Compston, W., Retief, E.A., Williams, I.T., & Welke, H.J., 1991. Zircon ion microprobe studies bearing on the age and evolution of the Witwatersrand triad. *Precambrian Research*, *53*(3), 243-266.

Armstrong, R.A., Lana, C., Reimold, W.U., & Gibson, R.L., 2006. SHRIMP zircon age constraints on Mesoarchean crustal development in the Vredefort dome, central Kaapvaal craton, South Africa. *Geological Society of America Special Papers*, *405*, 233-253.

Baker, D.M., Head, J.W., Schon, S.C., Ernst, C.M., Prockter, L.M., Murchie, S.L., & Strom, R.G., 2011. The transition from complex crater to peak-ring basin on Mercury: New observations from MESSENGER flyby data and constraints on basin formation models. *Planetary and Space Science*, *59*(15), 1932-1948.

Baldwin, J.A., Phillips, M.M., & Terlevich R., 1981. Classification parameters for the emission-line spectra of extragalactic objects. *Publications of the Astronomical Society of the Pacific*, 5-19.

Bohor, B.F., Betterton, W.J., & Krogh, T.E., 1993. Impact-shocked zircons: discovery of shock-induced textures reflecting increasing degrees of shock metamorphism. *Earth and Planetary Science Letters*, *119*(3), 419-424.

Boon, J.D., & Albritton, C.C., 1936. *Meteorite craters and their possible relationship to "cryptovolcanic structures"*. Texas Southern Methodist University.

Canup, R.M., and Asphaug, E., 2001. Origin of the Moon in a giant impact near the end of the Earth's formation. *Nature, (412),* 708-712.

Carter, N.L., 1965. Basal quartz deformation lamellae; a criterion for recognition of impactites. *American Journal of Science*, *263*(9), 786-806.

Carter, N.L., 1968. Meteoritic impact and deformation of quartz. *Science*, *160*(3827), 526-528.

Cavosie, A.J., Quintero, R.R., Radovan, H.A., & Moser, D.E., 2010. A record of ancient cataclysm in modern sand: Shock microstructures in detrital minerals from the Vaal River, Vredefort Dome, South Africa. *Geological Society of America Bulletin*, *122*(11-12), 1968-1980.

Cavosie, A.J., Erickson, T.M., & Timms, N.E., 2015. Nanoscale records of ancient shock deformation: Reidite (ZrSiO4) in sandstone at the Ordovician Rock Elm impact crater. *Geology*, *43*(4), 315-318.

Chesner, C.A., 1998. Petrogenesis of the Toba Tuffs, Sumatra, Indonesia. *Journal of Petrology*, *39*(3), 397-438.

Chupin, S.V., Chupin, V.P., Barton, J.M., & Barton, E.S., 1998. Archean melt inclusions in zircon from quartzite and granitic orthogneiss from South Africa; magma compositions and probable sources of protoliths. *European Journal of Mineralogy*, *10*(6), 1241-1251.

Collins, G.S., Melosh, H.J., & Ivanov, B.A., 2004. Modeling damage and deformation in impact simulations. *Meteoritics & Planetary Science*, *39*(2), 217-231.

Crow, C., 2015. The early lunar magmatic and impact histories recorded by Apollo zircons (PhD dissertation). University of California-Los Angeles.

Cupelli, C.L., Moser, D.E., Barker, I.R., Darling, J.R., Bowman, J.R., & Dhuime, B., 2014. Discovery of mafic impact melt in the center of the Vredefort dome: Archetype for continental residua of early Earth cratering? *Geology*, *42*(5), 403-406.

Daly, R.A., 1947. The Vredefort ring-structure of south Africa. *The Journal of Geology*, 125-145.

Dietz, R.S., 1961. Vredefort ring structure: meteorite impact scar? *The Journal of Geology*, 499-516.

El Goresy, A., 1965. Mineralbestand und Strukturen der Graphit-und Sulfideinschlüsse in Eisenmeteoriten. *Geochimica et Cosmochimica Acta*, *29*(10), 1131-1151.

Erickson, T.M., Cavosie, A.J., Moser, D.E., Barker, I.R., & Radovan, H.A., 2013. Correlating planar microstructures in shocked zircon from the Vredefort Dome at multiple scales: Crystallographic modeling, external and internal imaging, and EBSD structural analysis. *American Mineralogist*, *98*(1), 53-65.

Fagereng, Å., Harris, C., La Grange, M., & Stevens, G., 2008. Stable isotope study of the Archaean rocks of the Vredefort impact structure, central Kaapvaal Craton, *Contributions to Mineralogy and Petrology*, *155*(1), 63-78.

Fletcher, P., & Reimold, W.U., 1989. Some notes and speculations on the pseudotachylites in the Witwatersrand Basin and Vredefort Dome, South Africa. *South African Journal of Geology*, *92*(3), 223-234.

French, B.M., 1972. Shock-metamorphic features in the Sudbury structure, Ontario: a review. In *New developments in Sudbury geology* (Vol. 10, pp. 19-28).

French, B.M., 1998. Traces of catastrophe: A handbook of shock-metamorphic effects in terrestrial meteorite impact structures.

Frezzotti, M.L., 2001. Silicate-melt inclusions in magmatic rocks: applications to petrology. *Lithos*, *55*(1), 273-299.

Gedeon, O., Zemek, J., & Jurek, K., 2008. Changes in alkali-silicate glasses induced with electron irradiation. *Journal of Non-Crystalline Solids*, *354*(12), 1169-1171.

Gibson, R.L., & Reimold, W.U., 2008. *Geology of the Vredefort impact structure: A guide to sites of interest* (Vol. 97). Council for Geoscience.

Gibson, R.L., Reimold, W.U., & Stevens, G., 1998. Thermal-metamorphic signature of an impact event in the Vredefort dome, South Africa. *Geology*, *26*(9), 787-790.

Glass, B.P., Wasson, J.T., & Futrell, D.S., 1990. A layered moldavite containing baddeleyite. In *Lunar and Planetary Science Conference Proceedings* (Vol. 20, pp. 415-420).

Grieve, R.A.F., & Robertson, P.B., 1976. Variations in shock deformation at the Slate Islands impact structure, Lake Superior, Canada. *Contributions to Mineralogy and Petrology*, *58*(1), 37-49.

Grieve, R.A.F., Dence, M.R., and Robertson, P.B., 1977, Impact and Explosion Cratering, in Impact and Explosion Cratering: Pergamon Press (New York), p. 791– 814.

Grieve, R.A.F., Coderre, J. M., Robertson, P. B., & Alexopoulos, J., 1990. Microscopic planar deformation features in quartz of the Vredefort structure: Anomalous but still suggestive of an impact origin. *Tectonophysics*, *171*(1), 185-200.

Grieve, R.A.F., Robertson, P.B., & Dence, M.R., 1981. Constraints on the formation of ring impact structures, based on terrestrial data. In *Multi-ring basins: Formation and evolution (pp.* 37-57).

Grieve, R.A.F., 1987. Terrestrial impact structures. *Annual Review of Earth and Planetary Sciences*, *15*, 245-270.

Grieve, R.A.F., 1991. Terrestrial impact: The record in the rocks. *Meteoritics*, *26*(3), 175-194.

Hall, A.L., & Molengraaff, G.A.F., 1925. Vredefort mountain land in the southern Transvaal and the northern Orange Free State. Koninklijke Akademie van wetenschappen.

Hargraves, R.B., 1961. Shatter cones in the rocks of the Vredefort Ring. *Transactions of the Geological Society of South Africa*, *64*, 147-161.

Hart, R.J., 1978. A study of the isotopic and geochemical gradients in the old granite of the Vredefort structure, with implications for continental heat flow.

Hart, R.J., Andreoli, M.A., Tredoux, M., & De Wit, M.J., 1990. Geochemistry across an exposed section of Archaean crust at Vredefort, South Africa: with implications for mid-crustal discontinuities. *Chemical Geology*, *82*, 21-50.

Hart, R.J., McDonald, I., Tredoux, M., De Wit, M.J., Carlson, R.W., Andreoli, M., & Ashwal, L.D., 2004. New PGE and Re/Os-isotope data from lower crustal sections of the Vredefort Dome and a reinterpretation of its "crust on edge" profile. *South African Journal of Geology*, *107*(1-2), 173-184.

Head, J.W., 1977. Origin of outer rings in lunar multi-ringed basins-Evidence from morphology and ring spacing. In *Impact and Explosion Cratering: Planetary and Terrestrial Implications* (Vol. 1, pp. 563-573).

Henkel, H., & Reimold, W.U., 1998. Integrated geophysical modelling of a giant, complex impact structure: anatomy of the Vredefort Structure, South Africa. *Tectonophysics*, *287*(1), 1-20.

Hildebrand, A.R., Penfield, G.T., Kring, D.A., Pilkington, M., Camargo, A., Jacobsen, S.B., & Boynton, W.V., 1991. Chicxulub crater: a possible Cretaceous/Tertiary boundary impact crater on the Yucatan Peninsula, Mexico. *Geology*, *19*(9), 867-871.

Hinton, R.W., & Upton, B.G.J., 1991. The chemistry of zircon: variations within and between large crystals from syenite and alkali basalt xenoliths. *Geochimica et Cosmochimica Acta*, *55*(11), 3287-3302.

Hoskin, P.W.O., & Black, L.P., 2000. Metamorphic zircon formation by solid-state recrystallization of protolith igneous zircon. *Journal of metamorphic Geology*, *18*(4), 423-439.

Huber, M.S., Črne, A. E., McDonald, I., Hecht, L., Melezhik, V.A., & Koeberl, C., 2014. Impact spherules from Karelia, Russia: Possible ejecta from the 2.02 Ga Vredefort impact event. *Geology*, *42*(5), 375-378.

Jarosewich, E., 2002. Smithsonian microbeam standards. *Journal of Research of the National Institute of Standards and Technology*, *107*(6), 681-685.

Kamo, S.L., Reimold, W.U., Krogh, T.E., & Colliston, W.P., 1996. A 2.023 Ga age for the Vredefort impact event and a first report of shock metamorphosed zircons in pseudotachylitic breccias and granophyre. *Earth and Planetary Science Letters*, *144*(3), 369-387.

Kieffer, S.W., & Simonds, C.H., 1980. The role of volatiles and lithology in the impact cratering process. *Reviews of Geophysics*, *18*(1), 143-181.

Killick, A.M., & Reimold, W.U., 1990. Review of the pseudotachylites in and around the Vredefort Dome, South Africa. *South African Journal of Geology*, *93*(2), 350-365.

Kleinmann, B., 1968. The breakdown of zircon observed in the Libyan Desert Glass as evidence of its impact origin. *Earth and Planetary Science Letters*, *5*, 497-501.

Koeberl, C., Poag, C.W., Reimold, W.U., & Brandt, D., 1996. Impact origin of the Chesapeake Bay structure and the source of the North American tektites. *Science*, *271*(5253), 1263.

Kovaleva, E., Klötzli, U., Habler, G., & Wheeler, J., 2015. Planar microstructures in zircon from paleo-seismic zones. *American Mineralogist*, *100*(8-9), 1834-1847.

Krogh, T.E., Davis, D.W., & Corfu, F., 1984. Precise U-Pb zircon and baddeleyite ages for the Sudbury area. In *The geology and ore deposits of the Sudbury structure*, *1*, *431-446*. Ontario Geological Survey.

Lana, C., Gibson, R.L., & Reimold, W.U., 2003. Impact tectonics in the core of the Vredefort dome, South Africa: Implications for central uplift formation in very large impact structures. *Meteoritics & Planetary Science, 38*(7), 1093-1107.

Lana, C., Reimold, W.U., Gibson, R.L., Koeberl, C., & Siegesmund, S., 2004. Nature of the Archean midcrust in the core of the Vredefort dome, Central Kaapvaal Craton, South Africa. *Geochimica et Cosmochimica Acta, 68*(3), 623-642.

Langenhorst, F., 2002. Shock metamorphism of some minerals: Basic introduction and microstructural observations. *Bulletin of the Czech Geological Survey, 77*(4), 265-282.

Li, Z., 1994. The silicate melt inclusions in igneous rocks. *Fluid Inclusions in Minerals, Methods and Applications*, 73-94.

Lilly, P.A., 1981. Shock metamorphism in the Vredefort collar: evidence for internal shock sources. *Journal of Geophysical Research: Solid Earth, 86*(B11), 10689-10700.

Lilly, P.A., 1980. Faulting mechanics in the collar rock of the Vredefort ring structure. *Tectonophysics, 67*(1), 45-60.

Martini, J.E., 1978. Coesite and stishovite in the Vredefort dome, South Africa. *Nature, 272*, 715-717.

Martini, J.E., 1991. The nature, distribution and genesis of the coesite and stishovite associated with the pseudotachylite of the Vredefort Dome, South Africa. *Earth and Planetary Science Letters, 103*(1-4), 285-300.

McCarthy, T.S., 2006. The Witwatersrand Supergroup. *The Geology of South Africa*, 155-186.

Melosh, H.J., & McKinnon, W.B., 1978. The mechanics of ringed basin formation. *Geophysical Research Letters, 5*(11), 985-988.

Melosh, H.J., 1982. A schematic model of crater modification by gravity. *Journal of Geophysical Research: Solid Earth, 87*(B1), 371-380.

Melosh, H.J., 1989. Impact cratering: A geologic process. *Oxford Monographs on Geology and Geophysics, 11*, 1.

Morgan, G.B., & London, D., 2005. Effect of current density on the electron microprobe analysis of alkali aluminosilicate glasses. *American Mineralogist, 90,* 1131-1138.

Morgan, J.V., Warner, M. R., Collins, G. S., Melosh, H. J., & Christeson, G. L., 2000. Peak-ring formation in large impact craters: Geophysical constraints from Chicxulub. *Earth and Planetary Science Letters*, *183*(3), 347-354.

Moser, D.E., 1997. Dating the shock wave and thermal imprint of the giant Vredefort impact, South Africa. *Geology*, *25*(1), 7-10.

Moser, D.E., 2001. Birth of the Kaapvaal tectosphere 3.08 billion years ago. *Science. 291*(465), 465-468.

Moser, D.E., Cupelli, C.L., Barker, I.R., Flowers, R.M., Bowman, J.R., Wooden, J., & Hart, J.R., 2011. New zircon shock phenomena and their use for dating and reconstruction of large impact structures revealed by electron nanobeam (EBSD, CL, EDS) and isotopic U-Pb and (U-Th)/He analysis of the Vredefort dome *Canadian Journal of Earth Sciences, 48*(2), 117-139.

NASA. 2004. *The main difference between the simple crater and the complex crater.* Retrieved from http://solarsystem.nasa.gov/galleries/impact-crater-diagram.

Nel, L.T., 1927. *The geology of the country around Vredefort: an explanation of the geological map*. The Government Printing and Stationery Office.

Nicolaysen, L.O., Burger, A.J., & Van Niekerk, C.B., 1963. The origin of the Vredefort dome structure in the light of new isotopic data. *13th General Assembly of the International Union of Geodesy and Geophysics. Berkeley*, *Calif*ornia.

O'Keefe, J.D., & Ahrens, T.J., 1982. The interaction of the Cretaceous/Tertiary extinction bolide with the atmosphere, ocean, and solid Earth. *Geological Society of America Special Papers*, *190*, 103-120.

O'Keefe, J.D., & Ahrens, T.J., 1993. Planetary cratering mechanics. *Journal of Geophysical Research*, *98*(E9), 17011-17028.

Ogilvie, P., Gibson, R.L., Reimold, W.U., Deutsch, A., & Hornemann, U., 2011. Experimental investigation of shock metamorphic effects in a metapelitic granulite: The importance of shock impedance contrast between components. *Meteoritics & Planetary Science, 46*(10), 1565-1586.

Okabe, M., Kanzaki, Y., Shimomura, H., Terasaki, F., Hayashi, T., Kawamura, K., & Kitaura, Y., 2000. Backscattered electron imaging: A new method for the study of

cardiomyocyte architecture using scanning electron microscopy. *Cardiovascular Pathology*, *9*(2), 103-109.

Palme, H., 1980. The meteoritic contamination of terrestrial and lunar impact melts and the problem of indigenous siderophiles in the lunar highland. In *Lunar and Planetary Science Conference Proceedings* (Vol. 11, pp. 481-506).

Rankama, K., & Sahama, T.G., 1950. Geochemistry. 912 pp. *University of Chicago*.

Reed, S.J.B., & Reed, S.J.B., 1975. *Electron microprobe analysis* (Vol. 2). Cambridge: Cambridge University Press.

Reimold, W.U., & Collision, W.P., 1992. Pseudotachylites of the Vredefort Dome and the surrounding Witwatersrand basin, South Africa. *Geological Society of America Special Papers*, *293*, 177-196.

Reimold, W.U., & Gibson, R.L., 2010. *Meteorite impact: the danger from space and South Africa's mega-impact the Vredefort structure* (Vol. 1). Springer Science & Business Media.

Reimold, W.U., & Koeberl, C., 2014. Impact structures in Africa: A review. *Journal of African Earth Sciences*, *93*, 57-175.

Robb, L.J., & Robb, V.M., 1998. Gold in the Witwatersrand basin. *Mineral Resources of South Africa*, 294-349.

Robb, L.J., Charlesworth, E.G., Drennan, G.R., Gibson, R.L., & Tongu, E.L., 1997. Tectono-metamorphic setting and paragenetic sequence of Au-U mineralisation in the Archaean Witwatersrand basin, South Africa. *Australian Journal of Earth Sciences*, *44*(3), 353-371.

Robertson, P.B., 1975. Zones of shock metamorphism at the Charlevoix impact structure, Quebec. *Geological Society of America Bulletin*, *86*(12), 1630-1638.

Roedder, E., 1979. Silicate liquid immiscibility in magmas. *The Evolution of the Igneous Rocks Fiftieth Anniversary Perspectives*, 15-59.

Ryder, G., Koeberl, C., & Mojzsis, S.J. (2000). Heavy bombardment of the Earth at~ 3.85 Ga: The search for petrographic and geochemical evidence. *Origin of the Earth and Moon*, *1*, 475-492.

Schreyer, W., Massonne, H.J., & Chopin, C., 1987. Continental crust subducted to depths near 100 km: implications for magma and fluid genesis in collision zones. *Principles. MPP*, 155-163.

Schwarzman, E.C., Meyer, C.E., & Wilshire, H.G., 1983. Pseudotachylite from the Vredefort Ring, South Africa, and the origins of some lunar breccias. *Geological Society of America Bulletin*, *94*(7), 926-935.

Shand, S. J., 1916. The pseudotachylyte of Parijs (Orange Free State), and its relation to 'trap-shotten gneiss' and 'Flinty crush-rock'. *Quarterly Journal of the Geological Society*, *72*(1-4), 198-221.

Speer, J.G., 1980. Zircon. *Reviews in Mineralogy and Geochemistry*, *5*(1), 67-112.

Spray, J.G., 1995. Pseudotachylyte controversy: Fact or friction? *Geology*, *23*(12), 1119-1122.

Spray, J.G., & Rae, D.A., 1995. Quantitative electron-microprobe analysis of alkali silicate glasses: a review and user guide. *Canadian Mineralogist, 33*(2), 323-332.

Stepto, D., 1990. The geology and gravity field in the central core of the Vredefort structure. *Tectonophysics*, *171*(1), 75-103.

Stevens, G., Gibson, R.L., & Droop, G.T., 1997. Mid-crustal granulite facies metamorphism in the central Kaapvaal Craton: the Bushveld Complex connection. *Precambrian Research*, *82*(1), 113-132.

Therriault, A.M., Grieve, R.A.F., & Reimold, W.U., 1997. Original size of the Vredefort Structure: Implications for the geological evolution of the Witwatersrand Basin. *Meteoritics and Planetary Science*, *32*, 71-77.

Thomas, J.B., Bodnar, R.J., Shimizu, N., & Chesner, C.A., 2003. Melt inclusions in zircon. *Reviews in Mineralogy and Geochemistry*, *53*(1), 63-87.

Tredoux, M., Hart, R.J., Carlson, R.W., & Shirey, S.B., 1999. Ultramafic rocks at the center of the Vredefort structure: Further evidence for the crust on edge model. *Geology*, *27*(10), 923-926.

Vellekoop, J., Sluijs, A., Smit, J., Schouten, S., Weijers, J.W., Damsté, J.S.S., & Brinkhuis, H., 2014. Rapid short-term cooling following the Chicxulub impact at the Cretaceous–Paleogene boundary. *Proceedings of the National Academy of Sciences, 111*(21), 7537-7541.

Walraven, F., Armstrong, R.A., & Kruger, F.J., 1990. A chronostratigraphic framework for the north-central Kaapvaal craton, the Bushveld Complex and the Vredefort structure. *Tectonophysics*, *171*(1), 23-48.

Wegener, A., 1921. Die Entstehung der Mondkrater, Friedrich Vieweg & Sohn, Braunschweig, 48 pp.

Oggmus., 2014. Vredefort crater cross section [A diagrammatic NE-SW cross section through the Vredefort crater showing how the underlying strata were distorted by the meteor impact]. Retrieved July 5, 2016 from: https://en.wikipedia.org/wiki/Vredefort_crater.

Chapter 2

2 Microstructural evolution of *in-situ* zircon across the central uplift of highly shocked Archean crust at the Vredefort impact structure, South Africa

Connor L. Davis and Desmond E. Moser

2.1 Introduction

Impact cratering is known to have played a principal role in the crustal and biological evolution of the Early Earth (Frey, 1980; Pace, 1997). The absolute age and pace of putative events such as the Late Heavy Bombardment (LHB) (Turner et al., 1973) will remain largely unknown until methods for reading physical impact records and understanding shock metamorphism are further developed. Current end-member modeling of impact flux results in divergent evolution of the Early Earth's crust; from highly heterogeneous effects leaving areas of primary lithosphere intact (Grieve et al., 1990) to wholescale re-melting of the outer 10 km of the Earth by impact melting and impact-triggered mantle melting (Marchi et al., 2014). Large-scale, surficial records of terrestrial impacts from events such as the LHB have largely been removed due to the destructive forces of billions of years of tectonism and erosion on Earth. In fact, only 188 terrestrial impact craters have been confirmed (Spray & Hines, 2009), identified primarily based on large-scale morphological or structural evidence. Fortunately, evidence of impact cratering is also seen on the microscopic level, as the passage of a shockwave creates a variety of unambiguous shock microstructures in minerals such as zircon which are able to persist over extensive geological time and in some cases can be used to directly date shock metamorphism. Often, these minerals are the only remaining vestiges of long destroyed impact craters, and can provide key evidence for the location

and shock conditions of an otherwise enigmatic impact event on planetary crusts. Exploring the range and nature of zircon shock microstructures across a variety of shock conditions promises better reconstruction of the shock history of the Earth as well as other rocky planets and planetesimals. This work represents the first *in-situ* analysis of shocked zircon across a major complex impact structure. The study presents details on the sequence of microstructure development at different radial distances in the crater floor and the relative frequency of occurrence of these features within a rock and across the central uplift.

2.1.1 Shock metamorphic studies of quartz and other rock-forming minerals

Historically, microscopic-scale studies of shock metamorphism have focused on quartz. Quartz is a useful shock indicator mineral because it is common in crustal target rocks, and preserves a large array of shock effects, including planar deformation features (PDF's), planar fractures (PF's), and mechanical twinning (Stöffler and Langenhorst, 1994). High-pressure quartz polymorphs coesite and stishovite have also been attributed to the shock process (Stöffler, 1971). However, quartz microstructures are rather susceptible to post-shock alteration by processes such as recrystallization, as noted in Grieve et al.'s (1990) analysis of recrystallized quartz at the Vredefort impact structure, South Africa. The orientation and distribution of planar deformation features (PDF's) in quartz (Grieve et al., 1990) were analyzed in the hopes that they could be used to infer shock pressures experienced in the central uplift. The results of this study were anomalous, as intense post-shock recrystallization in the core of the central uplift resulted in annealing of many of these PDF's. The general zones of quartz recrystallization are displayed overlain on a bedrock geology and sample map in Figure 2-1.

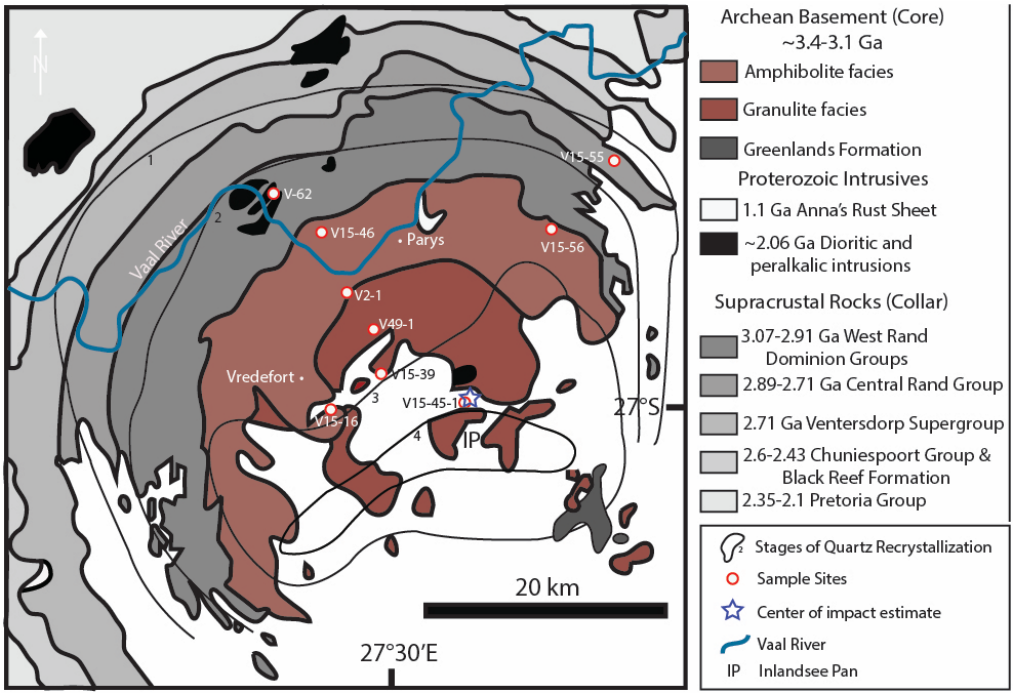

Figure 2-1: Bedrock geology map of Vredefort central uplift, South Africa, showing locations of samples, and centre of impact. Map adapted from Moser et al. (2011), geology modified from Nel (1921) and stages of quartz recrystallization (1-4) from Grieve et al. (1990).

Feldspars have also been used to characterize the shock process, but suffer from many of the same adversaries as quartz. Moreover, neither of these common minerals are suitable for high temperature geochronology methods such as U-Pb dating, the benchmark method for the geological timescale. In essence, a more robust and stable indicator of shock is necessary to progress the absolute timing of impact cratering history, especially in large craters which are predisposed to high post-shock temperatures that can cause widespread recrystallization.

2.1.2 Zircon shock microstructures

Zircon ($ZrSiO_4$) has recently become an important tool in impact crater research, largely due to its robustness and resilience against the adverse effects of erosion, tectonism, and metamorphism, as well as its capacity as a powerful U-Pb and Lu-Hf geochronometer. Shock microstructures that have been documented in zircon can be considered as two main groups. The dominant group are those created in very short time scales experience by ejecta materials and fallback deposits such as breccias and suevites (e.g. Bohor et al., 1993; Krogh et al., 1993). The other less-explored group of microstructures are those generated in target rocks that remain in the crater basement (i.e. the volume of crust beneath impactites and impact melt). Zircons in these environments have been shown to host a spectrum of microstructural and isotopic responses to a single cratering event. This spectrum is a consequence of large radial pressure gradients and extreme thermal gradients accompanied by equally extreme times of exposure to post-impact heating and strain in crater floor environments. For example, an ejecta zircon and crater zircon may experience instantaneous loading and unloading cycles as high as 100 GPa, whereas the thermal exposure of the two grains will range from seconds in an ejecta plume to hundreds to thousands of years in the central uplift of the crust beneath a crystallizing melt sheet.

Crater basement zircons have previously been shown to record a wide range of shock microstructures. Planar fractures have been identified in orientations: (010), (100), {112}, (011) (Moser et al., 2011; Erickson et al., 2013). Some {112} planar features host microtwins oriented 65° about <110>, and are thought to form when an increased shear stress is exerted on regular {112} PF's (Moser et al., 2011). Microtwins are thought to form at shock pressures between 20-40 GPa (Moser et al., 2011), although this remains

an estimate, and further study to properly constrain these conditions is necessary. Curviplanar features, occasionally referred to as curviplanar fractures (Moser et al., 2011) or non-planar fractures (Cavosie et al., 2010) have been identified at Vredefort, and are attributed to the rarefaction shockwave. These features are commonly annealed and are sub-parallel to {112} PF's (Erickson et al., 2013). Impact melt glass inclusions have also been documented along annealed curviplanar and planar features by Moser et al. (2011). Occasionally, these open fractures can lead to grain margin displacement (Krogh et al., 1984). Reidite, a high pressure $ZrSiO_4$ polymorph (Glass et al., 2002), has yet to be discovered at Vredefort, despite the fact that much of the central uplift believed to have reached shock pressures above the 40 GPa transition. Assuming it was originally present, it has likely reverted back to zircon due to high post-impact temperatures, and would possibly have been present along microtwin lamellae. Two types of granular-textured zircon have been reported, including decomposition of single grains to very fine-grained zircon formed in ejecta environments (Bohor et al., 1993), and coarser granular zircon formed from the immense post-shock temperatures in a complex impact structure (Kamo et al., 1996; Moser, 1997; Cavosie et al., 2015). Both of these textures have been documented at Vredefort. The distinction between these two textures is further discussed in this study. At even greater temperatures, zircon can decompose into its oxides, baddeleyite (ZrO_2) and silica (SiO_2), beginning at ~60 GPa and 1700°C (Wittmann et al., 2006). This has yet to be documented at Vredefort.

As shown, the zircon microstructures associated with shock metamorphism are diverse and, as we report, still growing. There has also been some ambiguity in the nomenclature of shock microstructures in zircon. For the purposes of this study, we define planar

features as any of the following: planar ‘fractures’ that are either annealed or filled by melt; planar fractures that remain open and unfilled; microtwins oriented 65° about [110]; ‘microcleavage,’ or low-angle (<10°) planar boundaries; and planar deformation bands (PDB’s) (Cavosie et al., 2015). PDB’s have been identified in terrestrial and lunar impact environments (Cavosie et al., 2015; Nemchin et al., 2009) and terrestrial tectonic environments (Kovaleva et al., 2015), and appear as bands of misoriented zircon (less than 2.7°) oriented parallel to {110}. Curviplanar features are defined as non-planar filled fractures that are impact-related, and typically delineated by impact melt glass inclusions, as in Moser et al. (2011). These fractures have been largely annealed due to remnant heat related to the impact melt glass inclusions, hence the abandonment of the term ‘fracture’ for the purposes of this study.

The compatibility of zircon for U uptake (in place of Zr^{+4}) and its exclusion of Pb makes it an incredible age indicator, providing precise U-Pb ages that can be linked to igneous, metamorphic, and impact events. Krogh (1984) provided a direct link between shock microstructures and U-Pb discordance in zircon, the understanding of which was enhanced by later terrestrial and lunar impact studies by Bohor et al. (1993), Pidgeon et al. (2011) and Moser et al. (2011).

2.1.3 Purpose of this study

Undeformed by tectonic processes, and eroded to expose the deep roots of the complex structure, the Vredefort central uplift, South Africa, is among the best terrestrial analogue sites for the study of zircons from similar rock types in an array of shock metamorphic environments in the crater basement. Despite the recent focus on zircon at Vredefort, no study has yet provided an *in-situ* analysis of zircons across the full extent of the central

uplift. The microscale record in zircon has the potential to be used to deduce the timing and magnitude of large impacts in terrestrial and *ex-situ* solar system samples, provided we have a more complete understanding of mineral and isotopic response and variability to complex impacts. The purpose of this study was to enhance the understanding of the variability of shock processes on zircon by analyzing zircons from a suite of granitoid-composition rocks (+1 quartzite) from various known shock environments across the Vredefort impact structure, South Africa. An attempt is made to provide a quantitative scale of the effects of shock on zircon based primarily on the location of these zircons within the regional context of a large complex impact crater.

2.2 Geological Setting

The Vredefort impact structure (S27°0', E27°30') is located approximately 120 km southwest of Johannesburg, South Africa, and is expressed surficially as a semi-annular array of topographically high supracrustal rocks constituting the outer limit of the Vredefort dome. The dome itself is approximately 70 km in diameter, including an ~45 km inner core of primarily Archean gneisses and an ~25 km outer core of Archean to Proterozoic rocks (Gibson & Reimold, 2008). Persisting after ~2.02 Ga of erosion (~8-10 km; Gibson et al., 1998), the dome represents the remnant central uplift of the once larger Vredefort impact structure, which would have been between 250-300 km in diameter (Therriault et al., 1997). The inner annulus of the central uplift at Vredefort hosts poorly exposed mid to lower crustal rocks (amphibolite to granulite, respectively) exhumed during the impact event (Stepto, 1979; Hart et al., 1981; Lana et al., 2004). This cross-section through the Kaapvaal Craton was emplaced at the surface by fluid-like rebound within the crater, leading to the higher-grade granulites surrounded by amphibolite-facies

rocks. Further evidence for this “crust-on-edge” model was provided by Hart et al. (1991) and Tredoux et al. (1999) who discovered harzburgite and other upper mantle ultramafic rocks at the centre of the central uplift.

2.3 Methods & Sample Locations

2.3.1 Methods

Roughly 30 samples (~1 kg each) were collected during field work in February, 2015. A subset was chosen for more intensive analysis, and were prepared as thin or thick sections, polished for ~3 hours with 0.06 um colloidal silica (neutral NaOH solution) on a Buehler VibroMet 2 vibratory polisher and carbon coated to ~25 um with an Edwards Auto 306 carbon coater.

The bulk of the analytical results for this study were collected with the Hitachi SU6600 field emission gun scanning electron microscope (FEG-SEM) from Western University's Zircon and Accessory Phase Laboratory (ZAPLab). Samples were characterized using a combination of feature mapping and phase mapping to locate the various ‘features’ (i.e. zircon, monazite) and main phases (i.e. quartz) in each sample. Upon location of the important features and phases, backscatter electron imaging (BSE) and secondary electron imaging (SE) were performed on ~15 of the largest (by length) grains for basic sample characterization (conditions listed in Table 2-1). Approximately 40-50 grains from six of the samples were analyzed with BSE/SE in order to obtain a survey of shock microstructures. Cathodoluminescence (CL) images were taken of select grains using a Gatan ChromaCL detector attached to the FEG-SEM (Table 2-1). Further microstructural data was captured with an Oxford Instruments Nordlys electron backscatter diffraction (EBSD) detector (Table 2-1). Energy dispersive spectroscopy (EDS) was performed with

an Oxford Instruments X-max silicon state detector (SSD) incorporated into the FEG-SEM (Table 2-1).

	Shock Survey (BSE/SE)	CL	EBSD	EDS Mapping
SEM System	Hitachi SU6600	Hitachi SU6600 Gatan ChromaCL	Hitachi SU6600 Oxford Instruments Channel 5	Hitachi SU6600 Oxford Instruments INCA
Carbon coat	Yes	Yes	Yes	Yes
Acc. voltage	15 kV	10 kV	20 kV	10 kV
Probe current	Variable	3.5-4.3 nA	~12 nA	Variable
Tilt	--	--	70°	--
Working distance	10.0 mm	12.5 mm	19.0 mm	10.0 mm
Apertures	3/1 (50µm/200µm)	2/3 (100µm/50µm)	3/2 (50µm/100µm)	2/1(100µm/200µm)
Gain	Medium-High	Medium	High	Medium

Table 2-1: Analysis conditions for the shock survey and backscatter electron & secondary electron (BSE/SE) imaging, cathodoluminescence (CL), electron backscatter diffraction (EBSD), and energy dispersive spectroscopy (EDS). Advanced EBSD parameters are found in Appendix A.

2.3.2 Sample Locations

Samples were collected from locations at different radial distances within the Vredefort central uplift to provide a complete transect from core to collar. The specific locations, and how they fit into the regional geology, are shown in Figure 2-1. Sample coordinates and rock types are listed in Table 2-2. Primarily granitoid composition samples were collected as they are the most common and volumetrically significant rock type in the crustal section. This reduced the bias attributed to the variance of shock effects in different rock types. To extend the radius of the survey deeper into the supracrustal rocks

of the collar, one quartzite sample from the Witwatersrand Supergroup was collected as well.

Sample Name	Lithology	Sample Type	Radial distance	Coordinates (UTM)	
V15-55	Quartzite	Thick Section	~24.5 km	563809 m E	7030330 m S
V-62	Alkali Feldspar Granite	Thick Section	~22.8 km	534627 m E	7029025 m S
V15-56	Outer Granite Gneiss	Thin Section	~19 km	560295 m E	7025905 m S
V15-46	Outer Granite Gneiss	Thin Section	~17.1 km	539943 m E	7025719 m S
V2-1	Charnockitic Gneiss	Thick Section	~11.4 km	540804 m E	7019340 m S
V49-1	Charnockitic Gneiss	Thick Section	~8.9 km	542531m E	7015741 m S
V15-16	Inlandsee Leucogranofels	Thin Section	~8.6 km	540091 m E	7010527 m S
V15-39	Inlandsee Leucogranofels	Thin Section	~5 km	543699 m E	7014140 m S
V15-45-1	Inlandsee Leucogranofels	Thin Section	<1km	550161 m E	7011662 m S

Table 2-2: Sample list indicating lithology type, sample type, distance from the currently accepted centre of impact (~4km N of Inlandsee Pan), and coordinates in UTM.

2.4 Results

2.4.1 Shock microstructures across the core-collar transect

This section describes the shock microstructures observed in each sample to portray some of the disparities in the formation and preservation of shock microstructures along the core-to-collar transect.

2.4.1.1 V15-55 Quartzite (~24.5 km from centre of impact)

Sample V15-55 is a quartzite unit in the Central Rand Group (2.89-2.71 Ga) of the Witwatersrand Supergroup. It is known to host SiO_2 polymorphs coesite and stishovite (Martini, 1978), constraining the shock metamorphic conditions to at least 2-3 GPa, 700°C and >10 GPa, >1200°C, respectively. Quartz grain boundaries exhibit triple

junctions, and the grains contain impact-induced planar deformation features. Detrital zircon grains in the sample analyzed are rare, and igneous, oscillatory zonation patterns are present in the majority of these grains. The zoning is cross-cut by random short and curved fractures that are typical products of differential expansion of zircon during metamictization, as well as sets of shock-induced conjugate planar fractures (Figure 2-2). In some cases, there is minor displacement along these fractures as shown by offset grain margins. No other shock-induced features were observed. To our knowledge, this is the first report of *in-situ* shocked zircon at this radial distance from the centre.

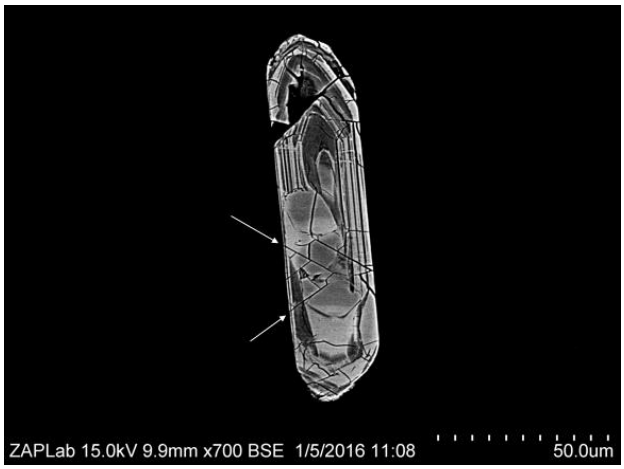

Figure 2-2: Shocked zircon F397 from V15-55, showing two orientations of planar fractures (white arrows) and some more typical irregular cracking due to differential expansion due to metamictization.

2.4.1.2 V-62 Alkali Feldspar Syenogranite (~22.8 km from centre of impact)

Sample V-62, a syenogranite from the Baviaanskrantz-Schurwedraii granitic complex (2052 ± 14 Ma) (Graham et al., 2005; Moser et al., 2011) is a coarse grained, massive grey-green rock composed of quartz+albite+k-feldspar+acmite+minor biotite. Zircons are almost exclusively hosted within acmite, which displays many planar microstructures and

melt inclusions, similar to the zircons that they host. Zircons range from 5 μm's to over 500 μm's in size. Zircons are mostly irregularly shaped and anhedral to subhedral. Zircons from V-62 preserve a variety of different shock microstructures, including planar and curviplanar features, multiple orientations of microtwins (Fig. 2-3), impact melt glass inclusions, and grain-margin displacement. The quality of preservation of these features in this sample is notable. Microtwins {112} rotated 65° about <110> in F3313 significantly disrupt zonation patterns, which is seen in both the CL and BSE images (Fig. 2-3a and b, respectively). A conjugate set of microtwins is observed. There is almost no recrystallization in the zircons, except in a few grains where a plagioclase-composition melt pocket has induced a zone of recrystallization. This melting is likely attributed to the impact process, as vestiges of this melt can be found pervasively tracing infilled planar fractures and curviplanar features within the zircons as well.

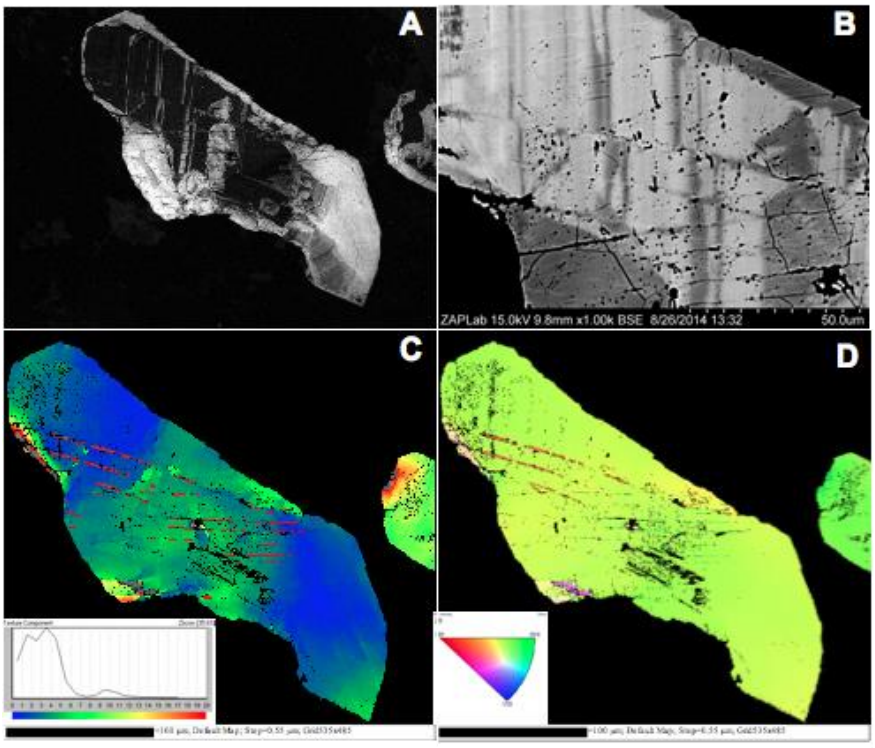

Figure 2-3: V-62 F3313 a) CL image showing zonation and shock microstructures, b) inset BSE image showing planar features, twins, and IMG inclusions (dark), c) EBSD misorientation map with microtwins outlined in red.

2.4.1.3 V15-56 Outer Granite Gneiss (OGG) (~19 km from centre of impact)

V15-56 is a coarse-grained gneissic rock, composed of plagioclase+quartz+orthoclase+ muscovite+hornblende. This sample is found within the amphibolite-grade Outer Granite Gneiss (OGG) zone (~3.1 Ga; Hart et al., 1981; Hart et al., 1990), in a quarry cross-cut by 30 cm-scale pseudotachylite dykes a few hundred metres below the base of the Witwatersrand quartzite contact. Quartz grains in this sample display abundant PDF's and undulose extinction. Zircons are preferentially found within or near plagioclase and biotite grains, with an average size of ~25 μm's, with the largest being ~116 μm's. The majority of the zircon grains are euhedral. Zircons have relatively few higher-pressure deformation microstructures (i.e. lack of microtwins). Zircons are not recrystallized, and largely retain their original magmatic zonation patterns. Planar features (annealed or filled planar fractures) and curviplanar features are present, but not as plentiful as in many of the other samples. These features are often delineated by traces of tiny, ovoid melt inclusions that often continue into larger "pods" of melt within the interiors of the grains (Fig. 2-4). Displacement is present in some of the grains (Fig. 2-4). No evidence of the high-pressure polymorph reidite or breakdown to baddeleyite and silica was detected in this sample.

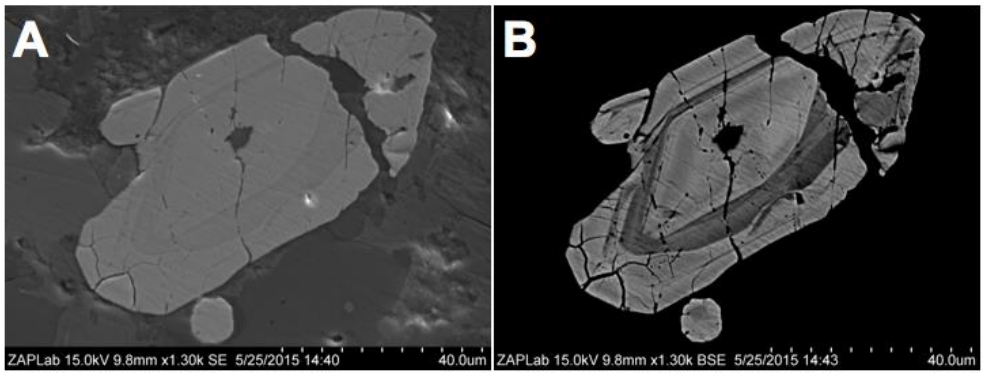

Figure 2-4: V15-56 F3037 A) SE image, B) BSE image showing curviplanar features and annealed planar fractures delineated by impact melt glass inclusions (with pod of melt in the middle of the grain), and a displaced curviplanar feature. Note the absence of microtwins. This grain is not typical of the main population.

2.4.1.4 V15-46 Outer Granite Gneiss (OGG) (~17.1 km from centre of impact)

Sample V15-46 is from a quarry area near a popular field stop to illustrate m-scale pseudotachyllite dykes. It is a medium-coarse grained granitic gneiss composed of plagioclase+quartz+myrmekite+orthoclase+minor biotite+minor muscovite+/-hornblende. This rock is also found within the Outer Granite Gneiss (OGG) zone. The outcrop from which this sample was collected hosts extensive pseudotachylite. Quartz grains display multiple orientations of annealed PDF's. Zircons are found preferentially within the feldspars (or along grain boundaries), and occasionally within quartz. Average zircon length is ~76 μm's, with a maximum size of 175 μm's. Morphologies are variable, but the majority of the grains are euhedral and long-prismatic. Zircons rarely show evidence of recrystallization, and primary magmatic zonation patterns are often well preserved. Zircons seem to host an abundance of melt inclusions (Fig. 2-5, 2-6), but very little evidence of shock microstructures (i.e. microtwins, planar features, etc.). Annealed or filled planar fractures and planar and curviplanar features are present in the majority of

the grains (albeit not as extensively as in other samples), traced by tiny ovoid melt inclusions that often lead to a larger pod of melt within the zircon (Fig. 2-5). Of the grains imaged with EBSD, no grains displayed evidence of microtwins, a notable observation given the abundant macroscopic shock features in the outcrops in which this sample was situated.

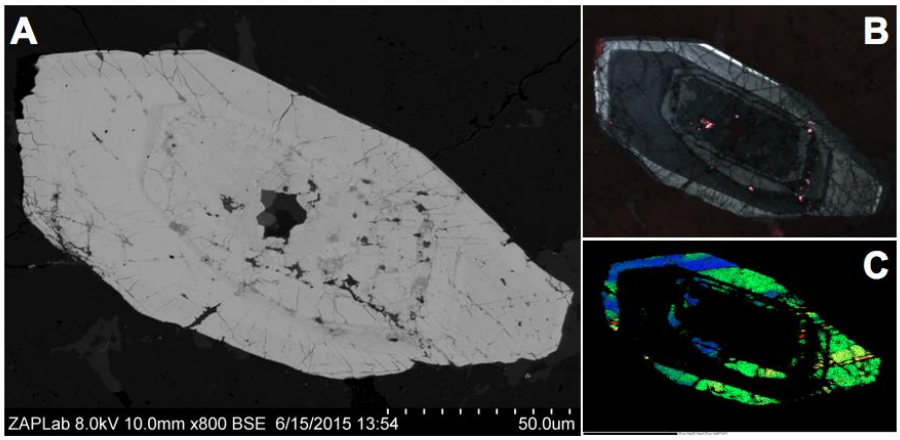

Figure 2-5: a) BSE image of V15-46 F725 showing multiple compositions of IMG inclusions, b) CL image showing relatively undisturbed zonation, c) EBSD misorientation map showing amorphous (metamict) zones and planar features.

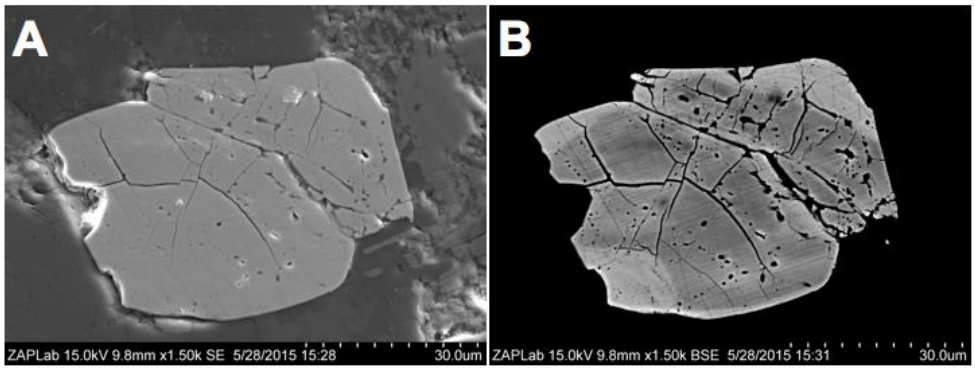

Figure 2-6: V15-46 F24565 a) SE image and b) BSE image showing pervasive melt along planar and curviplanar features.

2.4.1.5 V2-1 Charnockitic Gneiss (~11.4 km from centre of impact)

The absence of microtwins in V2-1 is a coarse-grained green-greyish rock located at the gradational transition from amphibolite to granulite-facies rocks. This area is rich in m-scale pseudotachylite veins, and is known as the Vredefort Discontinuity. V2-1 is classified as a charnockitic gneiss and the mineralogy of this rock is quartz + plagioclase + hypersthene +/- orthoclase. The rock has been previously dated by Moser et al. (2001), who dated zircons at ~3.094±0.007 Ga. Zircons in V2-1 are primarily concentrated near or within hypersthene, and seldom found within quartz and feldspars. The average grain length is ~70 μm's, with the largest being ~170 μm's. The majority of the zircons are euhedral. Zircon shock microstructures in this sample are quite variable. Some grains appear relatively unshocked, while others are intensely shocked. F3655, for example, displays three cross-cutting orientations of microtwins, oriented 65° about [110], a considerable degree of crystal plastic deformation, curviplanar and planar features, and numerous impact melt glass inclusions (Fig. 2-7). Crosscutting twinned domains noticeably displace each other as well (Fig. 2-7c). An example of newly described planar deformation 'twist' bands (PDB-twist) is present in F3655 (Fig. 2-7c) emanating from the large amorphous inclusion in the lower left of the zircon. This feature is an ~4-5 μm's in length and tapers out into a pointed end. This is the only feature of its kind in this zircon, and appears 'twisted' in misorientation EBSD maps (Fig. 2-7c). 'PDB-kinks,' similar to PDB's identified by Cavosie et al. (2015 and Kovaleva et al. (2015) are identifiable in the centre of the grain along planar features as μm-scale parallel domains of misoriented zircon (white arrow, Fig. 2-7c). Twins terminate along amorphous zones (impact melt glass inclusions) and appear to be crosscut by one set of planar features as well. Low angle boundaries detected in EBSD are often related to shock microstructures

(microtwins and planar/curviplanar features often delineate the boundaries). Pervasive impact melt glass inclusions are found in trails along curviplanar and planar features, spatially related to microtwins, and exhibiting a bright CL response (Fig. 2-7b).

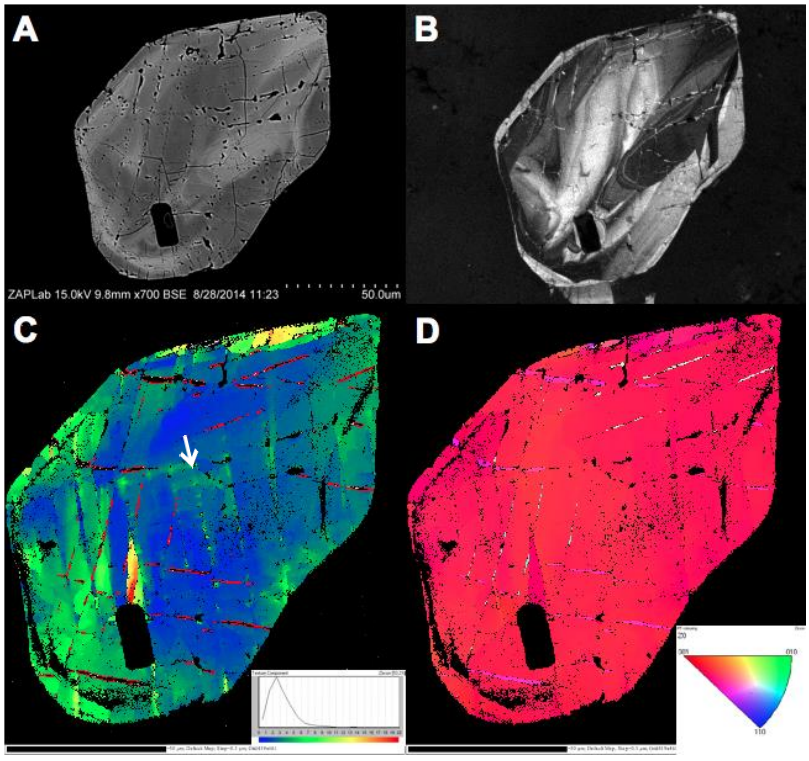

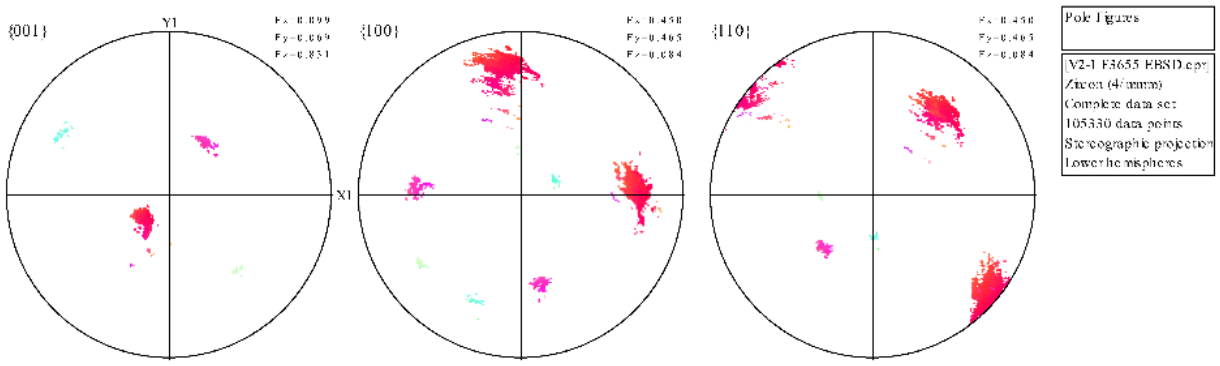

Figure 2-7: V2-1 F3655 a) BSE image displaying impact melt inclusions tracing twins and curviplanar features, b) CL image showing undisturbed zonation, c) EBSD misorientation map with microtwins outlined in red, white arrow indicates PDB kinks, d) inset EBSD IPF map with associated pole figures below.

2.4.1.6 V49-1 Tonalitic (Charnockitic) Gneiss (~8.9 km from centre of impact)

V49-1 (~3.1 Ga, Moser et al. (2001)) is a medium grained tonalitic (charnockitic) gneiss crosscut by a tonalite dyke of the same age. Similar to V2-1, this sample is from the gradational contact between middle and lower-crustal rocks. The mineralogy of this rock is plagioclase + quartz + minor orthoclase + minor hypersthene. Zircons are primarily concentrated within or near hypersthene grains, with average lengths at ~70 μm's. Zircons are typically euhedral to subhedral and regularly shaped, elongate. Planar features and curviplanar features are present in the majority of grains, and very small, ovoid impact melt glass inclusions are typically present along these planar and curviplanar features. Displacement is variably present, and many zircons show late-stage shearing along a displacement zone, in which the margins are often recrystallized into relatively fine granules (Fig. 2-8). Curviplanar features can sometimes be traced across this sheared displacement zone (Fig. 2-8c). Any recrystallization in this sample is usually associated with these displacement zones.

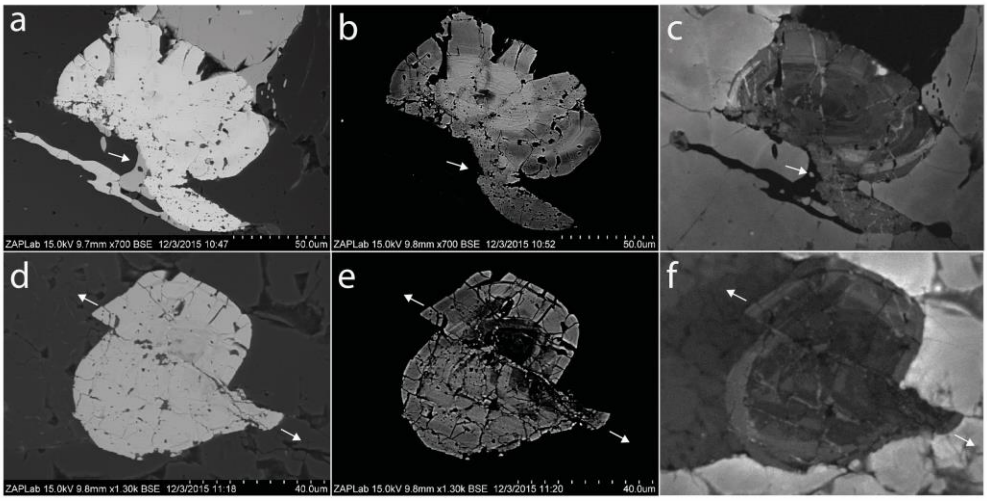

Figure 2-8: V49-1 F3481 a) SE image, b) BSE image, c) CL image, and F3890 d) SE image, e) BSE image, and f) CL image. White arrows indicate displacement zones.

2.4.1.7 V15-16 Granodioritic Gneiss (~8.6 km from centre of impact)

Sample V15-16 is a fine-to-medium-grained, milky grey-white granodioritic gneiss (plagioclase + quartz + biotite + orthoclase +/- clinopyroxene). This rock is located near the granulite-amphibolite facies transition. Quartz grains do not display any obvious shock features, however biotite is often kink-banded. Zircons are primarily found associated or directly within biotite, with some within orthoclase and plagioclase. Zircons average ~45 μm's, ranging up to 160 μm's, with most grains less than 65 μm's in length. There is a noted diversity in zircon morphology, from short and stubby, to elongate. The majority of the grains in this sample contain planar features, curviplanar features, impact melt glass inclusions +/- microtwins and displacement. There is a bright CL response along many planar/curviplanar features and along some of the displacement-associated recrystallization zones. A number of grains in this sample display what we have defined as planar deformation 'twist' bands emanating from the exteriors of the grains and

exhibiting twisted interior misorientation (Fig. 2-9, 2-10). The planar deformation twist bands do not exceed 15-25 μm's in length, and are typically only a few μm's in

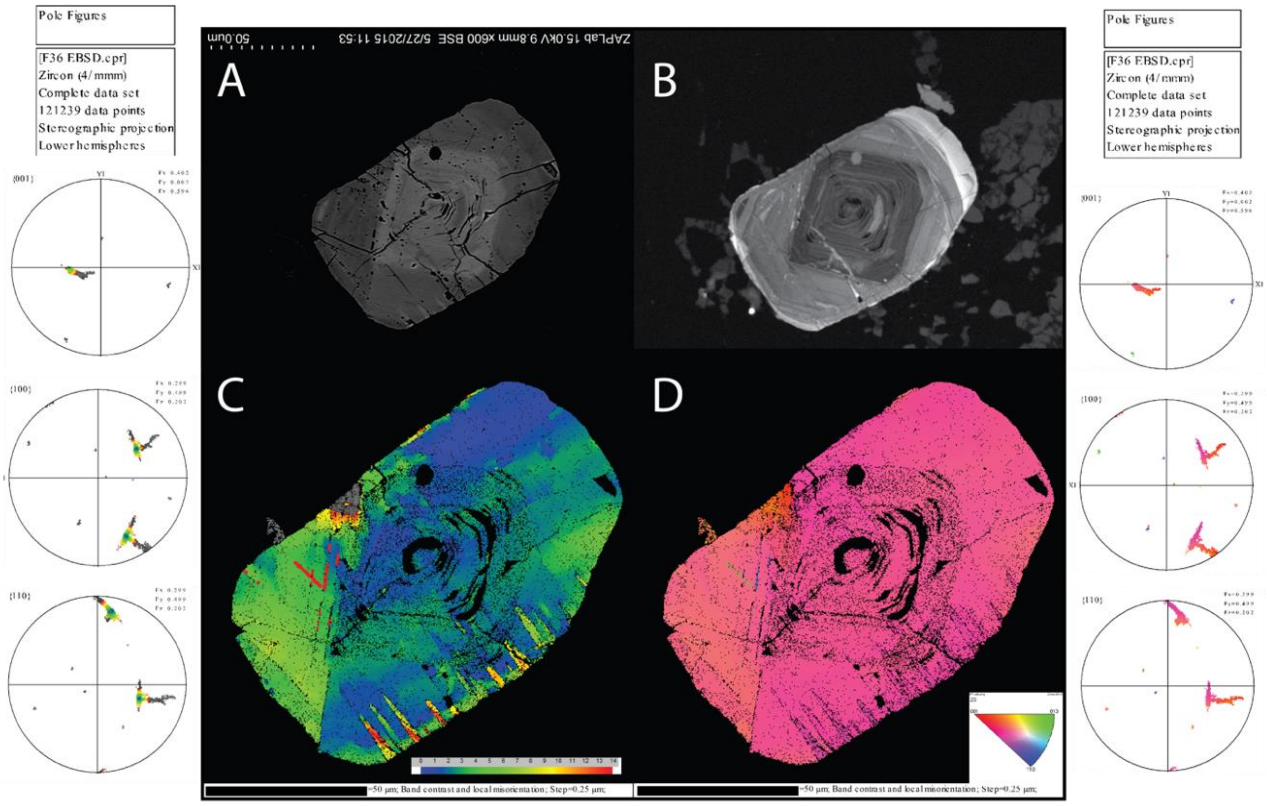

maximum width, tapering along strike. These features have not, to our knowledge, been reported in any other shock studies of zircon. Zircons in this sample tend not to be recrystallized, largely preserving their primary magmatic zonation patterns. Minor recrystallization is sometimes prevalent, but only along grain margin displacement zones within the zircon.

Figure 2-9: V15-16 F36 a) BSE image where planar deformation band 'twists' are slightly detectable, b) CL image showing relatively undisturbed zonation, c) EBSD misorientation map showing up to ~14° misorientation with associated pole figures (left), and d) IPF map with associated pole figures (right). Figure displays interesting shock-induced 'planar deformation twist bands' emanating from exteriors of grains, as well as a conjugate set of microtwins (Fig. c, outlined in red).

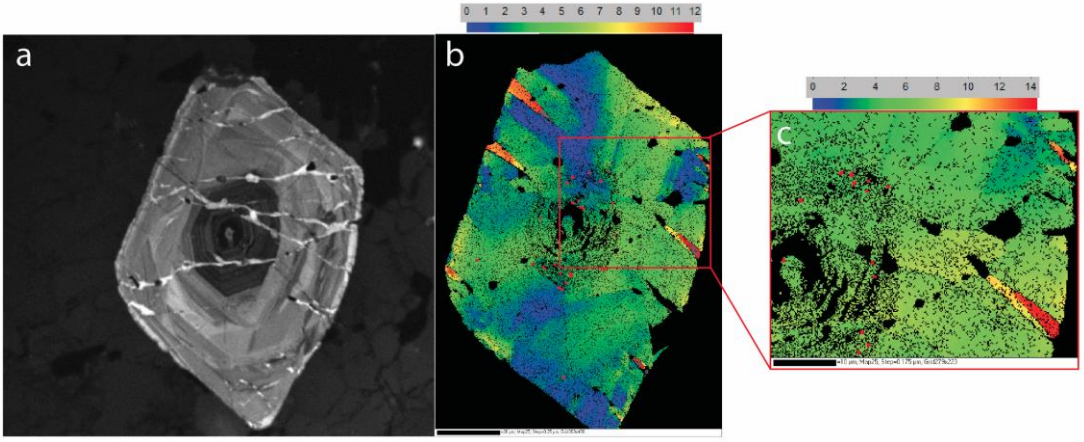

Figure 2-10: V15-16 F279 a) CL image showing bright areas around curviplanar feature-hosted impact melt glass inclusions, b) EBSD misorientation map showing up to 12° of misorientation mostly accommodated in zircon 'planar deformation twist bands' emanating from exterior of grain. These twist bands are inferred across the zircon grain. c) EBSD misorientation map of zoom-in from b), showing twist-band morphology.

An almost complete shock microstructural sequence, including planar features and curviplanar features, microtwins, impact melt glass inclusions, displacement, post-shock recrystallization and crystal plastic deformation is displayed in V15-16 zircon F617 (Fig. 2-11), whereas the surrounding minerals show no record of any of this. Shock microtwins in {211}, oriented 65° to [110] are prevalent in the lower left zone of the grain, and appear to bend slightly to the right as they approach the recrystallized domain, where they then disappear. Planar features and curviplanar features are mostly prevalent in the upper right of the grain, where they too disappear upon contact with the recrystallized zone. Recrystallization occurs along a dextral (right-lateral) displacement contact within the zircon that can be traced outwards to the boundaries between orthoclase and plagioclase (Fig. 2-11b). The occurrence of displacement and recrystallization in this

zircon can be visibly related to the surrounding mineralogy and associated shock impedance contrasts. The preservation potential of zircon is highlighted in Fig. 2-11f, when compared to surrounding anorthite and orthoclase that are completely recrystallized.

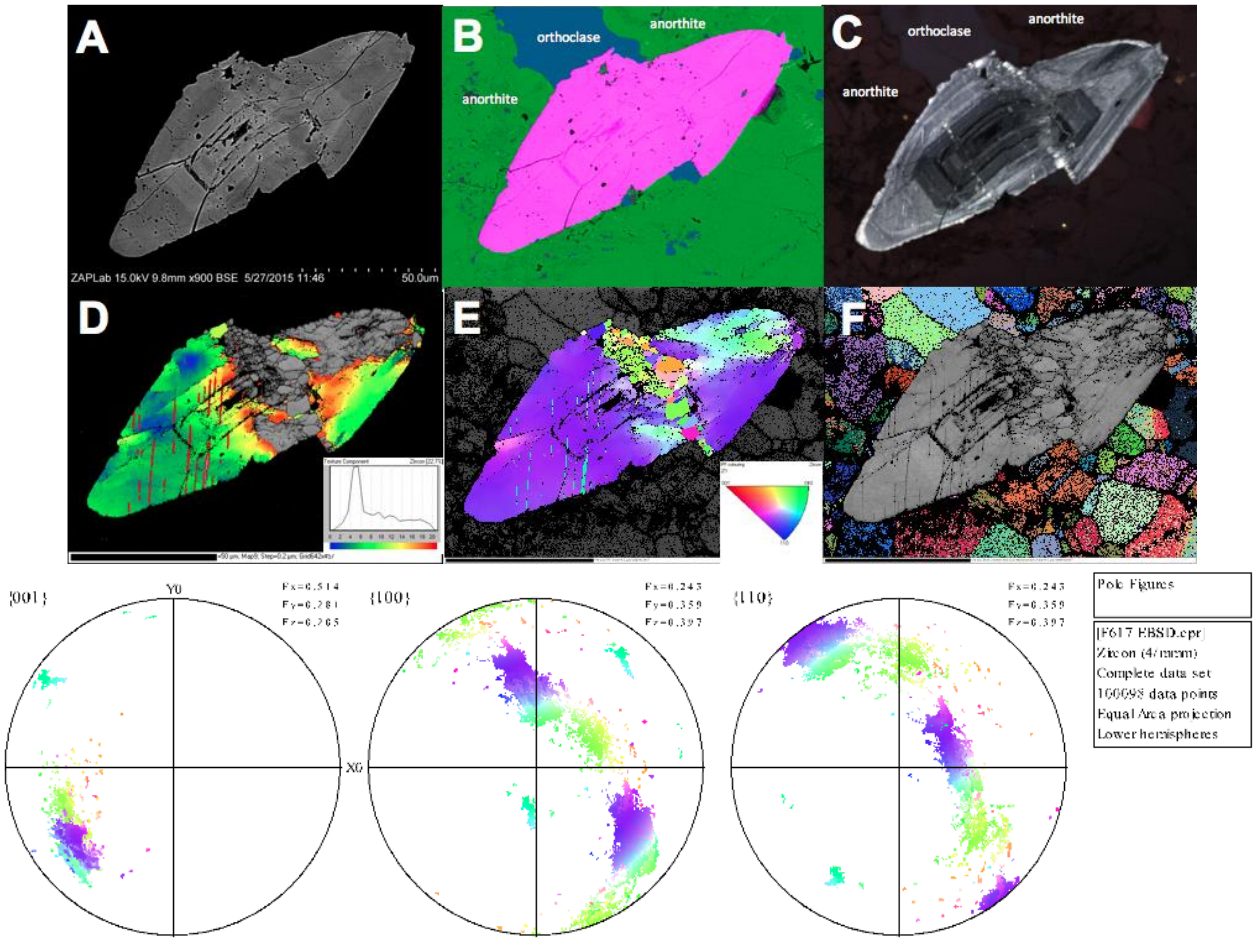

Figure 2-11: V15-16 F617 a) BSE image showing IMG inclusions, b) EDS map image (pink=Zircon, blue=orthoclase, green=anorthite) showing intersection of different phases at approximate location of displaced zircon boundary, c) CL image indicating brighter CL response along displaced, recrystallized boundary, d) EBSD misorientation map showing microtwins (red line) and up to 20° misorientation, e) EBSD inverse pole figure map showing microtwins (light blue lines), a heavily recrystallized displacement zone, and a zone of planar microstructures (upper right), including associated pole figures, below, f) euler angle map of anorthite and

orthoclase, outlining triple junctions that are comparable to triple junctions in recrystallized displacement zone in zircon.

2.4.1.8 V15-39 Inlandsee Leucogranofels (ILG) (~5 km from centre of impact)

V15-39 (ILG, ~2.8 Ga; Hart et al., 1981, Hart et al., 1990) is a fine-medium grained pink-white syenogranitic gneiss (quartz + plagioclase + orthoclase), bearing many textural similarities to V15-45-1. These textural similarities include domains of glomerogranular quartz that retain the original gneissic foliation that is obvious in hand sample (ILG glomerogranular texture). In thin section, minerals have triple junctions, confirming the metamorphic nature of this rock. Optically, quartz grains do not display obvious shock features, as is expected from Grieve et al.'s (1990) analysis of rocks from the UHT core. The zircons in this sample are small, averaging ~17 μm's in size, with a maximum of 89 μm's. Zircons preferentially appear along grain boundaries, specifically between quartz and the feldspars. Zircon grains in V15-39 are often recrystallized, displaying nodular and granular zircon growth, however most grains retain at least some of their original magmatic zonation. An example of this is F5348, shown in Fig. 2-12a-c, where half of the grain exhibits fairly consistent primary zonation, where the other half (top right) is in the process of recrystallization. Very few grains display any other shock features, however some grains display minor planar features (Fig. 2-12d), curviplanar features and displacement. Another notable observation in this sample is the presence of baddeleyite grains rimmed by zircon (Fig. 2-12g). The presence of baddeleyite with a zircon rim (surrounded by quartz) suggests this sample experienced peak conditions >1700°C (El Goresy, 1965).

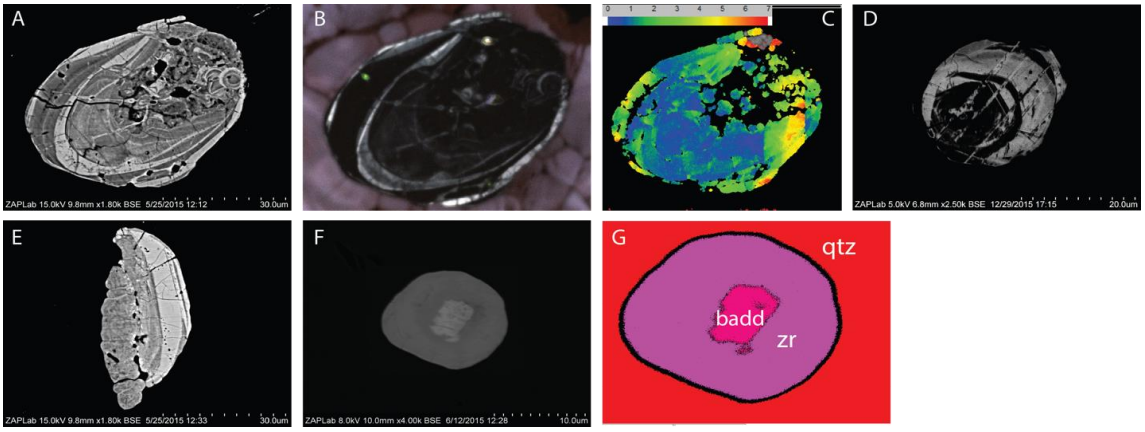

Figure 2-12: V15-39 F6348 a) BSE image, b) CL image, c) EBSD misorientation image, d) F5913 BSE image, e) F5627 BSE image showing sinistral (left-lateral) displacement. The left half of the grain appears to be missing, f) baddeleyite BSE image, g) EDS map of baddeleyite BSE image, g) EDS map of baddeleyite with zircon and quartz surrounding.

2.4.1.9 V15-45-1 Inlandsee Leucogranofels (ILG) (<1 km from centre of impact)

V15-45-1 is an ~2x1m boulder of fine-medium grained ILG from a farm field at the approximate geographic centre of impact (taken as ~4 km N of the Inlandsee Pan). To our knowledge, this sample may be the closest to the centre of impact ever examined. The rock is composed of quartz + orthoclase + plagioclase + minor muscovite. Quartz has been recrystallized into micrometer sized granules that retain the original primary fabric of the rock (classic ILG glomerogranular texture (Fig. 2-13b). Quartz grains do not preserve shock features (i.e. PDF's). Zircons are preferentially found within the glomerogranules of quartz (Schreyer, 1983; Stepto, 1990), providing insight into how zircon reacts to extreme recrystallization in comparison to quartz (Fig. 2-13c). Average zircon length is ~30 μm's, however lengths range up to ~260 μm's in some zircons undergoing recrystallization that remained intact and grew in clusters. Morphologies vary greatly, from small, stubby zircons, to longer, more acicular zircons. All grains display at

least minor recrystallization, with some grains fully recrystallized into coarsely granular zircon, as in F445 (Figure 2-14c). Maximum granule size is ~40-50 μm's in F445, with many other grains displaying smaller granules. In large granules, individual and newly formed concentric zonation is present, visible in BSE and CL (Fig. 2-15b, d). Many grains have a bright BSE response (Fig. 2-14), where the granule interiors appear brighter than their rims. None of the grains analyzed in this sample show any obvious evidence for planar or curviplanar features, microtwins, crystal plastic deformation, or impact melt glass inclusions. EBSD response is typically null for zircons from this sample, and a CL halo is seen around the majority of the zircons due to radiation damage from metamictization (Fig. 2-15d). Similar to V15-39, there is an obvious difference in the degree of recrystallization from grain to grain, however V15-45-1 represents the only sample in the central uplift where there are no distinct shock features preserved.

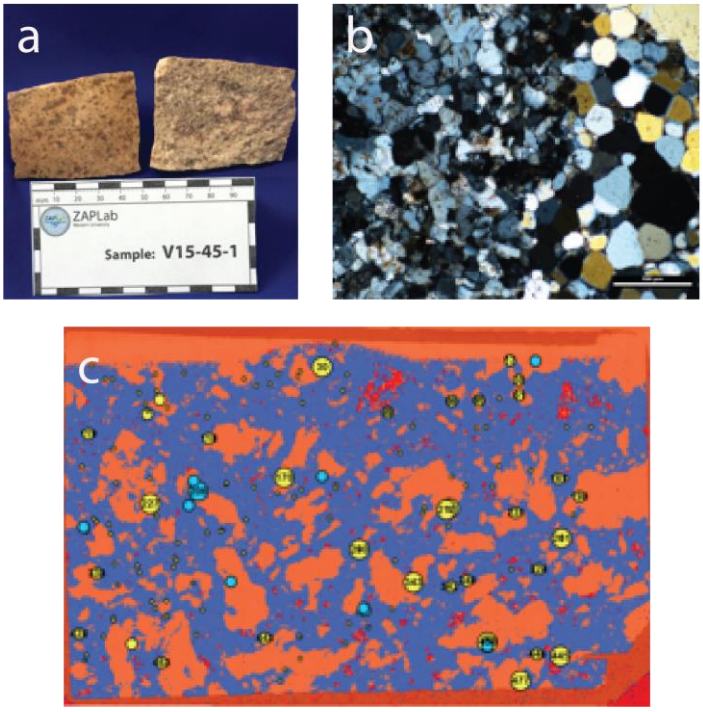

Figure 2-13: a) V15-45-1 hand sample, b) Recrystallized quartz grains, typical of ILG rocks at Vredefort, c) V15-45-1 ArcGIS map showing preferential location of zircons (yellow circles), and baddeleyite (blue circles) within quartz glomerogranules (orange). Blue is orthoclase and red is plagioclase.

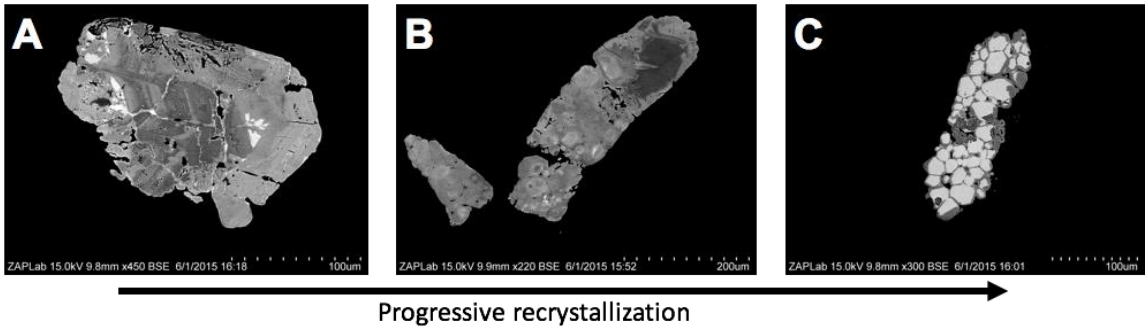

Figure 2-14: BSE images of three V15-45-1 zircon grains showing the variance in levels of recrystallization, from a) minor recrystallization, primary zonation remaining largely intact, b) displacement and the beginning of relatively undeveloped granularization, and c) complete granularization into a coarsely polycrystalline zircon.

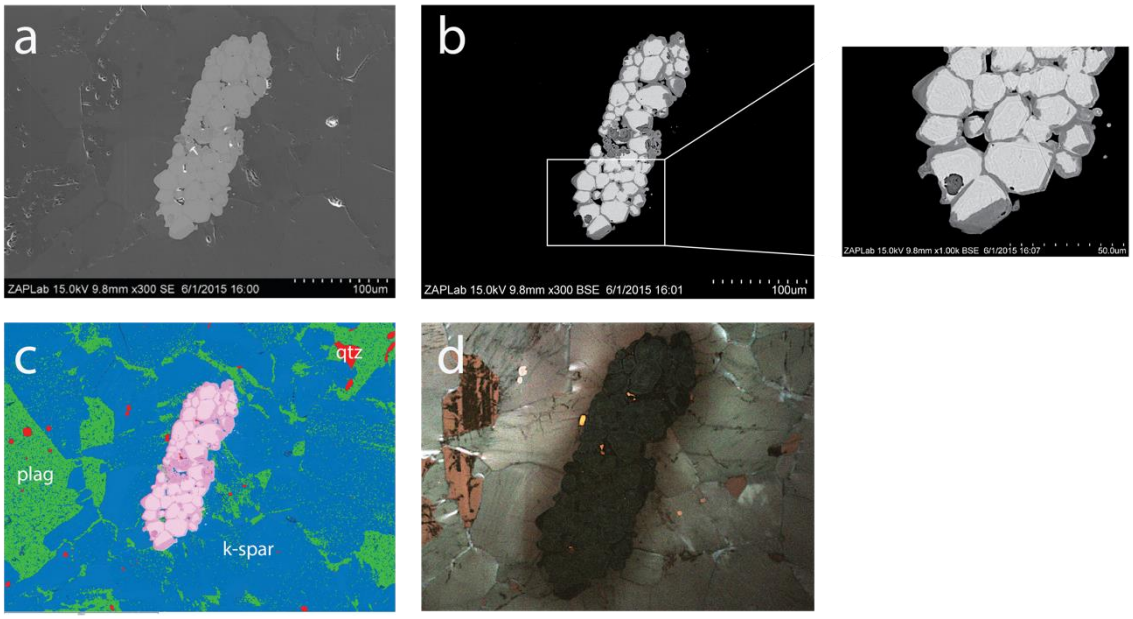

Figure 2-15: V15-45-1 F445 a) SE image, b) BSE image with inset zoom image showing compositional dichotomy between core and rims of zircon granules, c) EDS map showing plagioclase (green), orthoclase (blue), quartz (red), and zircon (pink), d) CL image that displays the newly formed zonation patterns in individual granules.

2.4.2 Proportions of pre-impact and shock-related features in zircon populations

A subset of six samples was chosen to represent the shock metamorphic gradient at roughly equal intervals of radial distance. An in-depth accounting of microstructures of ~40-50 *in-situ* zircons was performed on a petrographic polished thin or thick section of each sample. The transect ended at station V15-39, the in-place bedrock sample nearest to the centre of impact. This survey catalogued the presence of the following features: primary, pre-impact zonation (oscillatory or sector); planar features (including planar fractures, microtwins, 'microcleavage,' and planar deformation bands), curviplanar features; impact melt glass inclusions; granular/polycrystalline zircon; and grain margin displacement by through-going fracture networks. Grains were primarily imaged with

BSE/SE to determine the presence of the above listed features. A subset of grains from each sample were analyzed with other methods such as EBSD and CL to confirm the presence of microtwins or impact melt glass inclusions.

For the purpose of this survey, ‘shock features’ are defined as any impact-related deformation or crystallographic change in the zircon that alters its pre-impact state. This includes a variety of features created by the spectrum of processes in the crater environment, including: shock loading and unloading, impact-triggered melting, annealing, and recrystallization, and post-shockwave deformation of the crater floor during the modification stage. We acknowledge the possibility that not all shocked zircons will exhibit definitive shock features in the plane exposed through a given sample, and hence our values may be considered as minimum estimates. Nevertheless, the effort is justified in view of the novelty of the attempt.

The primary, Archean magmatic and metamorphic chemical zonation patterns are the dominant feature present in the majority of the samples. These zonation patterns were only lost in cases of intense post-shock recrystallization in one sample. Across the majority of the transect, nearly 100% of the zircons retained primary zoning with minor recrystallization. This was most significantly reduced to ~75% in the high temperature granular textures found in V15-39, where the majority of grains exhibited partial recrystallization, but still retained some of their primary zonation (Fig. 2-16). The proportion of grains exhibiting shock, as herein defined, is also fairly consistent across most samples (Fig. 2-16), although the occurrence frequency of different shock features is variable. The percentage of shocked zircons ranges from 80% to 100%, with the exception of collar quartzite V15-55, which could be due to a number of factors,

including: 1) decreased shock conditions due to radial distance from the core, and/or 2) rock type (quartzite) being less susceptible to shock than the other granitoid samples.

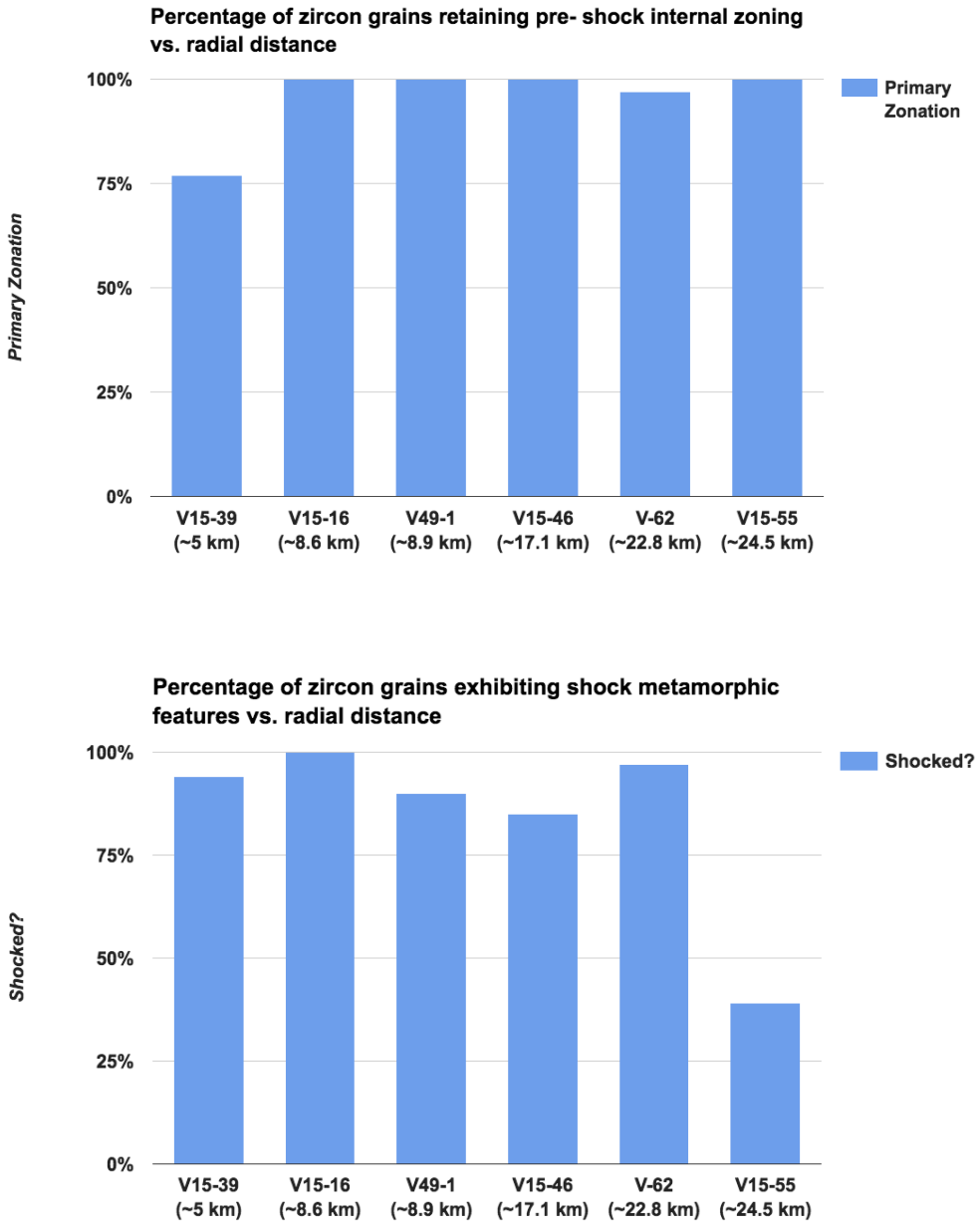

Figure 2-16: Bar graphs showing the percentage of zircons retaining at least partial domains of primary zonation patterns and those that are 'shocked' from samples across the Vredefort central uplift.

2.4.3 Types of shock-related features in zircon populations

A bar graph displaying the prevalence of different types of shock features in zircons from the six subset samples is shown in Figure 2-17. The findings are summarized below by feature type.

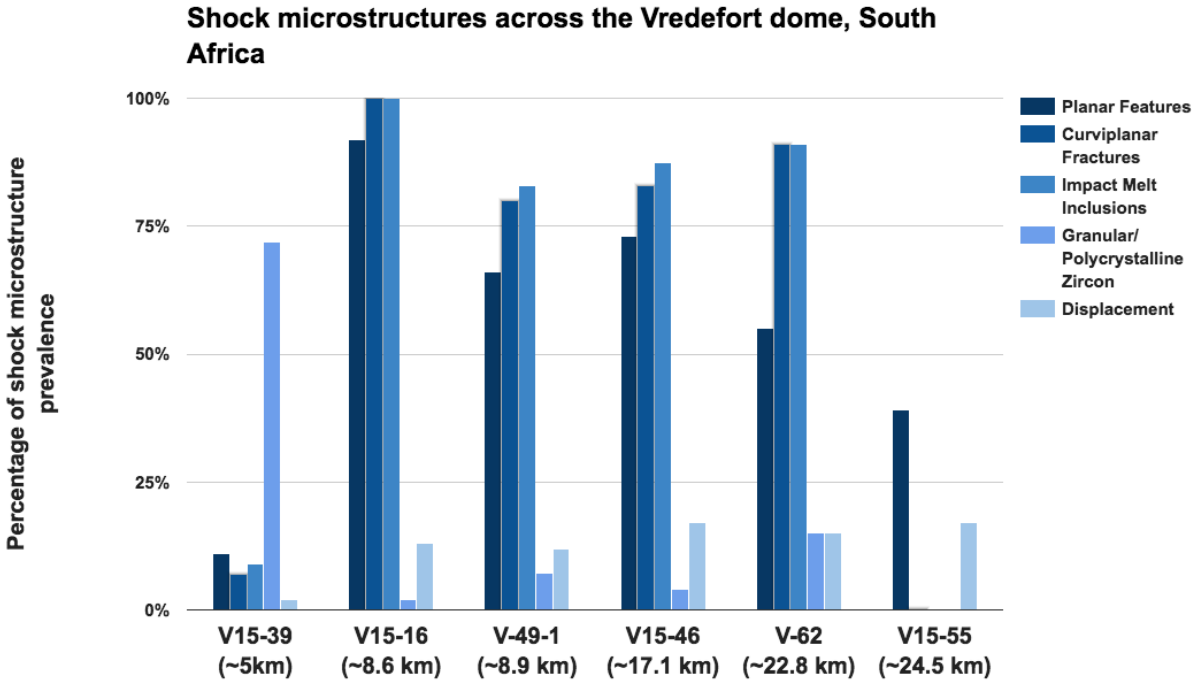

Figure 2-17: Bar graph displaying the percentage of each microstructure from the largest 40-50 grains of each sample. The line represents the trend of decreasing planar feature prevalence with increasing distance from the centre. The dotted line represents a rough estimate of planar feature prevalence in V15-39 if it did not undergo post-shock recrystallization.

Planar features (open or melt-filled fractures, 'micro-cleavage', microtwins, planar deformation bands)

With regard to planar features, prevalence can be roughly correlated with radial distance from the centre of impact (Fig. 2-17). Open (unfilled) planar fractures are only observed in the quartzite sample V15-55 (~24.5 km radial distance) (Fig. 2). All other planar features from sites closer to the centre of impact are either impact-melt filled fractures which have been annealed or are 'micro-cleavage' surfaces (Leroux et al., 1999). "Micro-cleavage" features and annealed planar fractures are present in some respect in almost all samples the exception of V15-55. With the exception of the largely recrystallized V15-39, there is a roughly linear increase in the prevalence of planar features, from 55% to 90%, as the centre of impact is approached. The trend (Fig. 2-17) indicates that the number of expected planar features in V15-39 would be nearly 100% if not for the effects of post-impact recrystallization. A precise radial distance at which some form of planar feature in zircon would completely disappear is difficult to predict.

The scope of this study precluded the time for EBSD analysis that would allow full quantification of microtwin abundance in the full zircon population. Nevertheless, microtwins were documented in V49-1, V15-16, and V-62, and are notably absent from intervening sites V15-39, V15-46 and V15-55. V15-39 is largely recrystallized, and thus is unlikely to preserve microtwins.

Curviplanar features (annealed low-angle boundary networks, grain displacement) and impact melt glass inclusions

Curviplanar features were found in all samples other than V15-55. Curviplanar features are quite common in V15-16, V49-1, V15-46, and V-62 (Fig. 2-17). The visual evidence and statistical relationship between curviplanar features and impact melt glass inclusions indicates a close connection, both temporally and spatially, between the two respective formation mechanisms (Fig. 2-17). Impact melt glass (IMG) inclusions are found along both planar and curviplanar features. The majority of samples analyzed host IMG inclusions, however the morphology of these inclusions is variable. IMG inclusions range from elongate melt inclusions (Fig. 2-7) to tiny, ovoid inclusions (Fig. 2-3) and larger, irregularly shaped pods of melt (Fig. 2-5). IMG inclusion prevalence is relatively consistent across all samples (Fig. 2-17), except for V15-39 and V15-55. Detailed information about IMG inclusions is provided in Chapter 3. Strain along some curviplanar features is sufficient to cause visible displacement of the margin of the grain by tens of μm's. This grain margin displacement is typically present in 15-20% of the zircon population in most samples except V15-39. In some cases, grains appear to be displaced along planar fractures as well (e.g. V15-55).

Crystal-plastic deformation

Crystal plastic deformation (CPD) is observed in most zircons from all samples analyzed except those exposed to high post-shock temperatures (V15-45-1, and to some degree, V15-39). These zircons typically hosted a number of low-strain granules. CPD typically forms gradual misorientation changes of several degrees with glide accommodated along [001]. Data was not collected for CPD prevalence across the entire structure, due to time

limitations involved with EBSD, but it should be noted that CPD could be identified in the majority of zircons analyzed.

Granular zircon/recrystallization

The presence of granular/polycrystalline zircon is highest in V15-39 at ~70% of grains, and drops off considerably in the other samples to levels of ~10% (Fig. 2-17). The average diameter of granules in this texture also increases toward the centre of impact. For example, the granule diameter in the collar in sample V-62 is typically sub-micron, whereas average diameter at V15-39 is between 1 to 5 μm's. Granules at the nearest-centre sample (V15-45-1) are much larger, ranging to >10 μm's.

2.5 Discussion

2.5.1 Proportion of pre-impact and shocked zircon features in impacted crust

There has been much speculation as to the survivability of Early Earth zircon in a Late Heavy Bombardment scenario. This speculation is in response to the failure, thus far, to identify shock metamorphic features in 4.0 Ga to 4.4 Ga Hadean Jack Hills zircons (oldest minerals on Earth) (Valley et al. 2014), or to find evidence of high crystallization temperatures typical of zircon crystallized from impact melts (Wielicki et al. 2012). Modeling has suggested ~15% of the early zircon record will be shocked and subsequently age-reset in a heavily bombarded Earth (Abramov & Mojzsis, 2013). Our results show that most zircons (~90%) at Vredefort retain at least partial pre-impact internal zonation, and that a similiar proportion display shock metamorphic features. With estimated erosional levels of approximately 7-10 km (Stevens et al., 1997; Gibson et al., 1998), and shocked zircon in this study found at radial distances of ~24.5 km (V15-55), this translates into an absolute minimum constraint of ~5000 cubic km of shocked

zircon in the crust at Vredefort. It follows, then, that an Early Earth scenario of widespread granitoid crust, and a pervasive bombardment at ~3.9 Ga should have also produced a crust that is rich in shocked zircon. The preservation of ~2.020 Ga shocked zircon in modern detrital systems (Cavosie et al., 2010) suggests that poor preservation is not a likely explanation for the absence of shocked zircon in the Jack Hills suite.

With regard to the types of microstructures, it can be seen that microtwins are found throughout most of the central uplift, and their absence in quartzite sample V-55 suggests that they are broadly diagnostic of the central uplift of the target. There is a noted absence of microtwins in V15-46 (as well as V15-56). This could be related to the pseudotachylite-rich environment from which they are found, where an increase in local melting may lead to a decrease in the relatively 'brittle' deformation. Likewise, the curviplanar features, domains of crystal plastic deformation and the impact melt glass inclusions are present through most of the central uplift but absent in the coherent strata in the collar (V15-55). These features are also characteristic of the central uplift, in particular the post-impact modification stage. The coarse (i.e. μm to >10-μm granule diameter) within 4-5 km of the centre of impact are the only shock related features that do not exhibit crystal plastic deformation, and therefore seem diagnostic of UHT environments in the central uplift proximal to high-temperature mafic impact melts (Moser, 1997; Cupelli et al., 2014). This suite of observations can be used to characterize the central uplift, basement 'facies' of large impact craters, and is of potential use for determining the provenance of detrital and meteoritic samples from our moon and other planets.

2.5.2 Microstructural evolution

The value of zircon as a superior mineral archive of the structural evolution of impact events can be seen in samples such as V15-16 (Fig. 2-11), where surrounding feldspar and quartz grains are in stable and undeformed (completely recrystallized) states. The spatial inter-relationships among the different microstructures in zircon display a general pattern that allows us to place the microstructures in a temporal framework from oldest to youngest, tracing the evolution of impacted crust.

i. Early planar features ('microcleavage,' open and melt-filled planar fractures)

Planar features have previously been suggested to be the earliest formed shock microstructure in the sequence (Moser et al., 2011), which is also demonstrated in our findings. Planar features are often crosscut by curviplanar features, a relationship that is dramatically evident where planar features terminate against displaced curviplanar features (Fig. 2-11). Planar features are themselves often crosscut by other orientations of planar features (Fig. 2-7), indicating multiple generations related to the shock loading process. Figure 2-11 (V15-16) displays c-axis parallel planar features crosscut by twinned domains in a {112} orientation, and twins also crosscut obvious planar features in Fig. 2-7 (V2-1). Planar features are found throughout the Vredefort impact structure (Fig. 2-17), and require the lowest shock conditions of any shock microstructure identified in this study, previously suggested to be ~20 GPa (Wittmann et al., 2006). All samples analyzed in this study, therefore, are assumed to have experienced shock pressures of at least 20 GPa. Open planar fractures in V15-55 and annealed planar fractures in other samples are considered to be coeval and associated with the formation of these early planar features. These open fractures do differ from some of the planar features in other areas of the

central uplift, and may be a lower pressure equivalent of crystallographically-controlled planar features.

ii. *Zircon planar deformation bands (PDB's)*

Zircon planar deformation bands (PDB's) (Cavosie et al., 2015; Kovaleva et al., 2015) have been documented in both impact and tectonic zircons. In this study, we identified two different 'types' of PDB's. We identify conventional PDB's as 'kinks,' which can be compared to previously documented PDB's. The presence of these PDB-kinks in V2-1 (white arrow, Fig. 2-7), a verifiably shocked zircon, indicates that this microstructure may be impact-related. They are typically represented as crystallographically-controlled (planar) tabular regions of low degrees of misorientation. PDB 'twists' are a zircon microstructure found in three different grains in this study, which, to our knowledge, have not been documented before. Two grains from V15-16 (F36 and F274) display these features emanating from the exterior of the zircon (Fig. 2-9, 2-10) while in V2-1 F3655, the feature is observed extending from a primary inclusion which has been variably replaced by impact melt (Fig. 2-7). These features are crystallographically-controlled and are discontinuous across the zircon, often extending just ~15-25 μm's, before tapering out into a pointed end. Maximum thickness of these features is between 1-5 μm's, and average spacing is between 1-5 μm's as well (Fig. 2-9). Within the features themselves, there is a twisted appearance of local misorientation (Fig. 2-9c, 2-10c), which appears to represent a 'twist' in the zircon lattice. This is best seen in Fig. 2-10, where both sides of the zircon have PDB-twists that can be inferred across the crystal. These features are difficult to place into a geochronological timeline, however microtwins, curviplanar features and impact melt glass inclusions are found crosscutting some PDB-twists in

Figure 2-7, providing a latest possible formation time. PDB-twists are always oriented perpendicular relative to the host zircon margin (Fig. 2-9, 2-10). In V2-1 (Fig. 2-7), the PDB extends from an exposed primary inclusion that has been variably replaced by impact melt. This inclusion represents a weakness in the zircon lattice, and in this respect, is treated similiarly to a grain margin from which the typical PDB-twists extend. We suggest that due to the planar appearance and crosscutting relationships, PDB-twists may be related to early planar features, represented as a reactivation of these features as a twist of the zicon lattice. Both kinks and twists are planar elements, however kinks are the microstructural effect of a 'kinking' of the zircon lattice in response to strain, while twists are strain accommodated as a twisting of the zircon lattice, hence the nomenclature.

iii. Microtwins

Microtwins found in this study form along {112} planar features, and are oriented 65° about <110>. Similar to other planar features, there are numerous cross-cutting microtwins (Figs. 2-7, 2-3), indicating multiple generations of twinning in zircon. The formation of these different twin generations is likely relatively coeval. Microtwins crosscut early planar features, but appear to pre-date later planar features, curviplanar features (Fig. 2-7) and recrystallization (Fig. 2-11). Twins are discontinuous across recrystallized zones and sometimes appear slightly curved, or 'dragged,' along displaced and recrystallized margins (Fig. 2-11), displaying the influence of the later curviplanar features and subsequent displacement.

iv. *Late planar features*

Despite crosscutting relationships that show planar features crosscut by microtwins, there also appear to be some planar features that crosscut microtwins (Fig. 2-7). This second

generation of planar features post-dates microtwins, which are generally thought to form during the rarefaction shockwave. These cross-cutting relationships may imply a more complex shockwave progression illustrated in these rocks, indicating that the initial compressional shockwave may still be active during and after the rarefaction that generates microtwinning in zircon.

v. *Curviplanar features*

Curviplanar features are commonly annealed due to heat associated with the impact melt glass inclusions, and are sometimes only visually identifiable by the non-linear trails of melt inclusions that they host. Curviplanar features likely form after the release of initial shock compression (Moser et al., 2011), during shock unloading (rarefaction). They should not be confused with non-planar features (NPF's) (Timms et al., 2012) which are not likely impact-related. Curviplanar features crosscut planar features and microtwins, and themselves are often crosscut by recrystallized domains (Figs. 2-11). The absence of curviplanar features in V15-55 is evidence that impact-related curviplanar features form at higher pressures (and thus later) than planar features in the microstructural sequence, and that V15-55 may, in fact, be outside of the zone of sufficient shock conditions for curviplanar feature formation.

vi. *Impact melt glass (IMG) inclusions*

IMG inclusions are typically not found in granular zircon from core samples (i.e. Figs. 2-12, 2-14). The recrystallization process appears to exsolve the melt from the granules. IMG inclusions are absent from V15-55, which could be due to a number of factors, including: 1) lower shock conditions (P/T not sufficient for melting or sufficient pathway (fracture) formation, 2) rock type, as there may be a lack of local low melting

temperature minerals to derive partial melt from (i.e. plagioclase, orthoclase), and 3) a different P/T pathway history, where the rarefaction wave has an absent or minimal effect on zircon, as evidenced by the lack of microtwins and curviplanar fracturing in this sample. IMG inclusions form soon after formation of planar and curviplanar features, and have been related to small-scale decompression melting of local minerals. More in-depth description and analysis of these IMG inclusions is provided in Chapter 3.

vii. *Grain margin displacement*

Displacement in zircon (e.g. Figs. 2-8, 2-11) has not been established as a definitive shock indicator, however the presence of displacement in shocked zircons and noted absence in unshocked grains indicates a probable shock-related formation mechanism. Displacement occurs along planar or curviplanar features, and is present in approximately 15-20% of the grains in the majority of the samples. There are relatively few zircons in V15-39 that exhibit displacement, largely due to the high post-shock temperatures and recrystallization in this sample. The majority of the displaced zircons in this study occur at contacts along grain boundaries (i.e. zircon in contact with plagioclase and orthoclase) (i.e. Fig. 2-11f). We suggest that the variable shock impedance contrasts between the minerals concentrates shock pressures and may increase the possibility of displacement along an open fracture. Displacement likely occurs somewhat contemporaneously with curviplanar feature formation, as planar features and twins are often crosscut by displaced boundaries (Fig. 2-4).

viii. *Crystal-plastic deformation*

Ductile deformation forms during the later modification stages of crater formation. Ductile deformation is expressed microstructurally as crystal plastic deformation (CPD),

and is present in almost all zircons analyzed with EBSD that were not affected by post-shock recrystallization. Microstructural evidence for the timing of CPD is provided by the deformation (bending) of microtwins (Fig. 2-3).

ix. *Recrystallization into coarse granular/polycrystalline zircon*

Outside of the UHT zone where high post-shock temperatures are present, granular or polycrystalline zircon is only found in some atypical zircons, and thus, we have defined two different primary mechanisms observed in this study for the formation of coarse granular/polycrystalline zircon, including:

1) partial to complete recrystallization due to high, regional post-shock temperatures (i.e. Figs. 2-12, 2-14).

2) partial recrystallization, primarily along a grain margin displacement zone (i.e. Fig. 2-11).

Within ~4-5 km from the centre of impact, zircons typically exhibit at least partial recrystallization, ranging up to complete recrystallization into large (40-50 μm) granules (Fig. 2-14). These granules are defined by their own, independent zonation patterns observable in BSE and CL (Fig. 2-15c), and have cores that appear brighter than their rims in BSE (Fig. 2-15c). These textures are unique, and are caused by prolonged exposure to high, regional post-shock temperatures from remnant heat related to the impact event, and are distinguishable from high-P finely-granular zircon identified in other studies of ejecta-type zircons (Bohor et al., 1993; Timms et al., 2012). It is interesting that a zircon from the crustal ILG bears similarities to impact melt-crystallized zircons from the Acraman impact melt sheet (Timms et al., 2014). These similiarities speak to the immense and prolonged post-shock temperatures present even at depth in the

crustal ILG rocks, which were not in direct contact with a cohesive melt sheet. The zone of zircon recrystallization at Vredefort matches relatively well with the “extreme” levels of quartz recrystallization identified by Grieve et. al (1990). V15-45-1, assumed to be taken from the approximate centre of impact, displays varying degrees of zircon recrystallization, but also displays a consistent lack of any shock microstructures. V15-39, located approximately 5 km from the proposed centre of impact, is still well within the ILG zone. The recrystallization of some domains in the zircon and not others highlights the heterogeneity of temperature effects at this radial distance (Fig. 2-11). It is noteworthy that there are a number of zircons that display planar features, displacement, and curviplanar features, which indicates that V15-39 (~5 km from centre) represents a transitional sample between large-scale zircon recrystallization and preservation of shock features. This relative lack of shock microstructural preservation is a result of the intense post-shock heating and recrystallization in this sample, to a lesser degree, but much like V15-45-1. We can thus establish an approximate limit of the large-scale UHT zircon recrystallization zone at ~4-5 km.

Zircon can also be recrystallized along a displacement zone formed from shearing along a previously opened fracture (Fig. 2-11). Shock pressures and temperatures may be focused along previously open fractures that represent a weakness in the zircon lattice due to shock impedance contrasts. Subsequently, localized recrystallization may occur due to an increased quantity of defects along this curviplanar fracture area, predisposing the area to the effects of high-temperature recrystallization. In both cases, overprinting relationships indicate that zones of recrystallization post-date the formation of any other shock-related

microstructure, and therefore share the same formation mechanism (extensive high post-shock temperatures) (Figs. 2-8, 2-10, 2-11, 2-15).

The samples analyzed in this study are placed on a regional cross section (Fig. 2-18). Temperature isotherms are estimates at 400 seconds post-impact, while isobars are suggested to be immediate peak pressures (Ivanov, 2005). Moser et al. (2011) have already indicated that the shock gradient proposed in this figure may be flawed, as evidenced by the presence of planar features and microtwins (20 GPa formation) outside of the 20 GPa isobar. These findings are reinforced by our microstructural observations as well. For example, zircons in V15-55 host multiple orientations of PF's (20 GPa), yet is outside the realm of the 20 GPa isobar on Fig. 2-18.

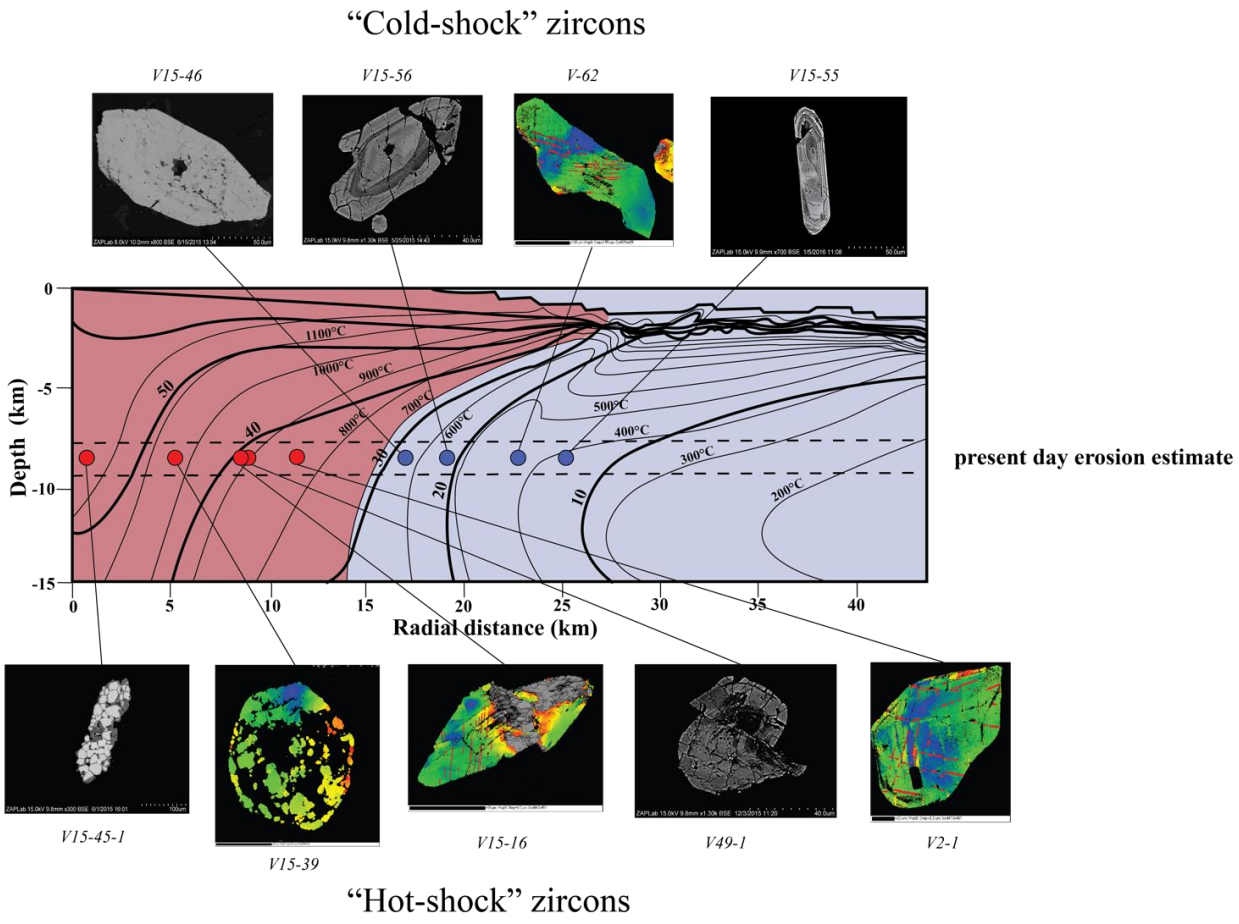

Figure 2-18: Regional cross-section map indicating location of samples as a function of radial distance and estimated pre-erosion depth. Estimated shock temperature (°C) and pressure (GPa) at ~400s post-impact are also shown on the diagram. Modified from Ivanov (2005), Gibson & Reimold (2008), Moser et al. (2011).

Within this general sequence of events, there are a number of different P/T shock pathways experienced in zircons from the Vredefort impact structure. For the purposes of this study, a pressure-time diagram was created to differentiate the microstructural progression in zircons from the "hot-shock" (i.e. V15-45-1), and "cold-shock" (i.e. V-62) locations identified by Moser et al. (2011) (Fig 2-19). This pressure-time diagram is adapted from Timms et al. (2012). A noted difference between the zircons in this study

and the those in the Timms et al. (2012) study is the microstructural sequence. This difference is likely attributable to the distinction between terrestrial zircons and lunar impact environments. A visual depiction of the observed crosscutting microstructural relationships as they relate to the pressure-time diagram is outlined in Figure 2-20.

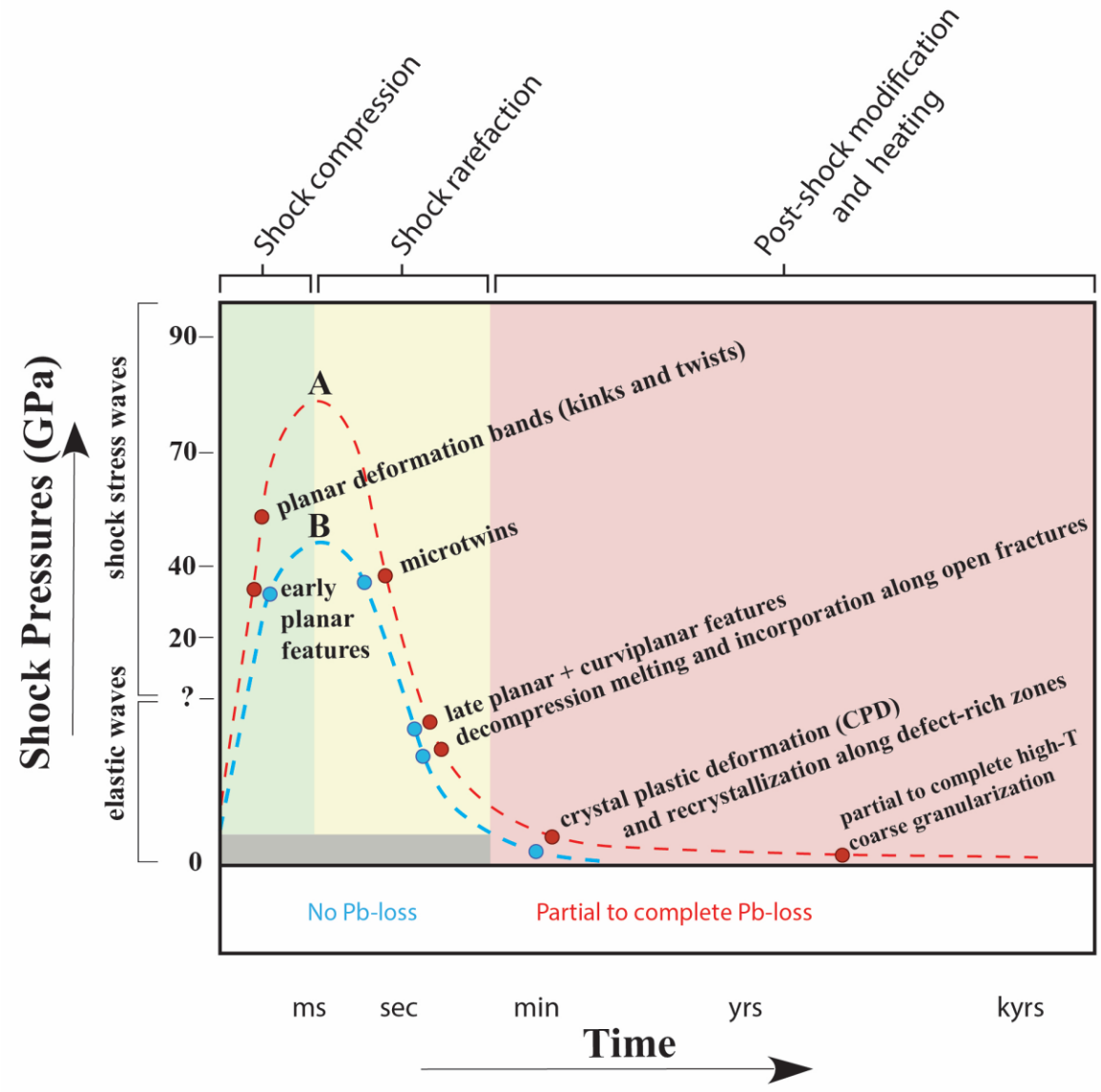

Figure 2-19: Pressure-time diagram showing shock pathways of a) a standard zircon from the "hot-shock" zircons (i.e. V15-45-1, V15-39, V2-1, V15-16), and b) a standard zircon from the "cold-shock" zircons (i.e. V15-46, V15-56, V-62). Modified from Timms et al. (2012).

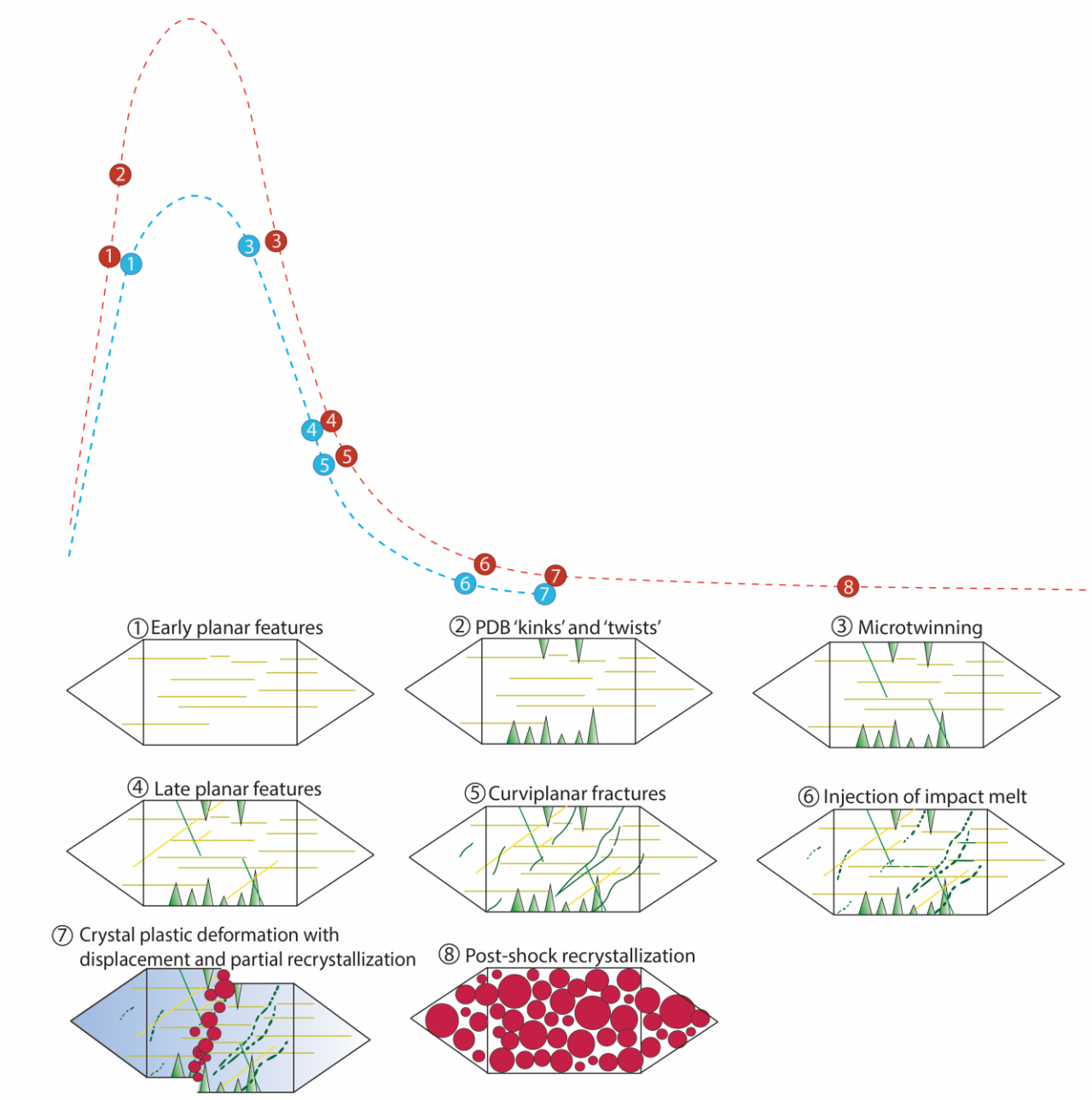

Figure 2-20: Microstructural progression in zircon from the Vredefort impact structure. a) Representative zircon from the core (i.e. V15-45-1), b) representative zircon from intermediate to collar locations (i.e. V2-1, V15-16, V-62). Relative sequence stages are listed, and colors identify the various mechanism for the formation of each microstructure: yellow=microstructures formed by initial shock

compression, green= microstructures formed by rarefaction wave and decompression, blue= microstructures formed by crater modification, red=microstructures formed by high post-shock temperatures.

2.6 Conclusion & Scientific Implications

We analyzed zircons from samples throughout the Vredefort central uplift, South Africa, and established a qualitative and quantitative guideline of microstructural progression. Cross-cutting relationships were observed to place the microstructures in a relative timeline, that was similar to previous reports (Moser et al. 2011). The standard zircon at Vredefort recorded the following progression: early planar features → planar deformation bands ('kinks' and 'twists'), likely coeval with early planar features → microtwinning → late planar features → curviplanar fracturing (and in some cases, grain margin displacement) → impact melt glass inclusion injection → ductile deformation (CPD) → post-shock recrystallization. A shock survey of ~40-50 zircons from 6 samples across the central uplift was conducted to understand the prevalence of various shock microstructures. The findings can be summarized as follows:

i. Planar features (early, late, and fractures) show a clear decrease in prevalence with increasing radial distance. They are present in zircons from ~24.5 km radial distance, indicating minimum shock pressures of 20 GPa at this location, which contradicts previous model-based shock estimates (Ivanov, 2005).

ii. Planar deformation bands, which can be separated into 'kinks' and newly documented 'twists,' but appear interrelated. Zircon PDB-twists are a newly documented microstructure found in 3 zircons in this study that post-date early planar features, but pre-date microtwins and curviplanar features, and appear to be related to grain-scale "twisting" of the zircon lattice.

iii. Microtwinning, formed during shock rarefaction, was present in many samples analyzed with EBSD, but absent from V15-39, V15-46, and V15-55.

iv. Curviplanar features, also formed during shock rarefaction are present in most samples but notably absent from V15-55.

v. Impact melt glass inclusions of locally-derived partial melt injected along curviplanar (and subsequently annealed planar fractures). Melt is formed due to decompression melting upon unloading of the shockwave, and thus relatively contemporaneous with curviplanar feature and twin formation. Again, impact melt glass inclusions are absent from V15-55.

vi. Displacement of grain margins, which may occur throughout the previous stages, but does, in some cases, post-date curviplanar fracturing.

vii. Crystal Plastic Deformation related to the crater modification stage is present in the majority of zircons not recrystallized by later post-shock temperatures.

viii. Recrystallization, which mainly operates in the ~4-5 km radius from the centre of impact, but which is variably present as partial recrystallization in some zircons from areas not affected by these post-shock UHT. Recrystallization is a direct result of heating to a point just below zircon's melting temperature (1676°C).

This study displayed some of the benefits of using zircon as a shock indicator in comparison to quartz. Zircon is much more resilient to post-shock temperatures, as indicated by the preservation of shock features up to ~4-5 km from the centre of impact where quartz grains are entirely recrystallized (Grieve et al., 1990). Zircons partially affected by recrystallization still retain a variety of shock microstructures, even if the surrounding minerals are completely recrystallized (Fig. 2-11f). The preservation potential of zircon is much better than quartz, and allows us to better constrain shock conditions.

The results of this study show that microstructural evidence refutes some of the shock-condition estimates based on numerical modeling (Ivanov, 2005). Planar fracturing in samples as far as 24.5 km from the centre of impact indicates that a minimum initial shock pressure of 20 GPa operated throughout the entirety of the Vredefort central uplift, and even into the collar rocks, meaning the shockwave likely did not dissipate to the degree previously estimated by Ivanov (2005). The discovery of shock evidence at this radial distance also indicates an absolute minimum of 4849-5310 km^3 of crust that hosts shocked zircon at Vredefort. Timms et al. (2012) created a shock progression sequence for lunar zircons. We determined that the microstructural sequence experienced by terrestrial, deep crater-floor zircons was much different than lunar zircons. Therefore, we recommend that the microstructural progression in lunar "ejecta-type" zircons be treated differently than those in standard terrestrial deep-crater environment zircons.

This study has significant implications for the future study of zircon in terrestrial crater environments. Progressing our understanding of U-Pb ages in shocked zircon requires studies such as this to advance our comprehension of the relationships between shock microstructures and U-Pb ages. Microstructural information in this study can be used to understand the cratering processes that generate such features, and the timescales associated with them. Moreover, the microstructural evidence presented in this study may be used as a basis for future applications to the study of impact craters on other rocky (lunar or Martian) surfaces, contributing advancements to the existing microstructural knowledge in these environments.

2.7 References

Abramov, O., Kring, D. A., & Mojzsis, S. J., 2013. The impact environment of the Hadean Earth. *Chemie der Erde-Geochemistry*, *73*(3), 227-248.

Bohor, B. F., Betterton, W. J., & Krogh, T. E., 1993. Impact-shocked zircons: discovery of shock-induced textures reflecting increasing degrees of shock metamorphism. *Earth and Planetary Science Letters, 119*(3), 419-424.

Cavosie, A. J., Quintero, R. R., Radovan, H. A., & Moser, D. E., 2010. A record of ancient cataclysm in modern sand: Shock microstructures in detrital minerals from the Vaal River, Vredefort Dome, South Africa. *Geological Society of America Bulletin, 122*(11-12), 1968-1980.

Cavosie, A. J., Erickson, T. M., & Timms, N. E., 2015. Nanoscale records of ancient shock deformation: Reidite (ZrSiO4) in sandstone at the Ordovician Rock Elm impact crater. *Geology*, *43*(4), 315-318.

El Goresy, A., 1965. Mineralbestand und Strukturen der Graphit-und Sulfideinschlüsse in Eisenmeteoriten. *Geochimica et Cosmochimica Acta*, *29*(10), 1131-1151.

Erickson, T. M., Cavosie, A. J., Moser, D. E., Barker, I. R., & Radovan, H. A., 2013. Correlating planar microstructures in shocked zircon from the Vredefort Dome at multiple scales: Crystallographic modeling, external and internal imaging, and EBSD structural analysis. *American Mineralogist*, *98*(1), 53-65.

Frey, H., 1980. Crustal evolution of the early Earth: The role of major impacts. *Precambrian Research*, *10*(3-4), 195-216.

Gibson, R. L., Reimold, W. U., & Stevens, G., 1998. Thermal-metamorphic signature of an impact event in the Vredefort dome, South Africa. *Geology, 26*(9), 787-790.

Grieve, R. A., Dence, M. R., & Robertson, P. B., 1977. Cratering processes-As interpreted

from the occurrence of impact melts. In *Impact and explosion cratering: Planetary and terrestrial implications* (pp. 791-814).

Gibson, R. L., & Reimold, W. U., 2008. *Geology of the Vredefort impact structure: A guide to sites of interest* (Vol. 97). Council for Geoscience.

Glass, B. P., Liu, S., & Leavens, P. B., 2002. Reidite: An impact-produced high-pressure polymorph of zircon found in marine sediments. *American Mineralogist, 87*(4), 562-565.

Grieve, R. A. F., Coderre, J. M., Robertson, P. B., & Alexopoulos, J., 1990. Microscopic planar deformation features in quartz of the Vredefort structure: Anomalous but still suggestive of an impact origin. *Tectonophysics, 171*(1), 185-200.

Hart, R. J., Welke, H. J., & Nicolaysen, L. O., 1981. Geochronology of the deep profile through Archean basement at Vredefort, with implications for early crustal evolution. *Journal of Geophysical Research: Solid Earth, 86*(B11), 10663-10680.

Hart, R. J., Andreoli, M.A.G., Reimold, W. U., & Tredoux, M., 1991. Aspects of the dynamic and thermal metamorphic history of the Vredefort cryptoexplosion structure: implications for its origin. *Tectonophysics, 192*(3-4), 313-331.

Hart, R.J., Andreoli, M.A.G., Tredoux, M., & De Wit, M.J., 1990. Geochemistry across an exposed section of Archean crust at Vredefort: with implications for mid-crustal discontinuities. *Chemical Geology, 82*, 21-50.

Ivanov, B. A., 2005. Numerical modeling of the largest terrestrial meteorite craters. *Solar System Research*, *39*(5), 381-409.

Kamo, S. L., Reimold, W. U., Krogh, T. E., & Colliston, W. P., 1995. Shocked zircons in Vredefort pseudotachylite and the U-Pb zircon age of the Vredefort impact event. *Proceedings, Centennial Geocongress: Johannesburg, Geological Society of South Africa*, 566-569.

Kamo, S. L., Reimold, W. U., Krogh, T. E., & Colliston, W. P., 1996. A 2.023 Ga age for the Vredefort impact event and a first report of shock metamorphosed zircons in pseudotachylitic breccias and granophyre. *Earth and Planetary Science Letters, 144*(3), 369-387.

Kovaleva, E., Klötzli, U., Habler, G., & Wheeler, J., 2015. Planar microstructures in zircon from paleo-seismic zones. *American Mineralogist, 100*(8-9), 1834-1847.

Krogh, T. E., Davis, D. W., & Corfu, F., 1984. Precise U-Pb zircon and baddeleyite ages for the Sudbury area. In *The geology and ore deposits of the Sudbury structure* (Vol. 1, pp. 431-446). Ontario Geological Survey.

Krogh, T. E., Kamo, S. L., Sharpton, V. L., Marin, L. E., & Hildebrands, A. R., 1993. U-Pb ages of single shocked zircons linking distal K/T ejecta to the Chicxulub crater. *Nature*, *366*, 731-734.

Lana, C., Reimold, W. U., Gibson, R. L., Koeberl, C., & Siegesmund, S., 2004. Nature of the Archean midcrust in the core of the Vredefort Dome, central Kaapvaal Craton, South Africa. *Geochimica et Cosmochimica Acta, 68*(3), 623-642.

Leroux, H., Reimold, W. U., Koeberl, C., Hornemann, U., & Doukhan, J. C., 1999. Experimental shock deformation in zircon: a transmission electron microscopic study. *Earth and Planetary Science Letters*, *169*(3), 291-301.

Marchi, S., Bottke, W.F., Elkins-Tanton, L.T., Bierhaus, M., Wuennemann, K., Morbidelli, A., & Kring, D.A., 2014. Widespread mixing and burial of Earth's Hadean crust by asteroid impacts. *Nature, 511*(7511), 578-582.

Martini, J. E., 1978. Coesite and stishovite in the Vredefort dome, South Africa. *Nature*, *272*, 715-717.

Moser, D. E., 1997. Dating the shock wave and thermal imprint of the giant Vredefort impact, South Africa. Geology, 25(1), 7-10.

Moser, D. E., Cupelli, C. L., Barker, I. R., Flowers, R. M., Bowman, J. R., Wooden, J., & Hart, J. R., 2011. New zircon shock phenomena and their use for dating and reconstruction of large impact structures revealed by electron nanobeam (EBSD, CL, EDS) and isotopic U-Pb and (U-Th)/He analysis of the Vredefort dome. *Canadian Journal of Earth Sciences, 48*(2), 117-139.

Nemchin, A., Timms, N.E., Pidgeon, R., Geisler, T., Reddy, S.M., and Meyer, C., 2009. Timing of crystallization of the lunar magma ocean constrained by the oldest zircon. *Nature Geoscience, 2*, 133–136.

Pace, N.R., 1997. A molecular view of microbial diversity and the biosphere, *Science, 276*, 333–336.

Pidgeon, R.T., Nemchin, A.A., & Kamo, S.L., 2011. Comparison of structures in zircons from lunar and terrestrial impactites. *Canadian Journal of Earth Sciences, 48,* 107-116.

Schreyer, W., 1983. Metamorphism and fluid inclusions in the basement of the Vredefort dome, South Africa: Guidelines to the origin of the structures. *Journal of Petrology, 24*(1), 26-47.

Spray, J., & Hines, J., 2009. Earth impact database. *Planetary and Space Science Centre. University of New Brunswick, Canada.*

Stepto, D., 1979. A geological and geophysical study of the central portion of the Vredefort Dome Structure. Ph.D. thesis, University of the Witwatersrand.

Stevens, G., Gibson, R.L., & Droop, G.T.R., 1997. Mid-crustal granulite facies metamorphism in the Central Kaapvaal craton: the Bushveld Complex connection. *Precambrian Research, 82,* 113-132.

Stöffler, D., 1971. Progressive metamorphism and classification of shocked and brecciated crystalline rocks at impact craters. *Journal of Geophysical Research, 76*(23), 5541-5551.

Stöffler, D., & Langenhorst, F., 1994. Shock metamorphism of quartz in nature and experiment: I. Basic observation and theory. *Meteoritics, 29*(2), 155-181.

Therriault, A.M., Grieve, R.A.F., & Reimold, W.U., 1997. Original size of the Vredefort structure: implications for the geological evolution of the Witwatersrand Basin. *Meteoritics & Planetary Science, 32,* 71-77.

Timms, N.E., Erickson, T.M., Schmieder, M., Tohver, E., Pearce, M., 2014. Shock recrystallisation and decomposition of zircon. *77th Annual Meteoritical Society Meeting.*

Timms, N. E., Reddy, S. M., Healy, D., Nemchin, A. A., Grange, M. L., Pidgeon, R. T., & Hart, R., 2012. Resolution of impact-related microstructures in lunar zircon: A shock-deformation mechanism map. *Meteoritics & Planetary Science, 47*(1), 120-141.

Tredoux, M., Hart, R. J., Carlson, R. W., & Shirey, S. B., 1999. Ultramafic rocks at the center of the Vredefort structure: Further evidence for the crust on edge model. *Geology, 27*(10), 923-926.

Turner, G., Cadogan, P.H., Yonge, C.J., 1973. Argon selenochronology. In *Lunar and Planetary Science Conference Proceedings* (Vol. 4, pp. 1889).

Valley, J.W., Cavosie, A.J., Ushikubo, T., Reinhard, D.A., Lawrence, D.F., Larson, D.J., Clifton, P.H., Kelly, T.F., Wilde, S.A., Moser, D.E., & Spicuzza, M.J., 2014. Hadean age for a post-magma-ocean zircon confirmed by atom-probe tomography. *Nature Geoscience, 7,* 219-223.

Wielicki, M.M., & Harrison, T.M., 2015. Zircon formation in impact melts: Complications for deciphering planetary impact histories. *Geological Society of America Special Papers, 518,* 127-134.

Wittmann, A., Stoffler, D., Schmitt, R. T., Tagle, R., Kenkmann, T., & Hecht, L., 2004. Zircon as a shock indicator in impactites of drill core Yaxcopoil-1, Chicxulub impact structure, Mexico (abstract# 1742). In *35th Lunar and Planetary Science Conference.*

Wittmann, A., Kenkmann, T., Schmitt, R. T., & Stöffler, D., 2006. Shock-metamorphosed zircon in terrestrial impact craters. *Meteoritics & Planetary Science, 41*(3), 433-454.

Chapter 3

3 Impact melt glass inclusions in zircon from the central uplift of the Vredefort impact structure, South Africa

Connor L. Davis and Desmond E. Moser

3.1 Introduction

A significant component of the energy of a meteorite impact with planetary crust is accommodated in the generation of impact melts (Dence, 1971; Grieve et al., 1977; Grieve and Cintala, 1992). These melts differ from endogenic melts in that they carry signatures of the much higher temperatures (>2000°C) and sometimes unique chemistry derived from impact melting of the target (French, 1998). A large body of research has described such macroscopic impact melt-rich features in the ejecta deposits (e.g. spherules and tektites) and crater facies (suevites), as well as the kilometres-thick impact melt sheets that fill large craters (French, 1998). Another aspect of impact melting, however, is at the microscopic level in the form of residual impact melt trapped within shocked minerals. This field has been explored in main phase minerals such as pyroxene and plagioclase in meteoritic samples (El Goresy et al., 2013), but much less attention has been directed to such features in accessory minerals such as zircon. Impact-generated glass inclusions of melted host rock have recently been reported for zircon from the

terrestrial Vredefort impact structure (Moser et al., 2011) and Apollo lunar soil samples (Crow et al., in press).

Zircons preserve diagnostic shock features, which have the ability to persist over billions of years, through cycles of tectonism (Krogh et al., 1984), erosion, transport, and incorporation into a new sedimentary host rock (Cavosie et al., 2010; Thomson et al., 2014; Erickson et al., 2015). The possibility that they may also carry melt products and a compositional fingerprint of their source crater as impact-melt glass inclusions raises the prospect of a potentially valuable tool for reconstructing impact conditions and provenance using *ex-situ* grains from sediments and meteorites. The specific zircon that yielded the original discovery of impact-melt glass (IMG) inclusions was discovered near the center of the central uplift of the 2.02 Ga Vredefort impact structure, in a loose grain separated from Archean granitoid for the purpose of geochronology (Moser et al., 2011). Regional mapping of these IMG inclusions shows that they are widespread in the central uplift out to a radial distance of 23 km but that they range in size and abundance (Chapter 2; Davis & Moser, in prep.). The purpose of this study is to characterize the chemistry of these features in the 'type' zircon near the centre of impact from Moser et al. (2011) and at two other sites at greater radial distance as a first step to understanding the origin of these novel and poorly-understood products of impact.

3.2 Geological Setting & Background

The Vredefort impact structure (S27°0', E27°30') is located approximately 120 km southwest of Johannesburg, South Africa. An ~25 km wide quasi-annular group of topographically high supracrustal rocks surrounds an ~45 km wide inner core of Archean gneisses (Gibson & Reimold, 2008), together representing the deeply eroded central

uplift of the once larger Vredefort impact structure, estimated to be between 250-300 km in diameter (Therriault et al., 1997). The ~2.020 Ga impact crater has experienced erosion to a depth of ~8-10 km (Gibson et al., 1998), and now exposes mid to lower crustal rocks in the core (amphibolite to granulite-facies, respectively). The exposure of amphibolite rocks surrounding granulite rocks is thought to have occurred by exhumation during the Vredefort impact event, highlighting the magnitude of this event (Stepto, 1979; Hart et al., 1981; Lana et al., 2004). The discovery of harzburgite and other upper mantle ultramafic rocks at the center of the dome provided further evidence for this "crust-on-edge" model (Hart et al., 1991; Tredoux et al., 1999). The impact melt sheet, which is assumed to have been quite extensive, has now long been eroded. However, there remains various other local evidence of impact melting throughout the structure, including: foliated norite impact melt rocks (Moser, 1997); granophyre with a meteoritic component (Koeberl et al., 1996); Inlandsee Leucogranofelsic Gneisses, which have been shown to host domains of partial melting (Kamo et al., 1996); and partial melting in the Central Anatectic Granite (Gibson, 1997).

3.3 Zircon and melt inclusions

Zircon is widely recognized as being the most physically and chemically resilient minerals on Earth, as evidenced by ~4.4 Ga Hadean zircons that are the oldest known pieces of our planet (Wilde et al., 2001). These grains have preserved their primary chemical features such as zoning and inclusions despite repeated travel through the rock cycle (Valley et al., 2014). The remarkable range of internal features in zircon that remain stable through geologic time has expanded to include chains of impact-generated inclusions that have remained in a glass state for over 2 billion years (Moser et al., 2011).

These are very different from primary melt inclusions that have long been recognized in igneous zircons from magma chambers (Thomas et al., 2003). Dependent primarily upon cooling rate, primary igneous inclusions can occur as a crystalline, single-phase glass, or a multi-phase mineral inclusions of co-crystallizing phases such as apatite, feldspar and quartz (Thomas et al., 2003). Primary igneous inclusions are randomly distributed and their boundaries are discordant to concentric growth zoning, indicating that the phases were captured or surrounded during growth of zircon and cooling of the parent magma.

Impact-related melting is invariably related to the unloading (decompression) phase of shock metamorphism (Grieve et al., 1977) in that, while the pressure wave releases within microseconds, the residual temperature rise of >2000°C remains, prompting instantaneous melting. The impact melt glass inclusions from the Vredefort impact structure were found spatially related to shock microstructures such as curviplanar features and along offsets related to microtwin domains. The association of the inclusions with the microstructures that are ‘late’ in the shock metamorphic sequence, such as curviplanar features, led to the proposal that they were generated and injected during the shock wave rarefaction (unloading) stage of the impact (Moser et al., 2011). Local derivation of the melt from the host granitoid gneiss was presumed based on the broad similarity of inclusion chemistry to the host granitoid. The glass (amorphous) state of the inclusion material was determined based on electron backscatter diffraction (EBSD) results using a step size as low as 60 nm and unpublished laser Raman spectroscopy carried out with Prof. S. Shieh (Moser, personal communication). It was recognized that melt inclusions could be useful indicators of shock conditions based on the melting temperature of the incorporated melted minerals, and potentially relate the zircons to their

original, partially melted host rock, but much more understanding of these features was necessary. Since the initial report of this new melt inclusion type in a separated zircon grain, there has not been an in-depth study of the local and regional variation in morphology, composition and method of emplacement of these inclusions, and no study of such features in zircon still contained (i.e. *in- situ*) in its host rock.

3.4 Samples & Standards

Ten samples were selected (Table 3-1, Figure 3-1) of granitoid composition (+1 quartzite) to limit any bias that rock type may have on shock metamorphic response of the zircons.

Sample	Lithology	Sample Type	Distance from center	Coordinates (UTM)	
V15-45-1	ILG	Thin Section	<1.0 km	550161 m E	7011662 m S
V09-237*	ILG	Grain Mount	~4.0 km	549589 m E	7006647 m S
V15-39	ILG	Thin Section	~5.0 km	543699 m E	7014140 m S
V15-16	ILG	Thin Section	~8.6 km	540091 m E	7010527 m S
V49-1	Charnockite	Thick Section	~8.9 km	542531 m E	7010527 m S
V2-1*	Charnockitic Gneiss	Thick Section	~11.4 km	540804 m E	7019340 m S
V15-46	OGG	Thin Section	~17.1 km	539943 m E	7025719 m S
V15-56	OGG	Thin Section	~19 km	560295 m E	7025905 m S
V-62*	Alkali Syenogranite	Thick Section	~22.8 km	563809 m E	7030330 m S
V15-55	Quartzite	Thin Section	~24.5 km	563809 m E	7030330 m S

Table 3-1: Samples included for impact melt glass inclusion analysis. Included in this table are the sample number, sample type, distance from the center of impact, and UTM coordinates. ILG=Inlandsee Leucogranofels, OGG=Outer Granite Gneiss. *=samples included in compositional and in-depth microstructural analysis.

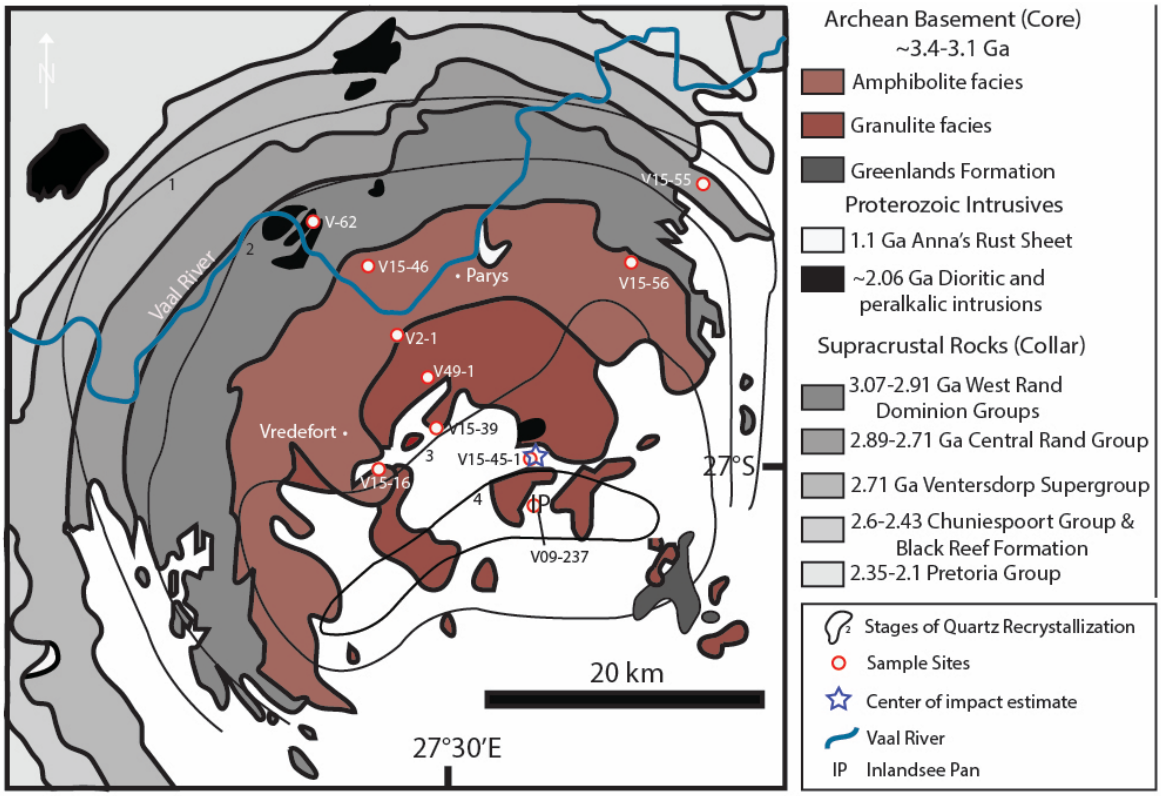

Figure 3-1: Geologic bedrock map of Vredefort impact structure, South Africa, showing the locations of samples used in this study. Map adapted from Moser et al. (2011) and Grieve et al. (1977).

Glass standard materials were cast in an epoxy plug, following the same preparation procedure as the samples. Standards used are listed in Table 3-2. Some mineral standards were used in certain cases. No glass standard was found with sufficient wt. % K for quantitative results, hence the use of a mineral K standard. It was also difficult to get accurate measurements for Fe, as the Kα line could not be used at the lower accelerating voltage (7 kV) at which this study operated. All Zr would have come from the mineral zircon, and as such, the zircon mineral standard was used.

Element	Glass Standard Reference
K	SEM mineral std. MAD-10 feldspar
Mg	K-412
Na	K-373
Fe	SEM mineral std. Fe
Si	NMNH Rhyolite (VG-568)
Al	K-495
Ca	K-411
Zr	SEM mineral std. zircon

Table 3-2: Table displaying the elements standardized in this study, and their corresponding glass standard reference. Glass standard sources are SPI supplies, C. M. Taylor Company, and Jarosewich (2002). Mineral standards were built-in standards within the SEM.

3.5 Methods

Samples were prepared as both thin and thick sections (+1 epoxy grain mount), polished with a Buehler VibroMet 2 vibratory polisher and carbon coated to ~25 nm with an Edwards Auto 306 carbon coater. Based on the regional shock microstructural survey (Chapter 2), representative grains were selected from select samples across the Vredefort central uplift for energy dispersive spectroscopy (EDS) analysis.

All grains were characterized in the Western University's Zircon and Accessory Phase Laboratory (ZAPLab) with a Hitachi SU6600 field emission gun scanning electron microscope (FEG-SEM). Analyses performed on these grains included secondary electron (SE) and backscattered electron (BSE) imaging, cathodoluminescence mapping (CL), electron backscatter diffraction (EBSD), and energy dispersive X-ray spectroscopy (EDS). EDS was performed for hundreds of inclusions from a variety of zircons throughout the Vredefort dome. The conditions for each of the basic imaging analyses are

listed in Table 3-3. EBSD analysis were performed with a Nordlys HKL system and Channel 5 software. EBSD data are uncorrected with the exception of wild spike noise reduction. Development of the EDS method and EDS conditions are described in Section 3.6.1 and Table 3-4.

	BSE/SE	CL	EBSD
SEM Detector	BSE/SE detector	Gatan ChromaCL	Oxford HKL Nordys electron detector
Carbon coat	~25 nm	~25 nm	~25 nm
Acc. voltage	15 kV	10 kV	20 kV
Probe current	Variable	3.5-4.3 nA	~12 nA
Tilt	--	--	70°
Working distance	10.0 mm	12.5 mm	19.0 mm
Apertures	3/1 (50 µm/200 µm)	2/3 (100 µm/50 µm)	3/2 (50 µm/100µm)
Gain	Medium	Medium	Medium

Table 3-3: Hitachi SU6600 FEG-SEM analysis conditions. Advanced EBSD parameters are provided in Chapter 1.

3.6 Results

3.6.1 Methodology development

Two categories of sample preparation and method development were necessary to perform this study. These involved modified polishing and coating techniques to permit electron beam micro-analysis while simultaneously refining electron beam conditions to permit qualitative and semi-quantitative elemental analysis by SEM-EDS.

3.6.1.1 Polishing and carbon coat methodology

It is difficult to properly polish melt inclusions in zircon due to the heterogeneity in hardness difference between the inclusions and host zircon. Basic polishing (9, 6, 1 and

0.25 μm) does not preferentially polish the μm-submicron melt inclusions, however a problem arises with the fine (0.05 μm) vibratory polish that is necessary for EBSD imaging. Standard ZAPLab vibratory polishing time for EBSD preparation is between 2.5-3 hours, using a basic aqueous solution of colloidal alumina. For the purposes of this study, it was found that a more neutral NaOH solution minimized inclusion destruction, and samples were polished for ~1-1.5 hours in order to avoid preferential polishing of the inclusions. EBSD images were not adversely affected by the lower vibratory polishing period. In fact, all mean angular deviation values (a measure of fit between the observed electron diffraction pattern and the ideal reference value) were between <0.2-0.5°, well below the threshold for zircon of 1.3°.

Knowledge and control of carbon coat thickness on samples is necessary in order to correct for X-ray absorption during EDS analysis and perform semi-quantitative elemental analyses of inclusions. The carbon coat was applied using an Edwards Auto 306 carbon coater, which does not have a thickness measurement device. The optimal carbon coat thickness for EDS analysis has been suggested to be ~20-25 nm (Kerrick et al., 1973). Carbon thicknesses on samples and standards in this study were determined by simultaneously coating a pure silicon chip and measuring coat thickness within the SEM, using a program developed and shared by Dr. Yves Thibault. Reproducibility of coat thickness was ensured by observing the interference colours on a polished brass disc (Kerrick et al., 1973). For the purposes of this study, samples were coated with a consistent ~25 nm thickness, as it is this thickness that produces the most noticeable interference colour change (Kerrick et al., 1973).

3.6.1.2 Development of energy dispersive spectroscopy (EDS) for μm to sub-μm impact melt glass inclusions in zircon

The EDS technique is known to be an excellent method for measuring the major element compositions of glass inclusions (Spray & Rae, 1995). Quantitative compositional analysis with such electron beam methods is, however, challenging in the analysis of small (μm-to-submicron) and shallow inclusions. This difficulty is because the target domain is similar or sometimes smaller than the spatial resolution of EDS due to electron scattering beneath the sample surface and excitation of X-rays to a distance of ~1 μm from the point of incidence of the ~1 nm diameter beam. In order to combat these issues, the following procedures for EDS mapping and semi-quantitative EDS were developed.

3.6.1.2.1 Energy dispersive spectroscopy (EDS) mapping

Qualitative EDS mapping provides an excellent method to visually characterize the compositional variations in IMG inclusions. Due to the microscopic scale of these inclusions, SEM beam conditions must be tailored and consistent. Table 3-4 lists the settings used for EDS mapping of zircon, melt inclusions, and surrounding minerals. These settings are recommended as the best settings for IMG inclusion characterization in that they minimize activation volume effects while maximizing signal intensity. For example, 7 kV was used for the semi-quantitative analysis, as using a lower accelerating voltage will decrease the interaction volume of the beam (Fig. 3-2). The settings in Table 3-4 were developed to reduce compositional inaccuracy.

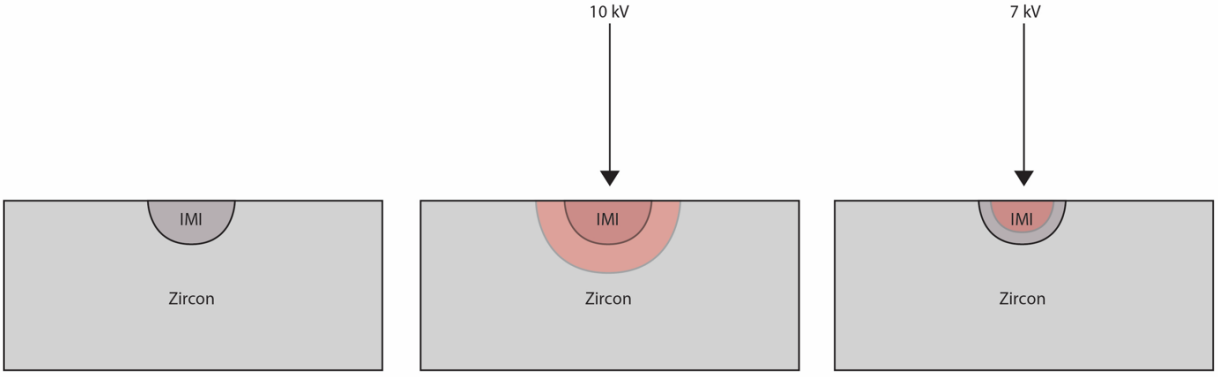

Figure 3-2: Schematic showing the difference in interaction volume (red) between 10 kV and 7 kV accelerating voltages. With 10 kV, a significant component of surrounding zircon would be included in impact melt glass inclusion (IMG) analysis. 7 kV acts to eliminate this zircon component.

3.6.1.2.2 Semi-quantitative energy dispersive spectroscopy (EDS)

There are a number of factors that must be considered when quantifying the major element chemistry of submicron-µm sized melt inclusions. Based on previous studies, many of the inclusions are assumed to be glass, and thus we must account for, and minimize well known beam-alteration effects on glass such as local alkali (Na and K) mobility. A block of glass standards (Table 3-3) was therefore created to most closely match the compositions of the melt inclusions. Two to three replicate measurements of each spot were taken of glass standards and melt inclusions, in an effort to control and record alkali mobility. Figure 3-3 displays an example of alkali mobility in one of the standards. The decline in Na wt. % is essentially negligible for the purposes of this study. Due to the difficulty of directly measuring oxygen in glasses, oxygen was calculated by stoichiometry, as we assume the source of these inclusions was their local mineral counterparts. All analyses were normalized to 100%. Normalization was performed

because totals were typically low. Low totals in glass analysis are generally accepted and attributed to the presence of H_2O or a loss of alkalis (Nash, 1992).

	EDS mapping	Semi-quantitative EDS
Detector	X-max SSD detector (Oxford Instruments)	X-max SSD detector (Oxford Instruments)
Carbon coat thickness	~25 nm	~25 nm
Accelerating voltage	10 kV	7 kV
Probe current	Variable	Variable (typically ~0.10 nA)
Working distance	10.0 mm	10.0 mm
Apertures	2/1(100 µm/200 µm)	4/3 (30µm/50µm)
Gain	Medium 6.0	Medium 6.0
Image res.	512x512	512x512
Process time	5 seconds	5 seconds
Map dwell	100 µs	--
Linescan dwell	2000	--
Frames	6.55 sec/frame	1 frame (26.7 sec/frame)
Spectrum range	0-20 keV	0-20 keV

Table 3-4: Advanced settings used for EDS mapping and semi-quantitative EDS analysis. Variable magnification was used.

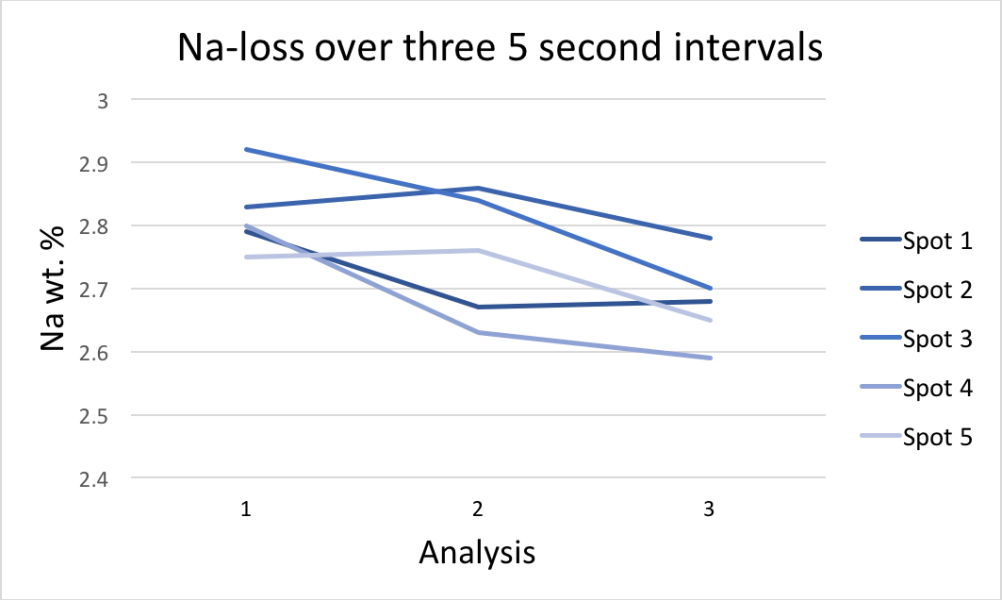

Figure 3-3: Na-loss in five different spots on the K-373 standard. Three repeat analyses (5 seconds each) were performed to mimic the impact melt glass inclusions analysis. Na shows a distinct decline in weight % over time, however the values are essentially negligible for the purposes of this study.

3.6.2 Results of FEG-SEM analysis

3.6.2.1 Regional distribution of impact melt glass inclusions

IMG inclusions are absent in the samples affected by ultra-high temperature (UHT) post-shock heating and extensive recrystallization. Where zircon grains are recrystallized into granular (polycrystalline) zircon (i.e. V15-45-1), impact melt inclusions are not present (Fig. 3-3d). The first (nearest to the center of impact) occurrence of IMI's at Vredefort is in V09-237 and V15-39. These samples are ~4 and 5 km from the center of impact, respectively, and host impact melt inclusions in some zircons, but not all. IMI's are present in all other samples analyzed in this study, except V15-55 (Fig. 3-4a). There appears to be more extensive (larger, higher abundance) of melt inclusions in zircons from samples spatially associated with pseudotachylite (Fig. 3-4b, c), indicating a

potential correlation between macroscale melting and partial melting on the microscale. Inclusions vary in prevalence, morphology, spatial distribution, size, and composition from sample to sample. A subset of the samples included in this study were chosen for an in-depth study of ~50 zircons (Figure 3-5), described in full in Chapter 2, which displays the high prevalence of impact melt inclusions in all samples except the intensely recrystallized (V15-39) and lower shock environment quartzite (V15-55). There is an almost perfect correlation between curviplanar fractures and impact melt inclusion prevalence that can be traced across the impact structure (Fig. 3-5).

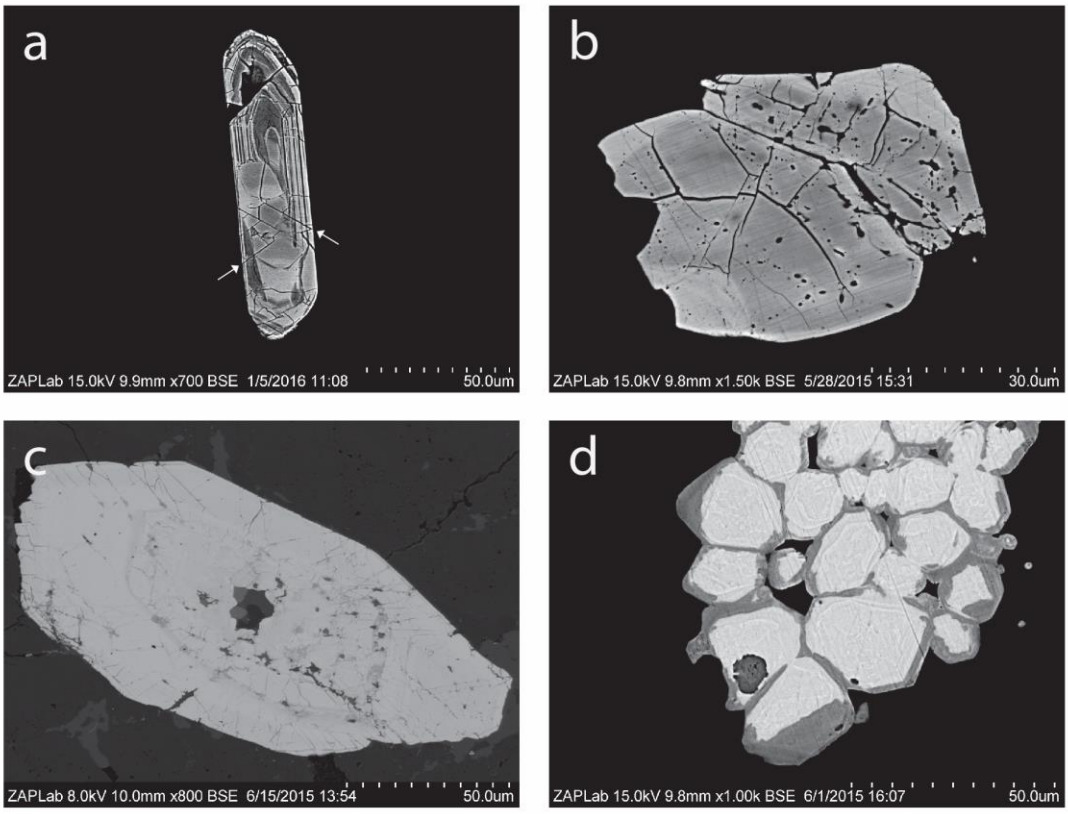

Figure 3-4: a) BSE image of V15-55 zircon grain displaying some planar fracturing but no IMG inclusions, b) and c) BSE images of zircons F24565 and F725, respectively, from pseudotachylite rich showing chains of elongate and ovoid IMG

inclusions, and some filling fractures, d) BSE (zoom) image of V15-45-1 F445

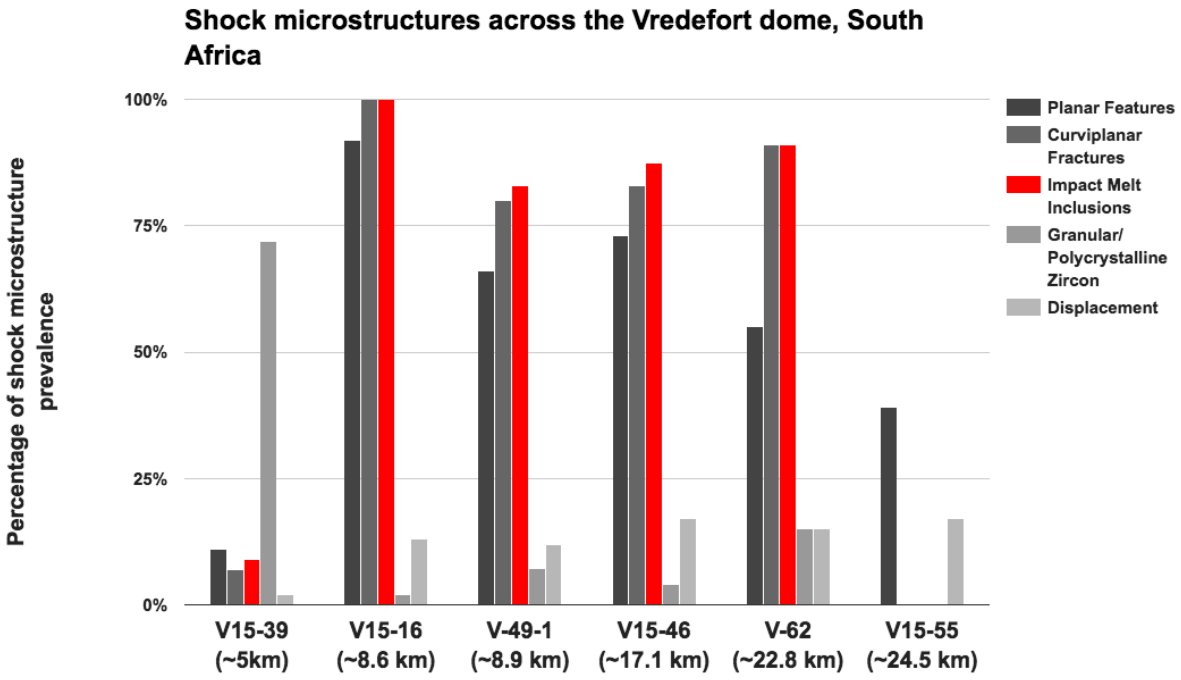

showing coarse granular texture zircon without IMG inclusions.

Figure 3-5: Bar graph displaying the percentage of each microstructure from ~50 grains of each sample.

3.6.2.2 Impact melt glass (IMG) inclusions at three sites across the central uplift

Impact melt glass inclusions were found in zircons in granitoid samples at radial distances between 4 km and 23 km in the central uplift (Chapter 2) (Fig 3-5). Zircons from V09-237, V2-1, and V-62 were selected to represent the core (~4.0 km radial distance), intermediate (~11.4 km radial distance) and collar (~22.8 km radial distance) locations, respectively. The three samples also represent varying granitoid compositions, including Inlandsee Leucogranofels (ILG) (V09-237), charnockitic gneiss (V2-1), and

syenogranite (V-62). A detailed investigation into the type (morphology, crystallinity, size, distribution), and composition (EDS mapping, semi-quantitative EDS) of IMG inclusions was performed on representative zircons from each sample.

3.6.2.2.1 Collar sample: V-62 F3440 and F123

V-62 is a syenogranite from ~23 km radial distance from the center of impact, originally a sill intruded into the deep levels of the Witwatersrand basin and rotated to a vertical attitude in the collar of the central uplift. Zircons are almost invariably hosted within pyroxene (aegerine, $NaFeSi_2O_6$) which appears to exhibit similar shock features and melt inclusions as many of the zircon grains (Fig. 3-6a, e, f). The zircon shock features include planar features such as microcleavage and microtwins, but melt inclusions are the most prominent impact-related features. There are, however, distinct morphological differences in these inclusions compared to samples closer to the center of impact. The size of the inclusions in V-62 are much smaller (1 μm or less on average) and the contacts with zircon are generally highly irregular as they are commonly bounded within fracture networks. Two zircons were chosen to represent the types of microstructures and inclusions characteristic of the population.

F3440 is an irregularly shaped zircon at a boundary between aegerine and a Na-rich aluminosilicate melt phase (Fig. 3-7). Criteria used to define IMG inclusions includes a spatial association with shock microstructures, and the absence of an electron diffraction pattern when analyzed using EBSD consistent with an absence of atomic order. In this case, there are two types of domains that meet these criteria; amorphous, submicron diameter inclusions within the zircon and aegerine, and domains along the zircon grain margin that lead into fractures. These glass domains are composed of Na-Al-O-Si,

distinct from feldspar and pyroxene by the absence of Ca and Fe, respectively. Both types of impact melt glass domains have margins, or are infilling features, that post-date both primary igneous zoning in the zircon (Fig 3-6c) and shock microstructures such as microtwins (Fig. 3-6 d).

The vast majority of the inclusions in this zircon are submicron, with occasional larger ‘pods’ of impact melt presiding within the center of grains. Open fractures in the zircon lattice appear to offer a principal pathway for impact melt into the zircon. These large, open fractures may be related to planar and curviplanar features present elsewhere in the grain in similar orientations. For instance, the large fracture emanating from the top right of the grain in Fig. 3-6 appears to coincide with the orientation of microtwins and planar features (Fig. 3-6 d, e, f). Regular curviplanar features, planar features and microtwins host the typically ovoid, submicron inclusions. The size of the IMG inclusions was below the spatial resolution for semi-quantitative EDS analysis however qualitative inspection indicated that the inclusions are similar in major element chemistry to the fracture-filling material (Fig. 3-7), with the exception of slight Al-variations.

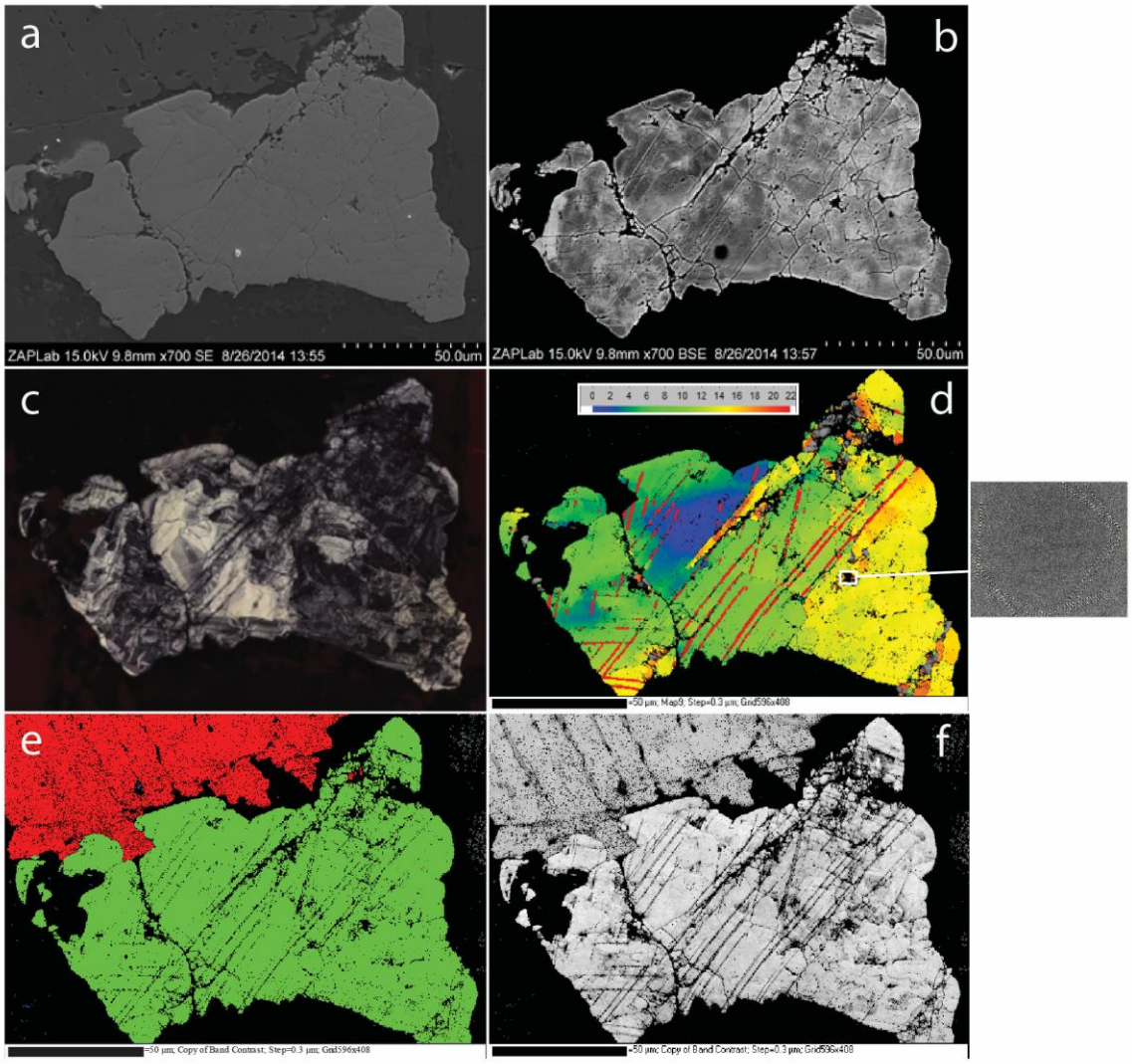

Figure 3-6: Electron beam data for V-62 F3440 a) SE image showing network of fractures and planar features in-filled with a secondary phase, b) BSE image indicating a low density (average Z) for the phase infilling fractures c) CL image showing primary igneous trace element zoning cross-cut by microtwins (linear zones of lower intensity), d) EBSD misorientation map image showing crystal plastic deformation, "bent" microtwins (red lines), local planar subgrain boundaries off-setting twins, and amorphous (black) inclusions , e) EBSD phase map showing zircon (green), aegerine (red), and null EBSD results (black), and f) EBSD band contrast map showing high quality diffraction for zircon and aegerine except in zones of planar features.

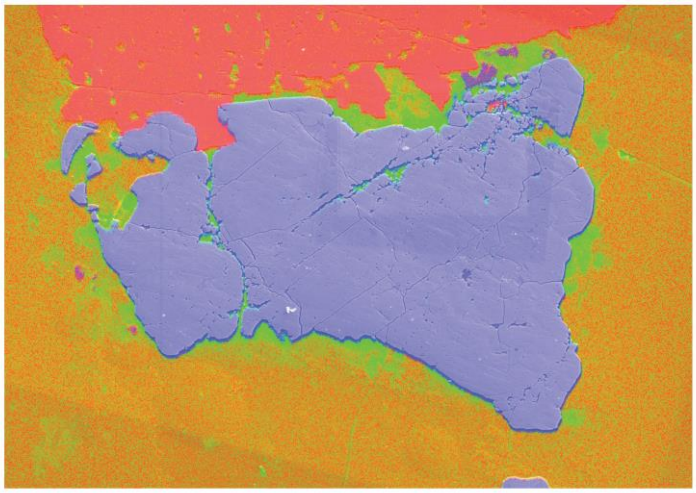

Figure 3-7: V-62 F3340 EDS map showing zircon (purple), aegerine ($NaFeSi_2O_6$) (red), and a Na-Al-Si-O phase (green) around the margins of the zircon and infilling fractures in zircon and aegerine. Orange is also Na-Al-Si-O, but appears to be the mineral constituent contributing to the melted phase (likely plagioclase). There does appear to be a slight difference in the amount of Al between the melt and surrounding mineral.

A second zircon grain, F123, is shown here to represent another IMG inclusion texture. An interesting texture is seen in Figure 3-8, where submicron, ovoid melt inclusions appear along annealed curviplanar features to create outline polygonal domains. These melt inclusions do little to disrupt zonation in CL (Fig. 3-8d). Again, these inclusions match the melt compositions tracing planar features in surrounding acmite (Fig. 3-8a,c). There is a noted absence of twins or planar features in this zircon.

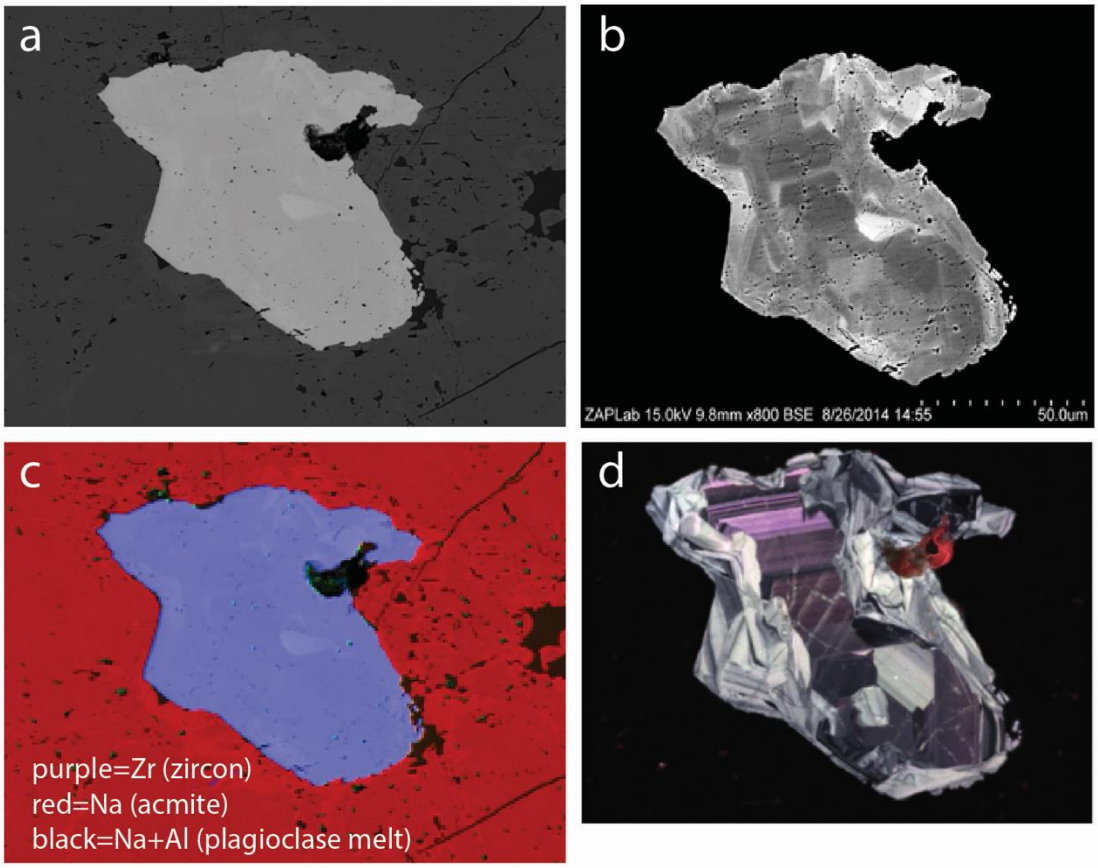

Figure 3-8: Electron beam data for V-62 F123 a) SE image showing similar inclusions and shock features in zircon and surrounding aegerine, b) BSE image showing polygonal melt inclusion domains, c) EDS map with purple=Zr representing zircon, red=Na representing aegerine, and black/dark green=Na+Al, representing plagioclase melt within aegerine and zircon, d) colour CL image. Note planar and curviplanar bright features perhaps relict annealed fractures. They coincide with chains of impact melt glass inclusions.

3.6.2.2.2 Intermediate sample: V2-1 F3655

Sample V2-1 is a charnockitic gneiss (plagioclase + quartz + orthopyroxene (hypersthene) + minor titanomagnetite) collected ~11.4 km from the center of impact. It is located in the gradational contact between middle and upper crustal rocks (ILG and OGG, respectively), in an area affected by Archean charnockitization (alteration by

anhydrous metamorphic fluids) and m-wide impact-generated pseudotachylite veins. Zircon F3655 has a core domain featuring typical igneous concentric zoning (Fig. 3-9c) patterns, surrounded by a brighter discontinuously zoned metamorphic rim. Both zoning patterns are disturbed by shock microstructures many of which host chains of inclusions.

This grain is pervaded by numerous IMG inclusions as well as what was likely once a primary igneous inclusion. The primary feature is a single, roughly rectangular domain in the lower, central part of the grain filled with low density phases (Fig. 3-9b). It fits the criteria for a primary inclusion and its shape is reminiscent of apatite mineral inclusions commonly observed in igneous zircon grains. IMG inclusions in V2-1 are also dark (lower average atomic number (Z)) in BSE images, but instead occur along microtwinned domains, and curviplanar features, varying in morphology. The inclusions found along microtwins are typically either elongate, or small and ovoid (Fig. 3-9). Curviplanar feature-hosted inclusions are either small and ovoid or larger, irregularly shaped pods (Fig. 3-9b). Sometimes, these pods appear to delineate planar features. The average size of elongate inclusions is 3-5 μm's in length and 1-3 μm's in width, while the ovoid inclusions are typically submicron, and the pods found along curviplanar features are ~5-15 μm's in length. EBSD analysis of this grain indicates that inclusions are amorphous (Fig. 3-9d, 3-10c). as well as the primary inclusion domain except for the remnant crystalline FeO that has not been replaced.

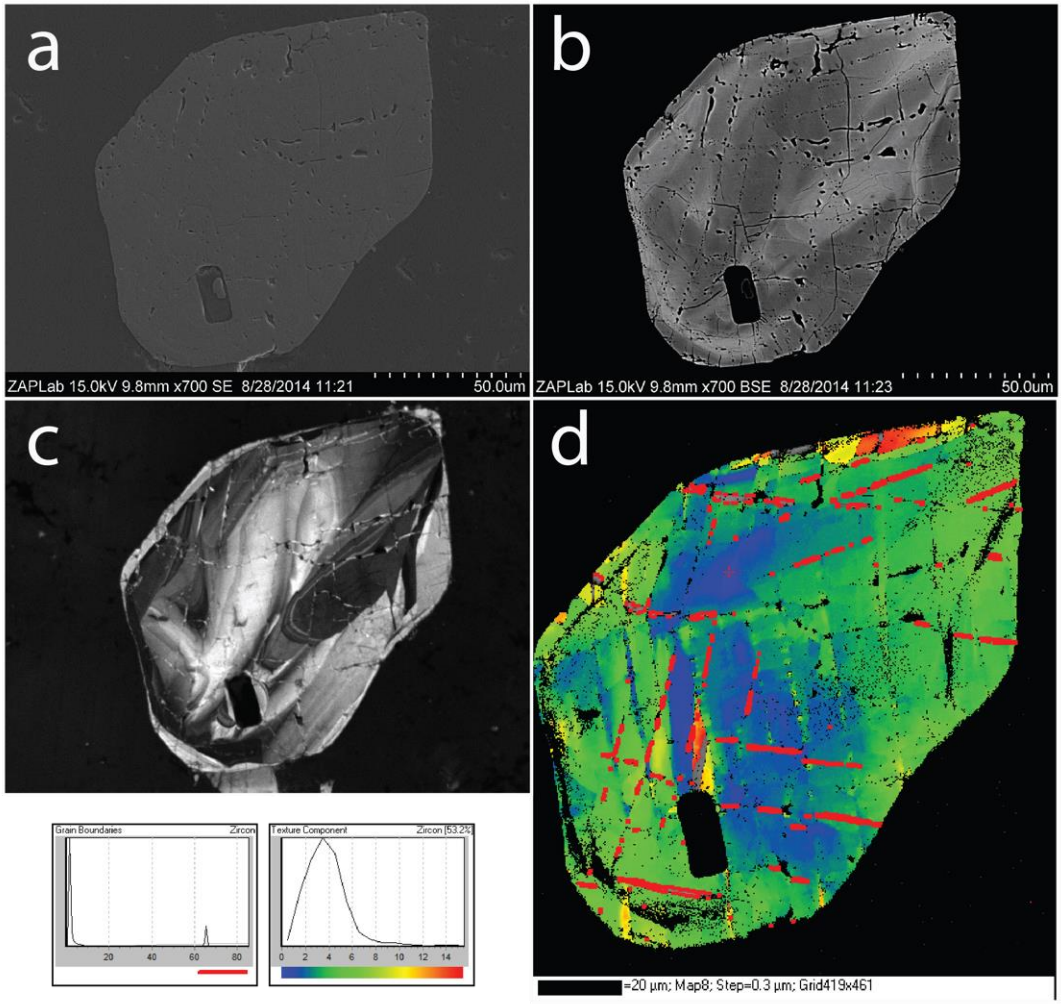

Figure 3-9: Electron beam data for V2-1 F3655 a) SE image, b) BSE image showing low density, c) CL image, showing pre-impact igneous core and metamorphic rim cross-cut by lighter CL traces along features containing inclusions,, d) EBSD misorientation map showing microtwins (red lines), melt inclusions (black), and misorientation across the zircon. Note that some black (non-indexed) domains are high-U metamict domains (also black in CL)

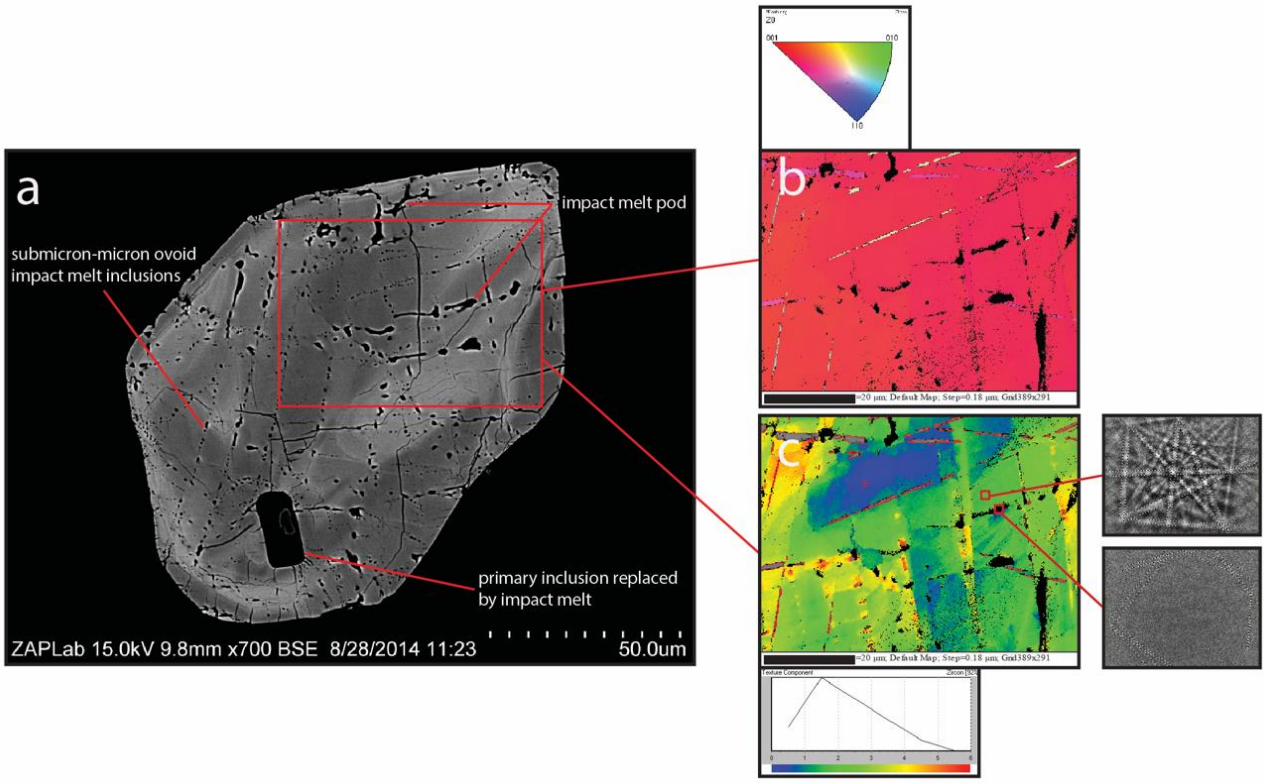

Figure 3-10: Electron beam data for V2-1 F3655 a) BSE image indicating the morphological differences between impact melt pods, abundant submicron-µm sized ovoid IMG inclusions, and primary inclusion variably replaced by impact melt, b) zoom-in EBSD inverse pole figure image showing different crosscutting microtwins (pink and yellow), as well as amorphous inclusions (black), c) EBSD misorientation map showing twins with different sizes, and inclusions (black). EBSP's of high-quality zircon and amorphous inclusions are inset.

EDS mapping and semi-quantitative analysis

Qualitative EDS mapping of the region around V2-1 F3655 indicates that the zircon is hosted primarily within plagioclase, with minor amounts of orthoclase and mafic minerals (orthopyroxene) (Fig. 3-11). Zircon F3655 has one dominant and two minor

melt inclusion compositions. In the central upper region of the grain (Figure 3-11a, b) Mg(+Fe)-rich inclusion compositions are dominant. Such Mg(+Fe) aluminosilicate inclusions are present throughout the grain, and constitute the dominant composition of melt inclusion. K-rich inclusions appear, mainly near the edge of the zircon in Figure 3-11b, in contact with orthoclase at the grain boundary. Na-rich inclusions are very small, and often difficult to resolve in EDS maps. A relatively larger expression of each of these melt compositions (Fe+Mg-rich, K-rich, and Na-rich) is observed replacing the primary inclusion domain in the lower left of the grain (3-11a). Inclusions are relatively homogeneous across strike.

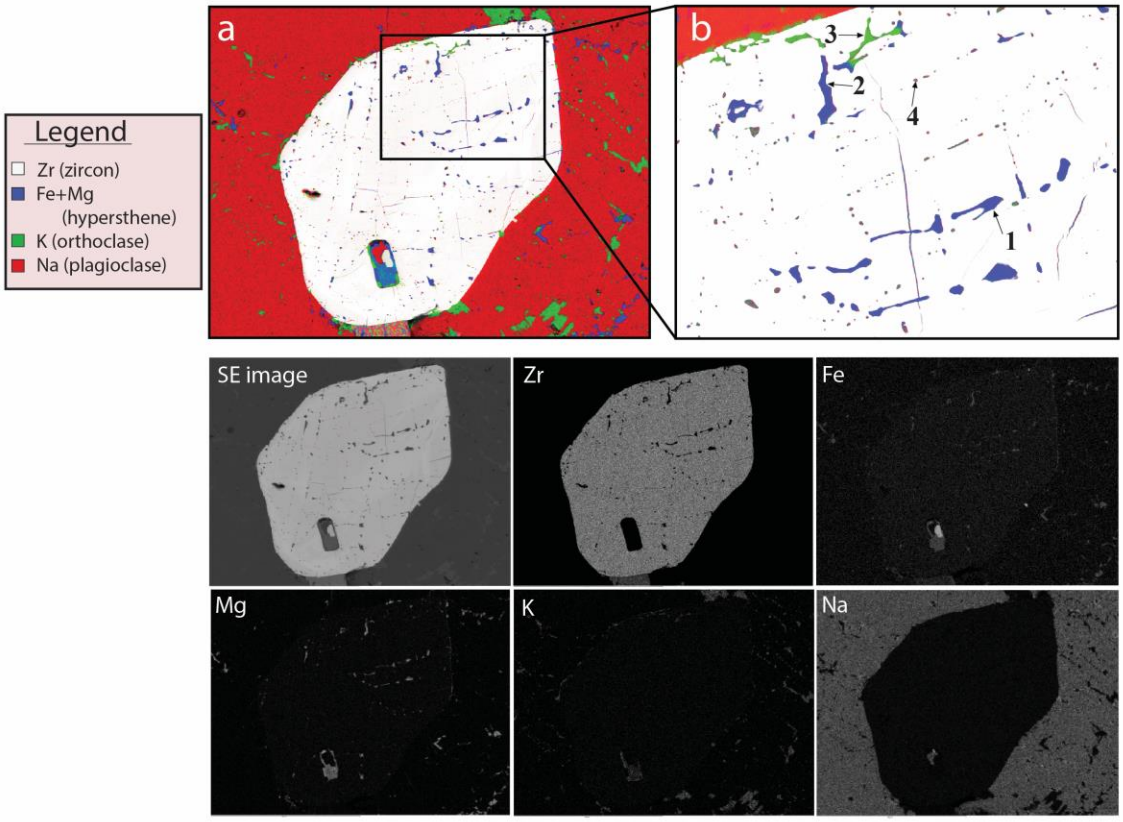

Figure 3-11: EDS mapping of V2-1 zircon F3655 a) EDS map of zircon (white) and matrix minerals, red=Na, green=K, purple=Mg(+Fe) showing melt inclusions

compositions are variable but dominantly Fe and Mg bearing. Associated elemental maps (Zr, O, Mg, K, Na) are shown below. b) inset image showing melt inclusions. Inclusions 1-4, as they relate to Table 3-5, are denoted.

The compositional data for V2-1 IMG inclusions can be grouped into three inclusion types and several large and representative inclusions were targeted for semi-quantitative analysis (Table 3-5). Slight heterogeneity in similiar inclusions was detected as shown by Incl. 1 and 2 (Table 3-5). Inclusions 1 and 2 appear to be similar in composition to hypersthene, a mineral (considered discredited as a formal 'mineral' by the IMA in 1998) which has a significant amount of both Fe and Mg. For the purposes of describing a pyroxene with both Fe and Mg components, and because of the relationship between charnockites and so-called hypersthene, we will continue to use the term hypersthene to describe these non-endmember pyroxenes. The formula for hypersthene is $(Mg,Fe)SiO_3$, and the presence of Al in our analyses may be due to substitution with Si. Inclusion 3 appears to match the stoichiometry of ideal end-member orthoclase ($KAlSi_3O_8$) relatively well. Inclusion 4 appears to match the stoichiometry of an ideal Na-Ca plagioclase such as andesine $(Na,Ca)(Si,Al)_4O_8$.

	Incl. modal%	Na	Mg	Al	Si	K	Fe	Ca	Zr	O	Total
Incl. 1	**90%**	--	10.32 ±0.40	5.41 ±0.28	21.52 ±0.34	--	20.45 ±0.21	--	--	42.3 ±0.38	100
Incl. 2		--	9.91 ±0.21	4.98 ±0.51	21.32 ±0.46	--	22.37 ±0.62	--	--	41.42 ±0.65	100
Incl. 3	**7-8%**	--	--	9.31 ±0.53	31.39 ±0.23	12.66 ±1.13	--	--	--	46.64 ±0.44	100
Incl. 4	**2-3%**	5.32 ±0.20	--	12.12 ±0.64	29.58 ±1.72	--	--	4.75 ±1.77	--	48.23 ±0.71	100

Table 3-5: V2-1 semi-quantitative EDS results of four representative inclusions. Inclusions 1 and 2 are the dominant Mg (+Fe) aluminosilicate inclusion. Incl. 3 is the

less common K aluminosilicate inclusion. Incl. 4 is the composition found along very tiny ovoid inclusions (Na-Ca) aluminosilicate. Standard deviation (2σ) provided.

3.6.2.2.3 Core sample: V09-237 grain 4

V09-237 is a sample of Inlandsee Leucogranofels (ILG) taken from near the Inlandsee Pan, approximately 4 km north of the estimated center of impact (Fig. 3-1). This sample has been prepared as a grain mount of zircons separated from the host rock. Grain 4 is typical of the main zircon population, an elongate, euhedral zircon with primary, concentric oscillatory zonation surrounded by a sector-zoned rim (Moser et al., 2011). BSE and SE images (Figs. 3-12a, 3-13a) show dark ovoid to elongate linear inclusions of IMG inclusions tracing planar and curviplanar features. CL images display a bright response along these inclusion-hosting microstructures (Fig. 3-12b). Inclusions vary in morphology, from elongated inclusions to much smaller, ovoid inclusions. Elongate inclusions are typically between ~20 and 50 μm's in length, and ~1-2 μm's in width. They tend to pinch and swell along strike, and are thus somewhat irregular. The tiny, ovoid inclusions in this grain typically vary between submicron to 3 μm's in diameter, and are also irregular in shape. Inclusions are invariably located along planar and curviplanar features, often in direct association with microtwins. Microtwins appear discontinuous, and are disrupted by these IMG inclusions. They also tend to occur closer to the edges of the zircon. All are amorphous in EBSD whereas zircon diffracts well (Figure 3-13b, c). As seen in the SE image (Fig. 3-13a), there is absolutely no difference in polish quality between zircon and the melt inclusions.

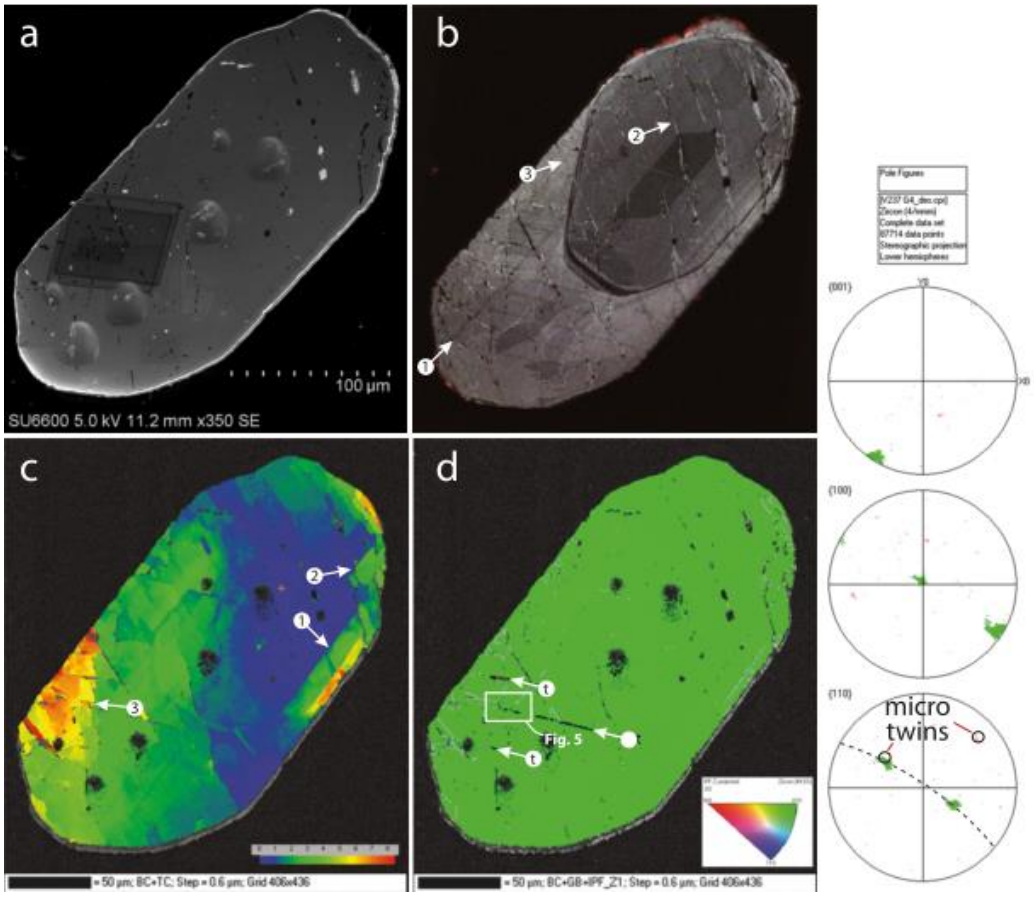

Figure 3-12: Electron beam data for V09-237 grain 4 a) BSE image, b) CL image, c) EBSD misorientation image, d) EBSD inverse pole figure image. Pole figures are shown on the stereonets on the right. Figure from Moser et al. (2011).

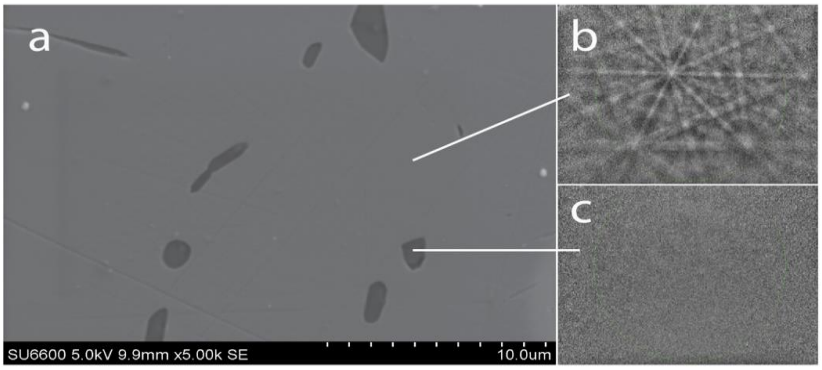

Figure 3-13: Electron beam data for V09-237 grain 4 a) SE image of IMG inclusions tracing annealed curviplanar features within zircon, b) EBSP indicating high-quality zircon pattern, and c) EBSP of an amorphous IMG inclusion.

Energy dispersive spectroscopy (EDS) mapping and semi-quantitative analysis

Grain 4 is an *ex-situ* zircon (grain-mounted), and thus, it is not possible to directly compare IMG inclusion compositions to the immediate surrounding mineralogy. It has been documented (Moser et al., 2011), that this zircon originates from a classic medium-grained Inlandsee Leucogranofels Gneiss (ILG) sample. Stepto (1990) classified this ILG rock based on its mineralogy, predominantly consisting of quartz, orthoclase, and plagioclase.

Grain 4 has two dominant melt inclusion compositions. The two types contain Al, Si and O but differ in the proportions of Na and K. (Fig. 3-14), and these variations are somewhat spatially controlled. The K-rich inclusions are present throughout Grain 4 (Fig. 3-14), however Na-rich inclusions are only present on the right side of the grain. Inclusion compositions often change along strike (Fig. 3-14c), which was not observed in V-62 or V2-1. This compositional change is not gradational, but rather quite distinct (as in Fig. 3-14c Incl. 3). Despite the spatial variance in general inclusion composition, there does not appear to be a preference for either composition to occupy only one particular type or orientation of shock microstructure.

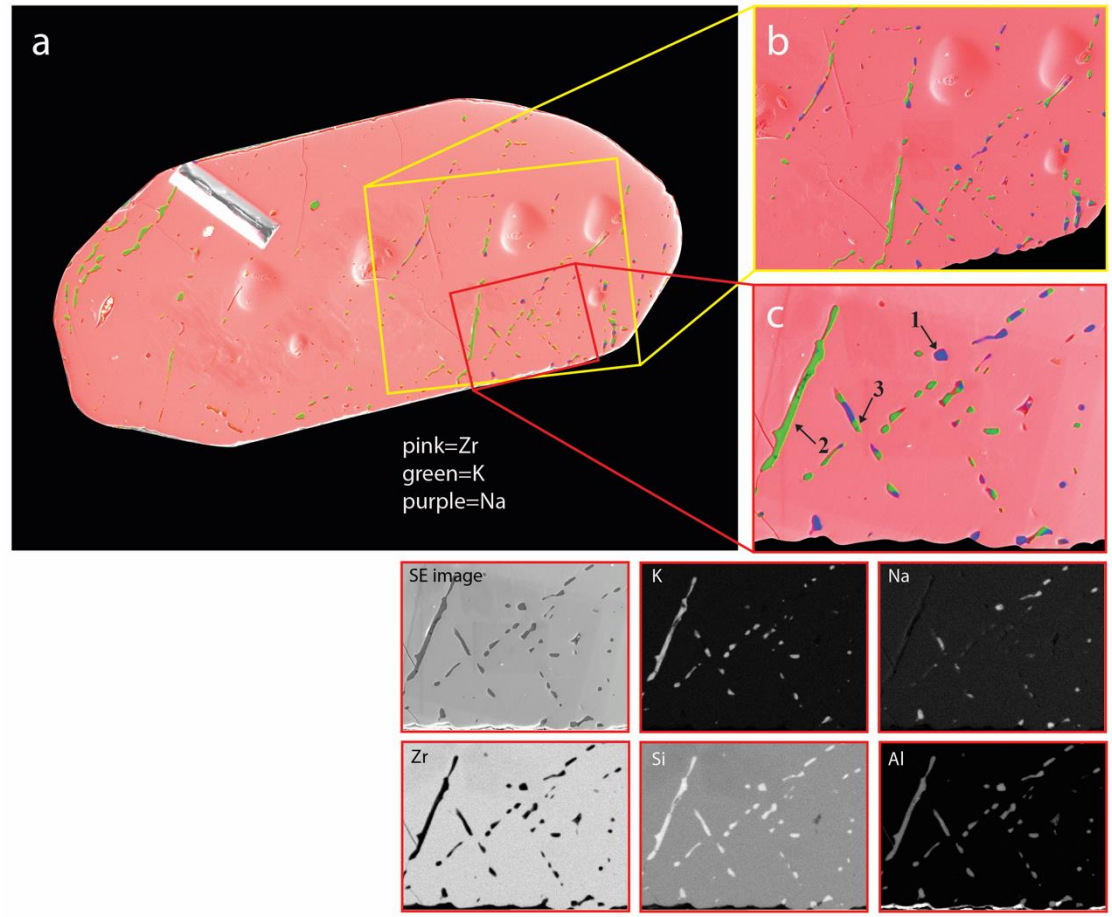

Figure 3-14: EDS map of V09-237 Grain 4 a) full-scale map of zircon, showing melt inclusions of various compositions, b) inset image showing melt inclusions in the lower right portion of the grain, c) zoomed-in inset image showing how melt inclusions change composition along strike. Inclusions, as they relate to Table 3-6, are denoted. Pink=Zr, green=K, purple=Na.

Semi-quantitative EDS analyses of three representative IMG inclusions were made within one domain of the zircon (Figure 3-14c) and results are listed in Table 3-6. Both the K and Na IMG inclusion types (inclusions 1 and 2) appear to match with the stoichiometry of minerals from the rock (albite and orthoclase) given by Moser et al. (2011). Inclusion 1 is very similar in elemental abundance to the stoichiometry of ideal end-member albite,

$NaAlSi_3O_8$. Inclusion 2 is similar in elemental abundance to the stoichiometry of $KAlSi_3O_8$. There are no mafic inclusions in this zircon. Inclusion 3 was known from mapping to have a bimodal alkali composition along strike (Fig. 3-14c). The semi-quantitative results are also mixed and could be due to impingement of the activation volume of the beam on an interface between the Na and K-rick IMG domains, or could indicate that contacts are more gradational than they appear on the elemental maps.

	Incl. modal %	Na	Mg	Al	Si	K	Fe	Ca	Zr	O	Total
Incl. 1	**~15%**	8.05 ±0.62	--	10.14 ±0.35	32.50 ±0.52	--	--	--	--	49.09 ±0.24	100
Incl. 2	**~85%**	--	--	9.18 ±0.57	31.80 ±0.03	11.79 ±0.15	--	--	--	46.95 ±0.25	100
Incl. 3	**--**	2.53 ±0.40	--	9.71 ±0.26	33.60 ±0.64	5.28 ±0.83	--	--	--	48.88 ±0.36	100

Table 3-6: V09-237 semi-quantitative EDS results of three representative inclusions. Incl. 1 is the Na-rich inclusion, incl. 2 is the K-rich inclusion, and incl. 3 is a mixed component with both Na and K, likely due to beam impingement on multiple inclusion compositions. Inclusions are denoted in Figure 3-13c. Estimated inclusion composition abundances are listed. Standard deviations are given at 2σ.

3.6.2.3 Chronology of impact melt glass inclusion injection

IMG inclusions are only found in grains with curviplanar features. This relationship is evident in Figure 3-5, where an almost perfect statistical correspondence is observed. In many cases, melt inclusions are also found along planar fractures and microtwins. Microtwins, generally thought to be later planar fracturing during rarefaction, terminate against melt inclusions (Fig. 3-10c). There is, however, a spatial relationship between twins and melt inclusions, and therefore the two are thought to be relatively

contemporaneous. Twins are often deformed (Fig. 3-6d), providing evidence for later-stage crystal plastic deformation related to crater modification. Post-shock recrystallization (Fig. 3-3d) destroys all shock microstructures, and is therefore post-melt inclusion injection. Based upon cross-cutting relationships in this study, it appears that IMG inclusions are incorporated into the zircon post-planar fracturing, microtwinning, and curviplanar features, but pre-post-shock recrystallization. This recrystallization is sometimes locally due to the heat related to impact melting, but typically occurs during a period of immense regional heating commencing immediately post-impact.

3.7 Discussion

3.7.1 Nature of IMG inclusions across the Vredefort central uplift

A comparison of the nature and distribution of IMG inclusions in the three samples across the ~23 km range of occurrence reveals many broad similarities and differences. IMG inclusions are always associated with shock microstructures, dominantly curviplanar features, but also planar features (filled fractures and microtwins) (Fig. 3-5). There is, occasionally, a greater abundance of melt inclusions near grain margins as opposed to the centre of the zircon. This observation is likely linked to the placement of the melt inclusions' local source mineral. EBSD successfully verified that all inclusions analyzed were amorphous at the 60 nm average length scale, similar to original reports (Moser et al., 2011). This reinforces the interpretation that all of these inclusions are, in fact, glass. The walls of host zircon surrounding IMG inclusions often show signs of a chemical change, as displayed by the change (typically increase) in CL emission (Fig. 3-9c, 3-12b). IMG inclusions are heterogeneous with regard to their major element chemistry, with three main compositional types identified throughout the crater. These

compositions are similar to that of host minerals in the respective sample, and are variable between different rock types. The main differences that exist in inclusions from across the transect are in respect to size. The sample furthest from the centre of impact typically has the smallest (submicron) IMG inclusions. Those inclusions from the closest to the centre of impact often extend to over tens of nm's. The variance in inclusion size likely points to the respective degree of melting at various points throughout the crater. These common characteristics allow us to comment on the sources of the IMG inclusions, and the mechanisms for their entrainment in zircon and preservation for over two billion years.

3.7.2 Source of IMG inclusions

The Vredefort structure hosts several types of impact melt bodies such as gabbronorite intrusions (Cupelli et al., 2014) and 2.02 Ga bronzite granophyre dykes with a crustal and meteoritic composition that have been introduced into the crater floor environment during cratering (Koeberl et al., 1996). At the microscopic scale, evidence of localized partial melting (Kamo et al., 1996; Stepto, 1990; Gibson & Reimold, 2005) has been recognized as the cm-scale glomerogranular quartz aggregates and granophyric texture (Kamo et al., 1996) in the Inlandsee Leucogranofels unit (V09-237) near the center of impact. A macroscale expression of this partial melting is the nearby central anatectic granite (2017 ± 5 Ma (Gibson et al., 1997)) (Moser et al., 2011; Cupelli et al., 2014), so despite the *ex-situ* nature of this zircon, we can establish a potential source mechanism for the IMG inclusions. There is no evidence that the IMG inclusions are derived from local primary inclusions, as evacuation of primary inclusions and re-distribution along shock features

would leave cavities or large crystal-shape pores in the zircon. This scenario is not observed in these samples.

Qualitatively, inclusion compositions in V09-237 were comparable to orthoclase and albite; two dominant feldspars existing in this rock before grain separation (Moser et al., 2011). The qualitative characteristics of the IMG inclusions in zircon in the two *in-situ* samples (V2-1 & V-62) likewise indicate a local source of melt generation. In collar sample V-62, Na-rich aluminosilicate glass at the margins of the zircon can be seen leading into and filling shock related fracture zones that lead into trails of IMG inclusions. In sample V2-1, the mineralogical compliment to the K-rich IMG inclusions can also be seen at the margin of the grain. Mafic inclusions of hypersthene and plagioclase composition appear to qualitatively match hypersthene and plagioclase minerals sparsely found outside of the zircon as well. It should be noted that no zircon analyzed in this study had any melt inclusions that could not be associated to local mineralogy, often within the field of view used for EDS mapping. This places a relative bound on the distance these melts travel before incorporation into the zircon.

The variable composition of the IMG inclusions between samples also argues for a local source. The observation that V09-237 does not have any mafic melt inclusions indicates that the major control on melt inclusion types is not necessarily P/T conditions, but rather local mineralogy. Semi-quantitative EDS is not possible for most V-62 zircons, however EDS maps indicate that the melt composition consists only of Na, Al, Si, and O, which likely originates from nearby plagioclase grains. In V2-1, the compositions match relatively well with mineral standards of orthoclase ($KAlSi_3O_8$), plagioclase ($NaAlSi_3O_8$-$CaAl_2Si_2O_8$), and hypersthene ($(Mg,Fe)SiO_3$), with estimated abundances of ~7-8%, 2-

3%, and 90%, respectively (Table 3-7). Interestingly, in the case of V09-237, inclusion compositions match well (within ~1 wt. % per element) with mineral standards of plagioclase (albite) ($NaAlSi_3O_8$) and orthoclase ($KAlSi_3O_8$), with estimated abundances of ~15% and 85%, respectively (Table 3-8).

V2-1						
Wt. %	**Incl. 1**	**Hypersthene USNM 746**	**Incl. 3**	**Orthoclase SPI**	**Incl. 4**	**Plagioclase SPI**
Na	--		--	0.35	5.32 ± 0.20	3.23
Mg	10.32 ± 0.40	16.16	--	--	--	--
Al	5.41 ± 0.28	0.65	9.31 ± 0.53	8.93	12.12 ± 0.64	15.10
Si	21.52 ± 0.34	25.28	31.39 ± 0.23	30.23	29.58 ± 1.72	25.34
K	--		12.66 ± 1.13	13.25	--	0.34
Fe	20.45 ± 0.21	15.22	--	1.39	--	--
Ca	--	1.08	--	--	4.75 ± 1.77	8.43
Zr	--		--	--		--
O	42.3 ± 0.38	44.00	46.64 ± 0.44	45.84	48.23 ± 0.71	47.08

Table 3-7: V2-1 comparisons of impact melt glass inclusions vs. ideal source mineral. Mineral wt. %'s are taken from standard minerals (SPI supplies, Smithsonian Microbeam Standards). Hypersthene differences are likely due to Al-Si and Fe-Mg substitution. Slight plagioclase differences are due to solid solution between Na-Ca. Analyses errors given at 2 σ.

V09-237				
Wt. %	**Incl. 1**	**Albite SPI**	**Incl. 2**	**Orthoclase SPI**
Na	8.05 ± 0.62	8.50	--	0.35
Mg		--	--	--
Al	10.14 ± 0.35	10.46	9.18 ± 0.57	8.93
Si	32.50 ± 0.52	31.85	31.80 ± 0.03	30.23
K	--	0.20	11.79 ± 0.15	13.25
Fe	--	--	--	1.39
Ca	--	0.30	--	--
Zr	--	--	--	--
O	49.09 ± 0.24	48.70	46.95 ± 0.25	45.84

Table 3-8: V09-237 comparison of impact melt glass inclusions vs. ideal source mineral. Mineral wt. %'s are from standard minerals (SPI supplies). Analyses errors given at 2 σ.

Fig. 3-15 shows the melt inclusion compositions from V2-1 and V09-237 on ternary (Al-K-Na) diagrams. A local source for IMG inclusions is also likely given that their compositions, in aggregate, can be closely matched with compositions of the host rock. Fig. 3-15 shows the melt inclusion compositions from V2-1 and V09-237 on ternary (Al-K-Na) diagrams. Figure 3-16 plots the inclusion compositions on total alkali vs. silica (TAS) diagram. Partial melt inclusions from V2-1 and V09-237 closely match the composition of the igneous rock type from which they originated. For example, a triangle between the three major inclusion types of V2-1 encompasses the approximate bulk composition of V2-1. This bulk composition was estimated by phase mapping, optical petrography, and references to the literature of charnockitic rocks at Vredefort (Flowers

et al., 2003; Lana et al., 2003) which describe the central Vredefort charnockites as being quartz monzodioritic to dioritic in composition. Inclusions from V09-237 plot as a line (binary) which is similar, but not identical, to the silica-rich granite composition of the ILG.

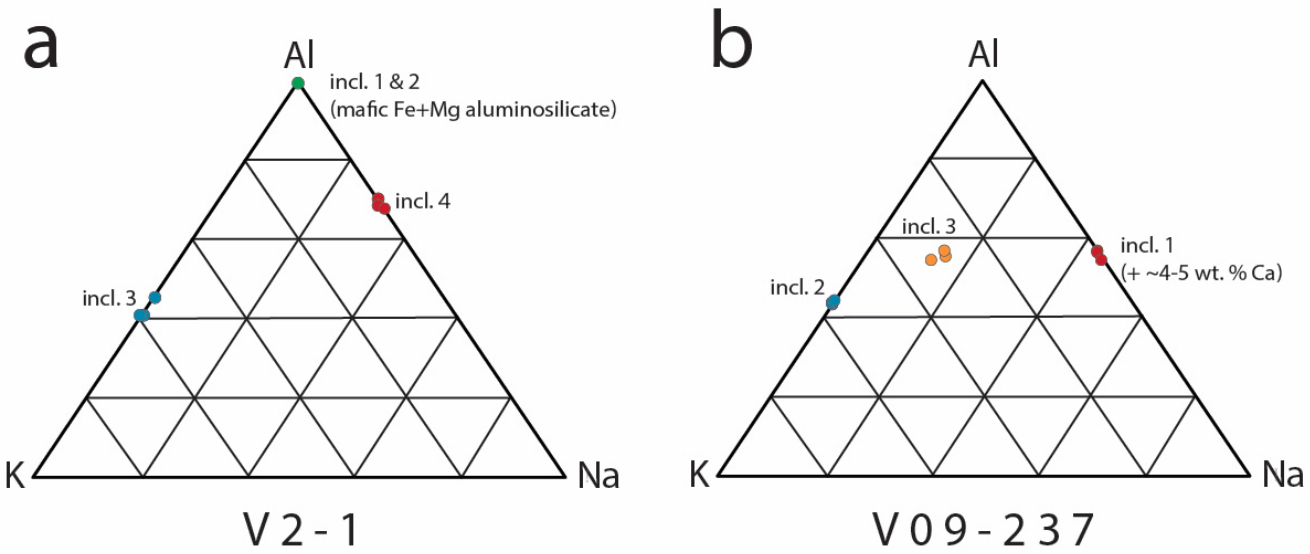

Figure 3-15: a) ternary diagram of V2-1 melt inclusion compositions, and b) ternary diagram of V09-237 melt inclusion compositions. Ternary diagrams created with Trinity software.

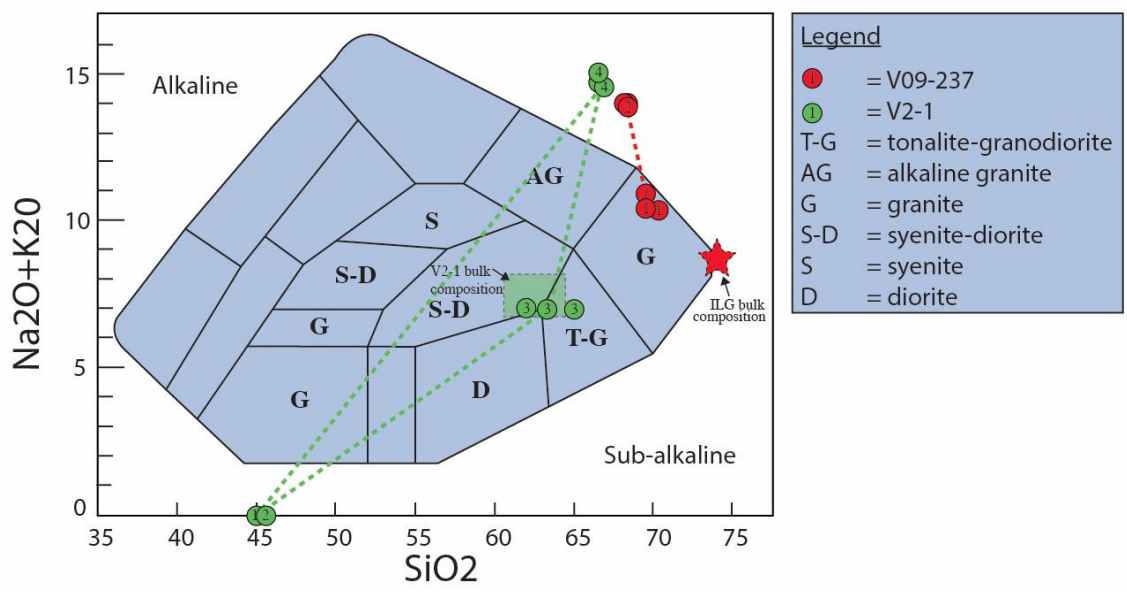

Figure 3-16: Total alkali vs. silica (TAS) diagram adapted from Cox et al. (1979); Pompa-Mera et al. (2013). This diagram plots the various inclusion compositions found in V2-1 (green) and V09-237 (red) on plutonic classification diagram. Na-rich inclusions fall on diagram, but K-rich inclusions in both V2-1 and V09-237 fall on the "alkaline" chart. Mafic inclusions from V2-1 are found at the bottom of the chart due to lack of alkalis. Estimated bulk compositions of V2-1 and V09-237 are shown.

3.7.3 IMG inclusion formation and preservation mechanisms

3.7.3.1 Conditions of melting

The IMG inclusions are products of impact melting, which occurs during decompression after the passage of a shockwave (Grieve et al., 1977). Our observations can be used to place brackets on the temperatures necessary for IMG inclusion formation. The upper bracket is the melting temperature of zircon itself at 1676°C. There is no evidence of zirconium in the IMG inclusions or textural evidence for zircon melting in these samples so this temperature is taken as the ceiling for the IMG inclusion forming processes. The

lower bracket would be the melting temperature of the lowest T_m mineral (typically albite T_m=~1100°C). The absence of impact melt inclusions in zircons at V15-55 could be due to the fact that they are hosted in a quartzite (quartz T_m= ~1700°C) and the lack of local lower-melting temperature minerals (i.e. albite T_m=~1100°C, anorthite T_m=~1500°C, orthoclase T_m=~1200°C). It is also situated at a radial distance outside of the zone of pressure sufficient to cause melting/curviplanar feature/microtwin formation (Chapter 2) and high post-impact temperatures (Ivanov, 2005). Given the occurrence of coesite in the same outcrop (Martini, 1978) we can establish a minimum pressure for IMG inclusion formation in zircon at ~3 GPa.

The presence of both mafic and felsic inclusions within V2-1 F3655 indicates exposure to a wide range of shock conditions perhaps up to the melting temperature of pyroxene (T_m=~1400°C). An average temperature of IMG inclusion formation in the range ~1100°C to 1700°C (i.e. below the melting temperature of quartz), would account for the fact that, in the ILG sample, inclusion population does not match the composition of the bulk rock and is relatively quartz-poor.

Assuming our model is correct, the composition of zircon IMG inclusions has the potential to serve as a proxy for the maximum temperature (and inferred pressure) experienced by its host rock, as well as fingerprinting the host rock lithology. This would be of value for zircons, for instance, that have been removed from their host rock by erosion and/or impact-driven transport (e.g. lunar regolith breccia).

3.7.3.2 Timing of injection

Based upon the cross-cutting relationships established in this study, it appears that impact melt inclusions are incorporated into the zircon after planar features, microtwinning, and

curviplanar features, and before high-temperature post-shock recrystallization. The inclusions of shock melt seen in V-62 F123 may actually play a significant role in nucleating the recrystallization of domains that date the impact event. Annealed curviplanar features hosting IMG inclusions in V-62 F123 appear to outline polygonal zones that may be a precursor to defect-nucleated crystallization seen in other zircons. We conclude that, just as twins have been shown to act as nucleation sites for recrystallization (Timms et al., 2014), as should IMG inclusions. Further description and a schematic displaying these microstructural relationships is available in Chapter 2.

We suggest, based on the strong spatial and statistical (Fig. 3-5) association, that the timing of IMG inclusion intrusion is intimately related to the formation of the curviplanar features. The curviplanar family of microstructures has only recently been recognized in the literature, and appears to be unique to the crater-basement environment. Given the large displacements that take place on a subset of curviplanar features that offset the grain margin, it is again likely that minerals were locally impact-melted and introduced into the host zircon, as in V-62. This type of strain in the rock, as a whole, does not fit with very short-lived high pressure shock wave. It does, however, match the behaviour expected by the post-impact rebound of the crater floor through a vertical process of 10 km, and/or the continued motions of the crater floor during longer-term isostatic rebound of the impact-traumatized crust. It has been suggested that rarefaction and decompression could cause movement and negative pressures in zircon grains to offer a primary pathway for the impact melt into the zircon (Moser et al., 2011), which also sets a temporal constraint for the development of this melting. The absence of melt inclusions in zircons that do not exhibit shock microstructures related to rarefaction or unloading (i.e. curviplanar

features, microtwins), as in V15-55 (Fig. 3-3) is further evidence that compression (planar fracturing) alone does not introduce melt into the zircon.

The relationship between planar and curviplanar features and IMG inclusions highlights the rate at which these structures are formed, as planar fractures must have remained open long enough to be penetrated by melt introduced along the later curviplanar features. In Chapter 2, we documented curviplanar features crosscutting microtwins, which is contrastable with the findings of Moser et al (2011). Melting, injection into open fractures, and the formation of these other microstructures must happen very rapidly (ms^{-1}), based on the microstructural relationships observed. The bright response in CL and annealing of these microstructures implies that melt remained hot for long enough to allow for trace element exchange with the host zircon, although this trace element diffusion and exchange may have been quite rapid if accelerated by high defect densities along the curviplanar feature margins.

Different compositions also sometimes occur along certain microstructures (as in Fig. 3-11), implying that there is a mechanical or morphological constraint on the composition of impact melt preserved. This may imply that certain minerals melted first and were incorporated along a specific microstructure, whereas later melts were incorporated along later-formed microstructures. This scenario may have been followed by a stage of mixing followed by segregation as we found no strong association of a certain orientation or type of microstructure with a particular IMG inclusion composition. Another process, perhaps operating in parallel, is the possibility of large immiscibility differences between different glass compositions as they intruded the zircon and expanded and cooled at different rates

based on density and composition. Answering these questions will require additional detailed study.

3.7.3.3 Glass formation and preservation

All IMG inclusions analyzed in this study appear amorphous (glass) under the ~60 nm EBSD resolution limit. All possible precautions were taken to ensure IMG inclusions were not preferentially polished, and as shown in Fig. 3-13, the melt inclusions have an equal polish quality to the surrounding zircon. This indicates that the amorphous nature of inclusions in EBSD is, in fact, due to a lack of long-range crystallographic order rather than poor polish quality. Additionally, the primary inclusion replaced by impact melt (Fig. 3-11a) retains a portion of the primary magnetite (FeO) crystal which does return an EBSP pattern.

Crystalline melt inclusions and glass melt inclusions in zircon are differentiated as a function of their cooling rate, size, and composition (Roedder, 1979). It can thus be expected that the Vredefort melt inclusions would be glass, as an impact setting is comparable to a volcanic setting in terms of cooling rate. Zircons from volcanic settings are known to host melt glass inclusions in rocks 74 ka and 56 Ma (Thomas et al., 2003). The presence of glass inclusions in this study, and their preservation as glass over the last ~2.020 Ga, is surprising. It is suggested that the zircon structure may retard or diminish the effects of devitrification, which is supported by the presence of glass inclusions in zircons as old as 56 Ma (Thomas et al., 2003) and ejecta zircons from a lunar soil sample >4 Ga (Crow, 2015). The presence of Na in many of these inclusions is also known to inhibit the acts of devitrification in glasses (Snyder, 2012). The lack of zircon incorporation into the inclusion composition is further evidence for quick cooling

(Thomas et al., 2003). The overwhelming presence of glass inclusions in this study as opposed to crystalline inclusions could be related to the small (submicron to μm) size of most inclusions. Thomas et al. (2003) found that small, primary MI tend to remain glass while the larger MI in the same zircon often crystallized. The existence of these features 2 billion years after impact in an upper crustal environment is intriguing and suggests a glass-stabilization mechanism that could be quite applicable to materials science applications if further understood and developed.

3.8 Conclusions

Our microstructural relationship findings are mostly similar to those of Moser et al. (2011), with a few minor exceptions:

i. Curviplanar features appear to crosscut microtwins. We suggest that curviplanar feature formation alone may be the driving force for melt injection, creating the negative pressure that Moser et al. (2011) attributed to microtwins. We recognize that curviplanar feature and microtwin formation are relatively coeval, which may be a contributing factor to this microstructural confusion.

ii. There is a second set of planar features (appearing as ‘microcleavage’) that appear to crosscut twins and earlier planar fractures. These features do not appear to host melt inclusions as they do not appear as open fractures.

In many of the zircons analyzed, there were multiple melt inclusion compositions. The partial melting of various minerals implies multiple generations of impact melt injection occurring in rapid succession. Because of the rate of these ‘pulses’ of melting and injection, it is difficult to illustrate the relative timing of different mineral melting phases.

However, there is potential to fit minerals into a temporal schematic based on their relative melting temperatures.

We suggested a multi-step process for the preparation and analysis of impact melt inclusions in zircon. This process included a new polishing and carbon coat method. We also identified the best parameters for the energy dispersive spectroscopy (EDS) mapping and semi-quantitative EDS analysis of melt inclusions. These settings were chosen so as to diminish the contribution of surrounding zircon into the composition measurements and limit alkali mobility. It is difficult, and sometimes impossible, to get accurate EDS analyses of particularly small (<submicron) melt inclusions. We concede that this problem is not exclusive or inherent to EDS, and would impact the results of EPMA or other compositional analyses as well.

Between 80-100% of the zircons not affected by post-shock recrystallization have IMG inclusions (Fig. 3-5). This prevalence means that IMG inclusions may represent the most abundant shock microstructure (along with curviplanar features) in zircon from the Vredefort impact structure. This also indicates that the majority of zircons from a deep-crater granitoid environment will host impact melt inclusions, providing incredible and substantial exploration potential.

The preservation of these glass inclusions in zircon from a ~2.020 Ga impact crater has far-reaching implications for the discovery of ancient impact events that lack surficial expression. The variation in melt inclusion compositions, and ability to relate these compositions with the stoichiometry of local rock-forming minerals, has implications for the association of *ex-situ* lunar zircons to their host terranes. The analysis of plagioclase-rich charnockitic gneiss samples (i.e. V2-1) provide a valuable link to similarly

plagioclase-rich lunar samples, highlighting the value of terrestrial analogue sites. Shock conditions experienced by zircons which host impact melt inclusions may be reconcilable based on the melting conditions of incorporated mineral melts. With further study and advancements, these results will hopefully help resolve the mechanisms underlying the dichotomy between reset and non-reset U-Pb ages of zircon, and ultimately improve the accuracy of bombardment chronologies.

3.9 References

Bohor, B. F., Betterton, W. J., & Krogh, T. E., 1993. Impact-shocked zircons: discovery of shock-induced textures reflecting increasing degrees of shock metamorphism. *Earth and Planetary Science Letters, 119*(3), 419-424.

Cavosie, A. J., Quintero, R. R., Radovan, H. A., & Moser, D. E., 2010. A record of ancient cataclysm in modern sand: Shock microstructures in detrital minerals from the Vaal River, Vredefort Dome, South Africa. *Geological Society of America Bulletin, 122*(11-12), 1968-1980.

Cavosie, A. J., Erickson, T. M., & Timms, N. E., 2015. Nanoscale records of ancient shock deformation: Reidite (ZrSiO4) in sandstone at the Ordovician Rock Elm impact crater. *Geology, 43*(4), 315-318.

Cox, K.G., Bell, J.D., & Pankhurst, R.J., 1979. The Interpretation of Igneous Rocks: London, George Allen and Uwin, 450 pp.

Crow, C. A., 2015. The early lunar magmatic and impact histories recorded by Apollo zircons: University of California Los Angeles-Ph.D Thesis.

Crow, C.A., et al., 2016. Geochimica et Cosmochimica Acta (in press).

Cupelli, C.L., Moser, D.E., Barker, I.R., Darling, J.R., Bowman, J.R., & Dhuime, B., 2014. Discovery of mafic impact melt in the center of the Vredefort dome: archetype for continental residua of early Earth cratering? *Geology, 42*(5), 403-406.

Dence, M.R., 1971. Impact melts. *Journal of Geophysical Research, 76*(23), 5552-5565.

El Goresy, A., Gillet, P., Miyahara, M., Ohtani, E., Ozawa, S., Beck, P., & Montagnac, G., 2013. Shock-induced deformation of Shergottites: Shock-pressures and perturbations of magmatic ages on Mars. *Geochimica et Cosmochimica Acta*, *101*, 233-262.

Erickson, T. M., Cavosie, A. J., Moser, D. E., Barker, I. R., & Radovan, H. A., 2013. Correlating planar microstructures in shocked zircon from the Vredefort Dome at multiple scales: Crystallographic modeling, external and internal imaging, and EBSD structural analysis. *American Mineralogist*, *98*(1), 53-65.

Erickson, T. M., Pearce, M. A., Taylor, R. J. M., Timms, N. E., Clark, C., Reddy, S. M., & Buick, I. S., 2015. Deformed monazite yields high-temperature tectonic ages. *Geology, 43*(5), 383-386.

Flowers, R.M., Moser, D.E., and Hart, R.J., 2003. Evolution of the amphibolite-granulite facies transition exposed by the Vredefort Impact Structure, Kaapvaal Craton, South Africa. *Journal of Geology, 111,* 455-470.

French, B.M., 1998. Traces of catastrophe: A handbook of shock-metamorphic effects in terrestrial meteorite impact structures.

Gibson, R. L., Armstrong, R. A., & Reimold, W. U., 1997. The age and thermal evolution of the Vredefort impact structure: A single-grain U-Pb zircon study. *Geochimica et Cosmochimica Acta*, *61*(7), 1531-1540.

Gibson, R. L., & Reimold, W. U., 2005. Shock pressure distribution in the Vredefort impact structure, South Africa. *Geological Society of America Special Papers*, *384*, 329-349.

Gibson, R. L., & Reimold, W. U., 2008. Geology of the Vredefort impact structure: A guide to sites of interest (Vol. 97). Council for Geoscience.

Gibson, R. L., Reimold, W. U., & Stevens, G., 1998. Thermal-metamorphic signature of an impact event in the Vredefort dome, South Africa. *Geology, 26*(9), 787-790. Grieve, R. A., Dence, M. R., & Robertson, P. B., 1977. Cratering processes-As interpreted frothe occurrence of impact melts. In Impact and Explosion Cratering: Planetary and Terrestrial Implications (pp. 791-814).

Grieve, R.A., & Cintala, M.J., 1992. An analysis of differential impact melt-crater scaling and implications for the terrestrial impact record. *Meteoritics, 27*(5), 526-538.

Grieve, R.A., Dence, M.R., & Robertson, P.B., 1977. Cratering processes-As interpreted from the occurrence of impact melts. In *Impact and explosion cratering: Planetary and terrestrial implications* (pp. 791-814).

Hart, R. J., Welke, H. J., & Nicolaysen, L. O., 1981. Geochronology of the deep profile through Archean basement at Vredefort, with implications for early crustal evolution. *Journal of Geophysical Research: Solid Earth, 86*(B11), 10663-10680.

Hart, R. J., Andreoli, M. A. G., Reimold, W. U., & Tredoux, M., 1991. Aspects of the dynamic and thermal metamorphic history of the Vredefort cryptoexplosion structure: implications for its origin. *Tectonophysics, 192*(3-4), 313-331.

Jarosewich, E., 2002. Smithsonian microbeam standards. *Journal of Research of the National Institute of Standards and Technology, 107*(6), 681-685.

Kamo, S. L., Reimold, W. U., Krogh, T. E., & Colliston, W. P., 1996. A 2.023 Ga age for the Vredefort impact event and a first report of shock metamorphosed zircons in pseudotachylitic breccias and granophyre. *Earth and Planetary Science Letters, 144*(3), 369-387.

Kerrick, D. M., Eminhizer, L. B., & Villaume, J. F., 1973. The Role of Carbon Film Thickness in Electron Microprobe Analysis. *American Mineralogist, 58*, 920-925.

Koeberl, C., Poag, C. W., Reimold, W. U., & Brandt, D., 1996. Impact origin of the Chesapeake Bay structure and the source of the North American tektites. *Science, 271*(5253), 1263.

Koeberl, C., 2006. Impact processes on the early Earth. *Elements, 2*(4), 211-216.

Lana, C., & Gibson, R.L., 2003. Geology and geochemistry of a granite-greenstone association in the southeastern Vredefort dome, South Africa. *South African Journal of Geology, 106*, 291-314.

Lana, C., Reimold, W. U., Gibson, R. L., Koeberl, C., & Siegesmund, S., 2004. Nature of the Archean midcrust in the core of the Vredefort Dome, central Kaapvaal Craton, South Africa. *Geochimica et Cosmochimica Acta, 68*(3), 623-642.

Moser, D. E., Cupelli, C. L., Barker, I. R., Flowers, R. M., Bowman, J. R., Wooden, J., & Hart, J. R., 2011. New zircon shock phenomena and their use for dating and

reconstruction of large impact structures revealed by electron nanobeam (EBSD, CL, EDS) and isotopic U-Pb and (U-Th)/He analysis of the Vredefort dome. *Canadian Journal of Earth Sciences, 48*(2), 117-139.

Moser, D. E., 1997. Dating the shock wave and thermal imprint of the giant Vredefort impact, South Africa. *Geology, 25*(1), 7-10.

Nash, W.P., 1992. Analysis of oxygen with the electron microprobe: Applications to hydrated glass and minerals. *American Mineralogist, 77*, 453-457.

Pompa-Mera, V., Schaaf, P., Hernández-Treviño, T., Weber, B., Solís-Pichardo, G., Villanueva-Lascurain, D., & Layer, P., 2013. Geología, geocronología y geoquímica de la Isla María Madre, Nayarit, México. *Revista mexicana de ciencias geológicas, 30*(1), 1-23.

Roedder, E., 1979. Silicate liquid immiscibility in magmas. The Evolution of the Igneous Rocks Fiftieth Anniversary Perspectives, 15-59.

Singleton, A.C. & Osinski, G.R., 2015. Microscopic effects of shock metamorphism in zircons from the Haughton impact structure, Canada. *The Geological Society of America, Special Paper 518*, 135-148.

Snyder, R. L. (Ed.). (2012). Advances in materials characterization II (Vol. 19). *Springer Science & Business Media.*

Spray, J., & Hines, J., 2009. Earth impact database. Planetary and Space Sci. Centre. University of New Brunswick. Canada.

Spray, J.G., Rae, D.A., 1995. Quantitative electron-microprobe analysis of alkali silicate glasses: a review and user guide. *Canadian Mineralogist, 33*(2), 323-332.

Stepto, D., 1979. A geological and geophysical study of the central portion of the Vredefort Dome Structure. University of the Witwatersrand-Ph.D. thesis.

Stepto, D., 1990. The geology and gravity field in the central core of the Vredefort Structure. *Tectonophysics, 171*(1), 75-103.

Stoffler, D., Keil, K., Scott, E.R.D., 1991. Shock metamorphism of ordinary chondrites. *Geochimica Cosmochimica Acta, 55*, 3845-3867.

Therriault, A.M., Grieve, R.A.F., & Reimold, W.U., 1997. Original size of the Vredefort structure: implications for the geological evolution of the Witwatersrand Basin. *Meteoritics & Planetary Science, 32*, 71-77.

Thomas, J. B., 2003. Melt inclusion geochemistry.

Thomson, O. A., Cavosie, A. J., Moser, D. E., Barker, I., Radovan, H. A., & French, B. M. (2014). Preservation of detrital shocked minerals derived from the 1.85 Ga Sudbury impact structure in modern alluvium and Holocene glacial deposits. *Geological Society of America Bulletin*, *126*(5-6), 720-737.

Timms, N.E., Erickson, T.M., Schmieder, M., Tohver, E., & Pearce, M., 2014. Shock recrystallisation and decomposition of zircon. *77th Annual Meteoritical Society Meeting.*

Timms, N. E., Reddy, S. M., Healy, D., Nemchin, A. A., Grange, M. L., Pidgeon, R. T., & Hart, R., 2012. Resolution of impact-related microstructures in lunar zircon: A shock-deformation mechanism map. *Meteoritics & Planetary Science, 47*(1), 120-141.

Tredoux, M., Hart, R. J., Carlson, R. W., & Shirey, S. B., 1999. Ultramafic rocks at the center of the Vredefort structure: Further evidence for the crust on edge model. *Geology, 27*(10), 923-926.

Valley, J.W., Cavosie, A.J., Ushikubo, T., Reinhard, D.A., Lawrence, D.F., Larson, D.J., Clifton, P.H., Kelly, T.F., Wilde, S.A., Moser, D.E., & Spicuzza, M.J., 2014. Hadean age for a post-magma-ocean zircon confirmed by atom-probe tomography. *Nature Geoscience, 7*(3), 219-223.

Wilde, S.A., Valley, J.W., Peck, W.H., & Graham, C.M., 2001. Evidence from detrital zircons for the existence of continental crust and oceans on the Earth 4.4 Gyr ago. *Nature, 409*(6817), 175-178.

Wittmann, A., Kenkmann, T., Schmitt, R. T., & Stöffler, D., 2006. Shock-metamorphosed zircon in terrestrial impact craters. *Meteoritics & Planetary Science, 41*(3), 433-454.

Chapter 4

4 Discussion & Conclusions

4.1 Introduction

The primary objectives of this thesis were to: a) further the understanding of how shock microstructures form in zircon from the different shock environments of a complex impact structure; b) to establish a best method for the preparation and compositional analysis of impact melt inclusions in zircon; and c) to document the presence of impact melt inclusions in zircon across the Vredefort impact structure, and constrain their timing and formational mechanisms. In order to achieve these main objectives, we employed the use of a variety of electron probe techniques, including backscattered electron (BSE) and secondary electron (SE) imaging, electron backscatter diffraction (EBSD), cathodoluminescence (CL), energy dispersive spectroscopy (EDS) mapping and semi-quantitative analysis. All techniques were performed on a Hitachi SU6600 field emission gun scanning electron microscope (FEG-SEM) from Western University's ZAPLab. In the following sections, I outline how the various components of my thesis can be integrated to further the understanding of shock processes in zircon, and the impact they will have on future research.

4.2 Shock microstructural progression in zircon

We defined a new microstructural progression observed in the zircons at Vredefort. The general progression sequence is as follows:

1. Early planar features (fractures, 'microcleavage').
2. Planar deformation bands ('kinks' and 'twists'). Likely temporally related to early planar features.

3. Microtwinning.
4. Late planar features (‘microcleavage’ domains).
5. Curviplanar fracturing primarily at an oblique angle to the c-axis, and grain margin displacement.
6. Injection of impact melt glass inclusions along curviplanar (+/- planar fractures).
7. Ductile deformation (crystal plastic deformation).
8. High-T post-shock granularization/recrystallization.
    1. Some zircons exhibit only partial granularization/recrystallization.

Two different general shock pathways were defined for the zircons in this study. The variety of shock pathways, based primarily on shock conditions experienced (e.g. “hot-shock” vs. “cold-shock”), highlight the complexity of zircon reactions to shock, and the need to further study these various shock pathways. These two pathways are also distinct from those experienced in extraterrestrial zircons, such as zircons from lunar breccias or meteorite samples. We recommended that the microstructural study of zircon in terrestrial, deep-crater environments be distinguished from those of extraterrestrial or ‘ejecta-type’ zircons.

4.2.1 Applications to deciphering the stages of the impact process

By establishing these microstructural relationships, we can begin to interpret the complexity of the impact process. It is now understood that early planar features are related to the passage of the initial compressional shockwave, while later, cross-cutting twins and curviplanar features are related to the rarefaction shockwave. Microstructural interrelationships such as these have allowed us to relate planar deformation bands (kinks and twists) discovered in this study to the initial shockwave. These zircon microstructure relationships have also allowed us to fit general temporal restraints on each of the respective cratering processes. For example, this study demonstrated that the formation of

planar fractures (compression) and curviplanar features (rarefaction) is very rapid (ms^{-1}), as impact melt introduced coevally with curviplanar features also intrudes planar fractures. These planar fractures must have remained open long enough for this to occur, which appears to point toward the rate of the various shock processes. We are able to determine that impact melt glass inclusions are related most strongly to curviplanar features, thereby placing a temporal constraint on their injection. Zircon recrystallization related to high post-shock temperatures may also allow us to constrain new microstructures as 'shock-related' if they are cross-cut by such recrystallized domains.

4.3 Zircon as a quantitative scale of the shock process

The study of shock features in zircon is somewhat complicated by the diversity of impact settings from which zircon is found. For example, the types and prevalence of shock features varies from classic terrestrial deep-crater settings versus that of ejecta-environment zircons (ejecta layers, lunar soil samples, etc.). Using a microstructural survey, we quantified terrestrial shock microstructures from across the Vredefort impact structure, South Africa. In this survey, we found that the degree of planar features (including planar fractures, microtwins, planar deformation bands, and "microcleavage") decreases with increasing distance from the center of impact. Despite the heterogeneity of the impact process (and associated P/T conditions), this would suggest that a decrease in P/T conditions is reflected in the number of grains that host planar features at Vredefort. Curviplanar features, often annealed, are one of the most abundant shock microstructures in zircon at Vredefort. Their prevalence is consistent across most of the samples in this survey, except in V15-55. A strong statistical correspondence is observed between curviplanar features and impact melt inclusions, which is strengthened by their spatial

relationships. Impact melt glass inclusions are often found tracing curviplanar features, indicating a close temporal relationship and similar formational mechanism. In approximately 15-20% of zircons from most samples, grain margins appear displaced, which seems to be due to extreme levels of strain exerted on previously open (planar and curviplanar) features. There is a zone of zircon recrystallization that operates within ~4-5 km of the center of the dome.

A number of interesting and, to the best of our knowledge, novel zircon microstructures were identified. One such microstructure has been identified as a form of planar deformation band (PDB). We call this PDB a 'twist' as it is represented by a twisted appearance in EBSD misorientation maps. It appears as though these microstructures represent a twist in the zircon lattice around a planar central axis. The other microstructure is extremely coarse granular zircon found near the centre of impact. These coarse granules host their own, independent, oscillatory zonation patterns. They have darker (in BSE) rims than cores as well. This microstructure is interesting, given that these zircons were not in direct contact with a cohesive impact melt sheet, as the textures would suggest. We determined that the heat present in the deep crater (central uplift) was sufficient to closely replicate the heat present in an impact melt sheet. The presence of these rare, newly documented microstructures highlights the need for further microstructural study of zircon from complex impact structures to not only quantify the prevalence of such features, but discover new features as well.

4.4 Impact melt glass inclusions in zircon

As shown in Chapter 3, impact melt glass inclusions are one of the most common shock microstructures in zircon at Vredefort. Because of their abundance across the majority of

the central uplift, it is apparent that impact melt glass inclusions are of much significance to the future study of shocked zircon. Impact melt glass inclusions were originally documented by Moser et al. (2011). Since then, they have been further documented by Erickson et al (2013), and Crow (2015). There remained a need for a comprehensive study of impact melt inclusions across the entirety of a complex impact crater, hence the purpose of this study. Inclusions were discussed in detail in Chapter 3, and the findings are summarized and discussed below.

In this study, energy dispersive spectroscopy (EDS) was established as a valuable alternative to conventional electron microprobe analysis (EPMA) for compositional analysis. EDS is an effective compositional tool because of its incorporation into many standard scanning electron microscopes. This is exceptionally beneficial for impact melt inclusion analysis, as it allows for the time-efficient integration of classic SEM methods (i.e. EBSD, CL, BSE/SE) with EDS. The analysis of such small inclusions within a higher density phase (zircons) is difficult, and a detailed methodology was provided. This included new polishing, carbon coating, and EDS analysis methods.

Impact melt glass inclusions at Vredefort are variable from sample to sample, but also within individual zircons. Analyses show that melt inclusions always occur as homogenous compositions, and no evidence of mixing of impact melt inclusions was found. This reinforces the interpretation of partial melting as the mechanism for the generation of these inclusions. Multiple different melt inclusion compositions were found, including Na-aluminosilicate glass inclusions, K-rich aluminosilicate, and mafic inclusions, roughly matching the mineralogy of external minerals plagioclase, orthoclase, and hypersthene (orthopyroxene), respectively. The relationship of these glass inclusions

to external (and local) mineralogy (typically between ~1 wt. % difference in elemental abundances) indicates that partial melting and incorporation into the host zircon was a locally-driven process. Petrographic evidence of melting was found in the majority of samples, including granophyric textures, melt pockets, and Inlandsee Leucogranofels (generated by partial melting) texture. Impact melt glass inclusions appear to have been introduced to the host zircon sometime during shockwave rarefaction, and subsequent curviplanar feature formation. The impact melt glass inclusions are most intimately related to these curviplanar features, but are also found along annealed planar fractures. All inclusions analyzed were glass, as identified by EBSD.

4.5 Zircon as a dominant shock indicator mineral

It is well-documented that many rock-forming minerals (i.e. quartz, feldspar) suffer with the preservation of shock effects through continued igneous, metamorphic, and distal sedimentary transport events (Grieve et al., 1990). Zircon, which is incredibly robust and has a much higher melting temperature (~1676°C) than quartz or feldspar, has recently become an important tool in recording the shock history of large, complex impact structures.

4.5.1 Zircon as an archive of shock microstructures

As outlined in this study, zircon has the potential to preserve a number of shock microstructures that can be related to all key impact processes, from initial compression, to shockwave rarefaction, crater modification, and high post-shock temperatures. This preservation is in stark contrast to most minerals, which are typically known for the preservation of minimal (e.g. one or two) shock microstructures. We documented the

presence of at least 10 different shock microstructures from zircons in this study. One zircon (F617) from an intermediate location in the central uplift (V15-16) displays features related to the initial compression, rarefaction, impact-related partial melting, crater modification, and high post-shock temperatures. The incredible preservation of such an array of shock features in a single grain reveals the potential of zircon as a unique and adaptable shock indicator mineral.

4.5.2 Preservation of shock microstructures in zircon

As mentioned above, the preservation of such a high quantity of shock microstructures in zircon is incredible, but is even more impressive when compared to the surrounding main phases. Quartz and feldspar from the same rock (V15-16) are completely recrystallized, and display no shock microstructures. This particular zircon (F617) is not a rare example; in fact, the majority of zircons analyzed in this study appeared to display incredible preservation of shock microstructures in comparison to surrounding minerals. The further documentation of 2.02 Ga shock microstructures in zircon is supplementary testimony to the robustness and ability of zircon to both record and retain shock microstructures.

The microstructural preservation potential of zircon is perhaps best realized in its preservation of impact melt glass inclusions. The successful determination that glass inclusions exist in these zircons is interesting, showing that zircon is even more robust than previously thought, and acting as a natural ‘shield’ from processes that may cause devitrification or re-heating and compositional mixing of these glasses over the past 2.02 Ga. This fact may have significant applications to glass-stabilization studies in materials science. Of course, the presence of various impact melt inclusion compositions is also of potential significance for understanding shock (melting) conditions in impact craters.

4.5.3 Usefulness of zircon as a U-Pb geochronometer for the dating of impact events

U-Pb age dating is a main method of choice for dating ancient geological events due to its double U-decay chain, which provides an ‘internal verification’ of U-Pb behaviour over extended timescales (Schoene, 2014). These unique attributes allow for a consistent and reliable source of information regarding the age of various events (i.e. igneous, metamorphic, shock).

Krogh (1984) established the link between U-Pb ages and shock microstructures in zircon. This development was further advanced by studies by Bohor et al. (1993), Pidgeon et al. (2011) and Moser et al. (2011). There still remain many unanswered questions in regard to the nature of the relationship between U-Pb ages and shock microstructures. Crater-wide studies of zircon, such as in this study, are necessary to provide a catalogue of different shock features before attempting to correlate U-Pb impact ages with the various microstructures. The preservation of shock microstructures across the majority of the central uplift speaks to the potential for zircon to date impact events. Shock microstructures such as microtwinning and curviplanar features may lead to partial age-resetting in zircon (Moser et al., 2011). The abundance of these features discovered in this study highlights the potential for future U-Pb studies across the exposure of the Vredefort central uplift. Impact melt glass inclusions, which in some cases appear to outline polygonal domains, may represent a precursor to the formation of granules that date the impact. Even in the complete zircon recrystallization zone (within ~1 km of the centre of impact), the unfortunate lack of shock microstructure preservation is balanced by the ability to establish reliable U-Pb ages in recrystallized zircon.

4.6 Implications of this study on the search for and study of ancient impacts

This study has provided further proof that zircon is one of, if not the most, robust mineral on Earth. Combining its incredible ability to act as a mineral catalogue of a variety of shock processes, as well as its ubiquity in the Earth's crust and usefulness as a U-Pb geochronometer indicates that zircon should be the focus of future impact studies. As previously mentioned, between 80-100% of zircons not affected by post-shock recrystallization retained impact melt inclusions. Additionally, nearly every zircon (<90%) analyzed in this study hosted at least one type of shock microstructure. The number of shock microstructures and impact melt inclusions in these zircons implies that nearly the entire Vredefort central uplift displays some form of zircon shock evidence. The implications for this are significant, as there are many ancient impact craters that remain undiscovered or eroded, and may only be recognizable on the microstructural level. The findings of this study suggest that we should be focusing on the hunt for shock microstructures in ancient impact structures. The preservation of impact melt inclusions as glass for ~2.020 Ga is an incredible finding which only reinforces the idea that ancient impact evidence is preserved in zircons, perhaps since the Late Heavy Bombardment (ca. 4.1-3.8 Ga), of which there is no macroscopic surficial evidence on Earth. Shock evidence in zircon is not only confined to terrestrial studies, but should also be a focus in extraterrestrial materials (i.e. Apollo zircons, lunar regolith breccias, etc.).

4.7 Recommendations for future work

The progress made for impact research in this study must be continued with more comprehensive studies of zircon in other impact settings (i.e. other complex structures and *ex-situ* grains from lunar or detrital samples), for example, building on studies such as Crow (2015). Furthering the understanding of the reaction of zircon to shock will have far-reaching implications for understanding shock conditions in other settings. We suggest that more *in-situ* studies should also be performed, with a focus on quantifying the prevalence of shock effects (i.e. planar features, microtwins, impact melt glass inclusions) in zircon. Because of the heterogeneity of shock effects observed in zircon, these quantitative studies provide an important perspective on the impact process.

We established a method for the preparation and compositional analysis of impact melt inclusions in zircon, which should be expanded on and used in future studies of other impact structures or *ex-situ* zircon grains (i.e. lunar or Martian). This method is still in the developmental stage, and requires further advancement in order to perfectly analyze all sizes and compositions of melt inclusions. With further study, zircons may be able to be correlated with host terranes based on the composition of the melt inclusions they host. These melt inclusions could also provide a rough estimate of the shock conditions necessary to melt those minerals. It would be of interest to heat these melt inclusions in a vacuum furnace and record the recrystallization of the glasses to gain insight into remnant (post-impact) temperature conditions. Additionally, Raman spectroscopy and transmission electron microscopy (TEM) studies would be beneficial for further confirming the lack of crystallinity in these impact melt glass inclusions.

Understanding of the mechanisms for Pb-loss in impact-affected zircons still remains in development. Building on the work from Moser et al. (2011), and microstructural findings from this study, future investigations may benefit to focus on the link between shock microstructures in zircon and Pb-loss. Specifically, it would be interesting to understand the potential effect of impact melt inclusions on U-Pb ages in zircon.

4.8 References

Bohor, B.F., Betterton, W.J., & Krogh, T.E., 1993. Impact-shocked zircons: discovery of shock-induced textures reflecting increasing degrees of shock metamorphism. *Earth and Planetary Science Letters*, *119*(3), 419-424.

Crow, C., 2015. The early lunar magmatic and impact histories recorded by Apollo zircons (PhD dissertation). University of California-Los Angeles.

Erickson, T. M., Cavosie, A. J., Moser, D. E., Barker, I. R., & Radovan, H. A., 2013. Correlating planar microstructures in shocked zircon from the Vredefort Dome at multiple scales: Crystallographic modeling, external and internal imaging, and EBSD structural analysis. *American Mineralogist*, *98*(1), 53-65.

Grieve, R.A.F., Coderre, J. M., Robertson, P. B., & Alexopoulos, J., 1990. Microscopic planar deformation features in quartz of the Vredefort structure: Anomalous but still suggestive of an impact origin. *Tectonophysics*, *171*(1), 185-200.

Kerrick, D. M., Eminhizer, L. B., & Villaume, J. F. (1973). The Role of Carbon Film Thickness in Electron Microprobe Analysis. American Mineralogist, 58, 920-925.

Krogh, T.E., Davis, D.W., & Corfu, F., 1984. Precise U-Pb zircon and baddeleyite ages for the Sudbury area. In *The geology and ore deposits of the Sudbury structure*, *1*, *431-446*. Ontario Geological Survey.

Moser, D. E., Cupelli, C. L., Barker, I. R., Flowers, R. M., Bowman, J. R., Wooden, J., & Hart, J. R. (2011). New zircon shock phenomena and their use for dating and reconstruction of large impact structures revealed by electron nanobeam (EBSD, CL, EDS) and isotopic U-Pb and (U-Th)/He analysis of the Vredefort dome. *Canadian Journal of Earth Sciences*, *48*(2), 117-139.

Pidgeon, R.T., Nemchin, A.A., & Kamo, S.L., 2011. Comparison of structures in zircons from lunar and terrestrial impactites. *Canadian Journal of Earth Sciences, 48,* 107-116.

Schoene, B. (2014). 4.10-U–Th–Pb Geochronology. *Treatise on Geochemistry, Second Editionth edn. Elsevier, Oxford*, 341-378.

Appendices

Appendix A: Detailed Methodology

All samples used for this study followed a similar sampling and preparation procedure. Some samples were prepared as thin sections, while others were prepared as thick sections so as not to disturb the sample surfaces that were, in some cases, already analyzed. The exact sampling and preparation procedure followed is described below.

Sampling

A total of 11 samples were analyzed. Of these, six samples (V15-39, V15-45-1, V15-16, V15-46, V15-56, V2-2, V15-55) were collected during fieldwork in February, 2015. The other samples (V-62, V49-1, V2-1, V09-237) were taken from the pre-existing sample collection at Western University's ZAPLab.

Final sample selection followed the following 'protocol': 1) sample as many areas of granitoid exposure from a variety of areas throughout dome, focusing on areas of known geological relevance (i.e. proximal to pseudotachylite quarries etc.) 2) from these collected samples, an effort was made to study specific samples that would represent a consistent transect from the core to the collar of the central uplift. Due to sparse exposure in some areas, we studied samples from every ~2-4 km across the structure.

The samples collected during fieldwork followed a consistent collection procedure. First, regional field photographs were taken to characterize the sample locations, followed by a sample photograph and notes on the surrounding geology. Each sampling station required a UTM (+/-3m) coordinate to be recorded (Appendix B). This, combined with the photographs and notes taken, ensured that the locations could be easily found again if necessary. Using a sledgehammer, hand samples were collected from the most pristine, unweathered sample surfaces available. The samples were separately bagged in order to decrease the likelihood of potential contamination. After collection, all samples were entered into a Google Earth map. This Google Earth map consists of an amalgamation of samples from February 2015 field work, as well as samples from previous field excursions, resulting in an electronic map of over 150 sample locations.

Sample Preparation

As previously mentioned, due to the state of the pre-existing samples from previous work, not all samples were prepared exactly the same. Where possible, samples were made into thin sections in Steve Wood's laboratory at Western University.

A total of seven samples were prepared as thin sections. One sample (V09-237) was a zircon mount. The other three samples remained as thick sections, as any further cutting or polishing would destroy many important features on the already exposed surface of the thick section.

Thin and thick sections were polished successively with 120 grit, 9 µm, 6 µm, 1 µm, and 0.25 µm polishing pads. This was followed by between 1.5-3.0 hours on a Buehler VibroMet 2 vibratory polisher with a neutral colloidal alumina polishing solution at Western University's ZAPLab. The use of this vibratory polisher was necessary for successful electron backscatter diffraction. In order to reduce charging and beam drift in the SEM, all samples were carbon coated with ~25 nm of carbon in an Edwards Auto 306 carbon coater at Western University. The carbon coat thickness is also very important for accurate compositional analysis with energy dispersive spectroscopy; therefore, the amount of carbon coating on each sample was measured with a combination of two techniques. First, a polished brass disk was placed beside the standards and samples, and was used to roughly estimate the thickness (~25 nm) based on interference colours, following the method of Reed, 1975, shown in Table A-1. Once a satisfactory approximation of carbon thickness was obtained, the samples and standards were analyzed under the SEM. A piece of pure silicon standard coated simultaneously with the samples and standards was analyzed for carbon thickness. The k-ratios of carbon and silicon were used to calculate the actual carbon thickness on the samples and standards with a program created by Yves Thibault. This provided a verifiable and reproducible carbon coat thickness result, which is imperative to the proper analysis of composition with energy dispersive spectroscopy.

Thickness (nm)	Interference Colour
15	Orange
20	Indigo Red
25*	Blue
30	Bluish-Green
35	Green Blue
40	Pale Green

Table A-1: Chart of interference colours on carbon coated brass (Reed, 1975). *Target carbon coat thickness used in this study.

Standard Preparation

The standard materials used for semi-quantitative energy dispersive spectroscopy (EDS) were selected based on the elements within the samples being analyzed. Table A-2 shows the standards used for each element in this study.

Element	Glass Standard Reference
K	SEM mineral std. MAD-10 feldspar
Mg	K-412
Na	K-373
Fe	SEM mineral std. Fe
Si	NMNH Rhyolite (VG-568)
Al	K-495
Ca	K-411
Zr	SEM mineral std. zircon

Table A-2: Table displaying the major elements standardized in this study, and their corresponding glass standard reference. Glass standards provided by SPI supplies and C. M. Taylor Company, and Jarosewich (2002). Mineral standards were built-in to the SEM-EDS system.

The standard materials were prepared in an epoxy mount. The epoxy mount was made by pouring a combination of Struers Epofix Resin and Struers Epofix Hardener together (5:1 ratio) onto a piece of carbon tape with the standard materials attached. The epoxy was then cured overnight so that it hardened properly. Once hardened, the standard materials were polished with the same procedure as the thin and thick section samples. Finally, the standard mount was coated with approximately 25 nm of carbon, the same amount as the samples. Coating the standards and samples with the same amount of carbon reduces the error associated with any corrections that need to be made.

Optical Petrography

Thin sections were analyzed with optical petrography to observe mineralogy and textural relationships that can be used in tandem with scanning electron microscopy observations. The grain mount and thick section samples were not analyzed with optical petrography.

Optical petrography was performed with a Nikon Eclipse LV100 POL microscope at Western University's ZAPLab. Sample descriptions are provided in Appendix B.

Analytical Techniques

The majority of the analytical work for this study was performed on a Hitachi SU6600 field emission gun scanning electron microscope (FEG-SEM) at Western University's ZAPLab.

Samples were first feature mapped and phase mapped in order to locate accessory phases of interest, such as zircon, and to provide insight into the mineralogy of the sample. After this mapping, the samples could be analyzed by techniques which included: backscattered electron (BSE) and secondary electron (SE) imaging; electron backscatter diffraction (EBSD); cathodoluminescence (CL); quantitative energy dispersive spectroscopy (EDS); and EDS mapping.

Feature Scanning

Each thin and thick section was initially feature scanned using INCA software in order to identify the various accessory phases within the sample. A formula was used to identify zircon, baddeleyite, monazite, and zirconalite. The locations of these features were saved and later georeferenced so that they could be relocated. The settings used for feature scanning were as follows (Table A-3):

Feature Scanning	
Carbon coat thickness	~25 nm
Accelerating voltage	15 kV
Probe Current	--
Gain	Medium
Working distance	10 mm
Apertures	3/1 (50 µm/200 µm)
Magnification	150x

Table A-3: Settings used for feature mapping.

Phase Mapping

All samples were mapped with INCA's phase map feature. This mapping identified the various main phases (i.e. quartz, plagioclase, etc.) within the sample, and assisted in the

optical petrography analysis (Appendix B). The settings used for the phase mapping are shown in Table A-4.

Phase Mapping	
Carbon coat thickness	~25 nm
Accelerating voltage	15 kV
Probe current	--
Gain	Medium
Working distance	12 mm
Apertures	3/1(50 μm/200 μm)
Magnification	90x

Table A-4: Settings used for phase mapping.

Backscattered Electron (BSE) and Secondary Electron (SE) Imaging

All samples were examined with backscattered electron imaging (BSE). Incident electrons will backscatter based on elastic scattering from interactions with specific atoms. This scattering is controlled by the atomic number of the elements being analyzed. Heavier elements (high atomic number) will backscatter electrons more powerfully than lighter elements, ultimately creating a contrast difference between different minerals (Okabe et al., 2000). BSE was used in this study to characterize the mineralogy and textures of each sample, and for a reconnaissance survey of zonation patterns and shock microstructures in zircon. Images were taken at low magnification (typically 90-150x), medium magnification (~300x), and high magnification (fully zoomed). In some distinct cases, highly zoomed images of areas of interest were taken to further characterize the grain textures.

Simultaneously, samples were analyzed with secondary electron imaging (SE). In SE, incident electrons collide with sample atoms, displacing electrons down from outer shells, and creating weaker secondary electrons that are emitted and caught by a detector. SE imaging provides information about surface topography, as a scan moving across a hole or depression, the number of secondary electrons emitted is reduced. Likewise, a scan moving across a bulge or topographic high will emit a higher number of secondary electrons. Again, images were taken at low magnification (typically 90-150x), medium magnification (~300x), and high magnification (fully zoomed). Samples were imaged with the following BSE/SE settings (Table A-5).

BSE/SE Settings	
Carbon coat thickness	~25 nm
Accelerating voltage	15 kV
Gain	Medium
Probe current	--
Working distance	10.0 mm
Apertures	3/1 (50 μm/200 μm)
Tilt	--

Table A-5: Standard settings used for backscattered electron and secondary electron imaging.

Zircon grains analyzed by BSE/SE were chosen due to length, with the larger zircon grains (by length) being imaged first. Due to inherent time constraints with this analysis, typically between 15-20 of the largest zircon grains were imaged in each sample. The analysis by BSE/SE imaging was used in order to identify target grains for further analysis by methods such as electron backscatter diffraction, cathodoluminescence, and energy dispersive spectroscopy, as outlined below.

Samples V15-39, V15-16, V49-1, V15-46, V-62, and V15-55 were selected for a comprehensive zircon shock microstructure survey (Appendix D). Approximately 40-50 of the largest (by area) zircon grains were selected from each sample to provide an unbiased survey. These grains were all observed to account for various shock features. Where possible, to best display the variety of shock features in BSE, the survey was conducted with lower kV settings. Samples that were not favorable under low kV were imaged with standard BSE/SE settings.

Electron Backscatter Diffraction (EBSD)

Following the initial BSE/SE imaging, certain zircons were selected for electron backscatter diffraction (EBSD). These grains were selected based primarily on the presence of interesting microstructures, including impact-related melt inclusions.

In EBSD, an electron beam is directed at a tilted, polished sample. If the sample is crystalline and well-polished, then the electrons that are diffracted tend to form recognizable patterns called Kikuchi bands on a fluorescent screen (detector). The patterns created are related to the crystal structure and orientation of the sample under the

beam, which provides information on micro-scale crystallographic orientation. This information can be portrayed in a number of different ways. In this study, we use inverse pole figure (IPF) maps and misorientation maps. IPF maps show the distribution of crystallographic directions parallel to various sample directions. IPF maps are convenient for visualizing certain textures, such as microtwinning in zircon, or different growth phases of zircon. Misorientation maps display the misorientation of a crystal relative to a single point. This representation is better for the visualization of lower angle grain boundaries (i.e. planar/curviplanar features) or crystal plastic deformation which may not be represented in IPF maps. Tables A-6 and A-7 show the parameters used for the EBSD analyses in this study.

EBSD Settings	
Carbon coat thickness	~25 nm
Accelerating voltage	20 kV
Gain	Medium
Probe current	--
Working distance	19.0 mm
Apertures	3/2 (50 μm/100 μm)
Tilt	70°

Table A-6: Electron backscatter diffraction (EBSD) parameters.

SEM model	Hitachi SU6600
EBSP collection time per frame (ms)	19
Background (frames)	64
EBSP noise reduction (frames)	7
(binning)	4x4
(gain)	High
Hough Resolution	80
Band Detection min/max	5/7
Step distance (μm)	Between 0.1 – 0.3 μm

Average mean angular deviation (zircon)	Between 0.2-0.5°
Noise reduction- “wildspike”	yes
n neighbor zero solution extrapolation	0
Kuwahara Filter	--

Table A-7: Advanced electron backscatter diffraction settings. **Average mean angular deviation values (MAD) are well below zircon cutoff of 1.3° in all cases.**

Cathodoluminescence (CL)

Cathodoluminescence (CL) is a useful tool in the reconstruction of geological histories, especially for luminescent minerals such as zircon. Cathodoluminescence (CL) is the emission of photons with a characteristic wavelength after bombardment by high-energy electrons. Some minerals are more fluorescent than others, and luckily, zircon is highly fluorescent. CL emission is controlled by a number of factors, including composition, strain or damage, and lattice structure. Upon bombardment, electrons belonging to the lower energy valence band jump up to the higher energy conduction band. When these electrons relax and return to their ground state, they can be trapped momentarily by structural defects or impurities (traps). Energy lost in these traps is emitted as energy (wavelength in visible spectrum). The density of these traps generally provides the function of CL intensity.

CL can be used to provide information about the growth history of a zircon, including recrystallization events from high temperature exposure, as well as identify any deformation within the zircon crystal. CL was performed on many of the zircon grains analyzed. The settings used in this analysis are listed in Table A-8, below.

CL Settings	
Carbon coat thickness	~25 nm
Accelerating voltage	10 kV
Gain	Medium
Probe current	--
Working distance	12.5 mm
Aperture	2/3 (100 μm/50 μm)
Tilt	--

Table A-8: Settings used for cathodoluminescence analysis.

Quantitative Energy Dispersive Spectroscopy (EDS)

Energy dispersive spectroscopy (EDS) is an analytical technique designed to communicate the elemental and chemical information of a sample. The technique relies on a series of interactions which emit a characteristic X-ray corresponding to a certain element. An electron beam emits a stream of electrons which excite electrons from an inner orbital shell, causing that electron to be released, and an outer shell electron to fill the void left behind. The energy difference between the higher energy outer shell and the lower energy inner shell is emitted as a characteristic X-ray (Kα, Kβ, or Lα radiation). A characteristic X-ray is a distinguishable peak among continuum X-rays (background). They correspond to certain elements, and therefore a measurement of count rates and X-ray energies can be used to measure elemental composition of a sample.

One of the main issues that arises in performing quantitative EDS is the failure to properly account for carbon coat thickness, which can lead to incorrect compositional totals. As carbon coating is essential to avoid beam drift during EBSD, CL, and BSE/SE, an accurate measurement of thickness was necessary. This measurement was established, and is outlined in Section 3.2. Another common issue that occurs with EDS analysis of glass is alkali mobility. Na and K in glass are quite mobile under an electron beam (Morgan & London, 2005). Considering these issues, we attempted to diminish the effects of alkali mobility by modifying the parameters used in analysis (i.e. accelerating voltage, beam current, time of beam on sample etc.) (Table A-9). Specifically, we used a lower accelerating voltage and beam current to reduce the penetration depth and sample heating. We used a shorter beam count-time to reduce the chance of significant alkali mobility. We also routinely took 2-3 analyses of each spot in order to track the mobility of Na and K. After the fine-tuning of the parameters, we saw no significant alkali mobility in any of the analyses taken. This was likely due to the relatively short duration that the samples (and standards) were exposed to the beam, as well as the lower accelerating voltage and beam current that was used.

Detector	X-max SSD detector (Oxford Instruments)
Carbon coat thickness	~25 nm
Accelerating voltage	7 kV
Probe current	Variable
Working distance	10.0 mm
Apertures	4/3 (30µm/50µm)
Gain	Medium 6.0?
Image res.	512x512

Process time	5 seconds
Frames	1 (26.7 seconds/frame)
Spectrum range	0-20 keV
Speed	Medium

Table A-9: Run conditions for Quantitative EDS analyses.

For the analysis to be fully quantitative, the elements in the sample must be "standardized." Using a suite of standards (Table A-1 & Appendix F) of known elemental composition as a reference for the analysis of a sample, increased accuracy can be obtained, which is an essential component to any elemental analysis. The conditions used for the quantitative EDS work are included in Table A-9. These settings were chosen based on numerous trial and error attempts, as the inclusions being analyzed are often both submicron-sized and quite shallow. The chosen settings reduced the incorporation of surrounding zircon into the analysis while still collecting enough data from the inclusions themselves. These settings could be considered the best EDS settings for the analysis of μm -submicron scale impact melt inclusions in zircon.

Despite relatively high totals (typically between 95-100%), we have normalized all results in order to provide an accurate depiction of relative elemental totals in each grain. The elemental abundances were calculated while calculating oxygen by stoichiometry.

EDS elemental mapping was also performed on a number of samples. The run conditions are listed in Table A-10. All quantitative results are displayed in Appendix E.

Detector	X-max SSD detector (Oxford Instruments)
Carbon coat thickness	~25 nm
Accelerating voltage	10 kV
Probe current	Variable
Working distance	10.0 mm
Apertures	2/1(100 μm/200 μm)
Gain	Medium
Image res.	512x512
Process time	5 seconds
Map dwell	100 μs

Linescan dwell	2000
Frames	6.55 sec/frame
Spectrum range	0-20 keV

Table A-10: Run conditions for EDS elemental mapping analyses.

Appendix B: Sample Locations

Sample	Lithology	Sample Type	Distance from center	Coordinates (UTM)	
V15-45-1	Inlandsee Leucogranofels	Thin Section	<1.0 km	550161 m E	7011662 m S
V09-237	Inlandsee Leucogranofels	Grain Mount	~4.0 km	549589 m E	7006647 m S
V15-39	Inlandsee Leucogranofels	Thin Section	~5.0 km	543699 m E	7014140 m S
V15-16	Inlandsee Leucogranofels	Thin Section	~8.6 km	540091 m E	7010527 m S
V49-1	Charnockite	Thick Section	~8.9 km	542531 m E	7010527 m S
V2-1	Charnockitic Gneiss	Thick Section	~11.4 km	540804 m E	7019340 m S
V15-46	Outer Granite Gneiss	Thin Section	~17.1 km	539943 m E	7025719 m S
V15-56	Outer Granite Gneiss	Thin Section	~19 km	560295 m E	7025905 m S
V-62	Alkali Syenogranite	Thick Section	~22.8 km	563809 m E	7030330 m S
V15-55	Quartzite	Thin Section	~24.5 km	563809 m E	7030330 m S

Appendix B-1: Sample lithology, type, and locations within the Vredefort dome.

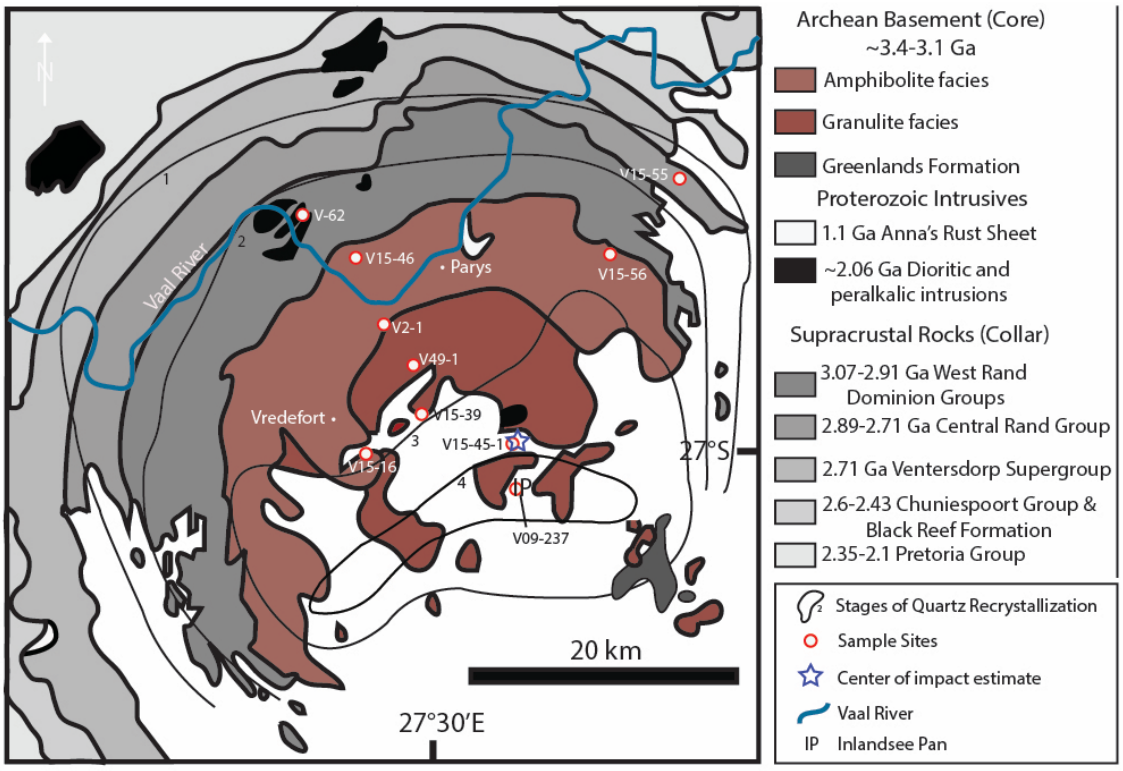

Appendix B-2: Geologic bedrock map of Vredefort impact structure, South Africa, showing the locations of samples used in this study. Map adapted from Moser et al. (2011) and Grieve et al. (1977).

Appendix C: Sample Descriptions

V15-45-1:

V15-45-1 is a typical Inlandsee Leucogranofels (ILG)-type rock. The sample was retrieved from a large boulder outcrop, as is evidenced by the light weathering of the rock itself (orange-colouring) (Figure C-1). The mineralogy of this rock is quartz + orthoclase + minor plagioclase + minor muscovite (Figure C-2, Table C-1). This fine-medium grained rock contains recrystallized quartz grains into micrometer sized fragments, as is typical of ILG rocks (glomerogranular texture) (Fig. C-3). Triple junctions are present at the boundaries of these quartz grains. Upon close examination, there is a weak coarser grained foliation delineated by these recrystallized quartz grains, but the rock remains relatively granoblastic**.** There are absolutely no optically-resolvable shock features in the quartz or feldspars of this sample. This observation is to be expected based on Grieve et al.'s (1990) analysis of core samples. According to the phase map (Fig. C-2), almost all zircons are found within the orthoclase, which is also heavily recrystallized. Few zircons are found within quartz, and even those are spatially related to the orthoclase.

Figure C-1: V15-45-1 hand sample.

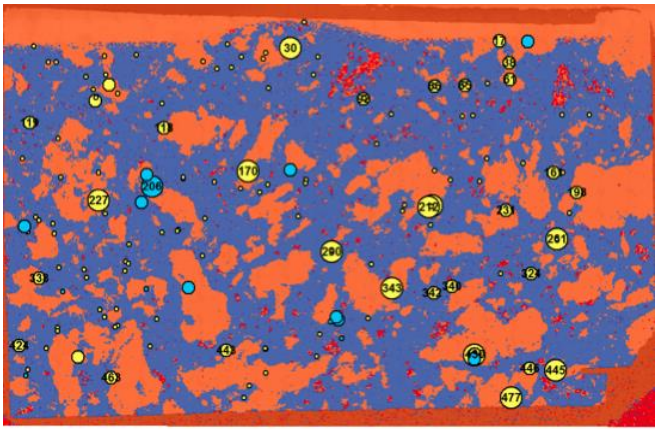

Figure C-2: V15-45-1 phase map showing quartz (orange), orthoclase (blue), and plagioclase (red).

Mineral	Shape	Modal % Estimate	Colour in PPL
Quartz	subhedral-anhedral	30	white/yellow
Orthoclase	euhedral-anhedral	65	white/clr
Plagioclase	anhedral	5	white/clr
Muscovite	anhedral	less than 1%	colourless

Table C-1: Mineralogy of V15-45-1

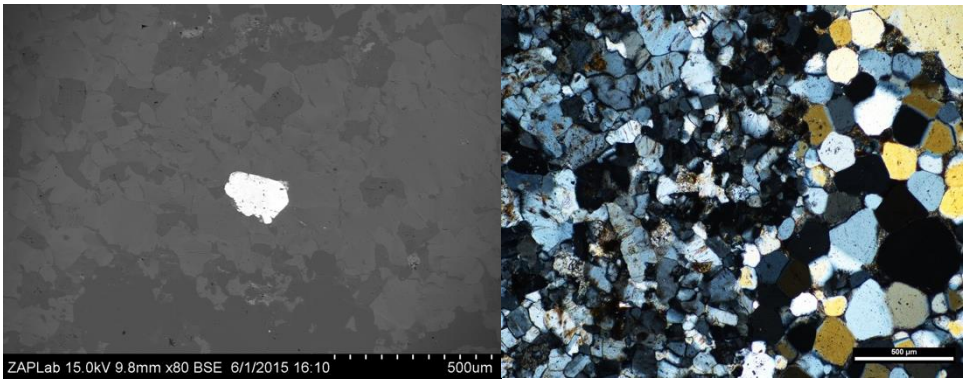

Figure C-3: BSE texture and optical photography of recrystallized "glomerogranular" quartz grains.

V09-237:

This sample is an epoxy grain mount. See Moser et al. (2011) for full sample description.

V15-39:

V15-39 is a pink-white rock (Fig. C-4) with a significant contribution of plagioclase, orthoclase and quartz (Fig. C-5). There is a distinct gneissic (compositional) banding that is seen primarily from the pink to lighter 'layers.' This is also seen in the thin section as well (Fig. C-6). Based upon the hand sample, this could be called a syenitic gneiss (ILG). Quartz in thin section is intensely recrystallized (much like V15-45-1). These quartz grains are recrystallized into glomerogranular quartz grains, retaining the shape and orientation of their original quartz grains. V15-39 is fine-medium grained, with triple junctions at the boundaries of quartz grains, as typical of metamorphic and recrystallized samples. Plagioclase grains are typically quite fine-grained, probably due to recrystallization effects from the impact. Quartz grains do not appear to host many (if any) shock features, as is noted by Grieve et al.'s (1990) analysis of ILG rocks from the core. The foliation is evident in thin section as well, with quartz (even if recrystallized) still displaying the gneissic foliation that is obvious in hand sample. There does not appear to be any exclusivity to the location of the zircons in this sample, however they do preferentially appear along grain boundaries, specifically between quartz and the feldspars.

Figure C-4: V15-39 hand sample photograph.

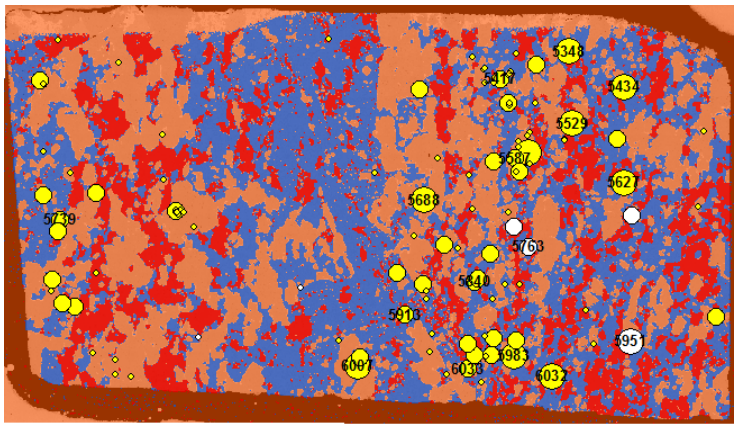

Figure C-5: V15-39 showing plagioclase (red), quartz (orange), and orthoclase (blue), with yellow dots (zircon), and white dots (monazites).

Mineral	Shape	Modal % Estimate	Colour in PPL
Orthoclase	Subhedral-anhedral	~40	white
Quartz	Euhedral-subhedral	~30	white
Plagioclase	subhedral-anhedral	~15-20	white

Table C-2: V15-39 Mineralogy

V15-16:

This sample is a milky grey-white rock with significant biotite and minor pyroxene contribution. No major or obvious foliation is visible in the hand sample, however a weak foliation/lineation may be present. V15-16 is a fine to medium grained rock that has been metamorphosed to ~granulite facies, based partly on the noted presence of clinopyroxene. Based on the hand sample, this rock could be called a granodioritic gneiss, however the foliation in the sample is quite weak. This fine-medium grained rock contains recrystallized quartz grains into micrometer sized fragments, as is typical of ILG rocks (glomerogranular texture). The extent of this is less than in ILG rocks from closer to the core (V15-45-1/V15-39). Triple junctions are present at the boundaries of these quartz grains. There may be a weak coarser grained foliation followed by the recrystallized grains (difficult to tell), but the rock remains relatively granoblastic. Clinopyroxene is evident, but in very minor proportions. The presence of cpx probably displays the amphibole→ cpx + H_2O that often accompanies granulite facies metamorphism. Plagioclase and orthoclase grains are heavily recrystallized into very small grains,

however there do remain some larger, not recrystallized k-spar. What appear to be apparently annealed and (decorated?) PDF's show up in optical microscopy in orthoclase. Kink-bands are seen in biotite grains. Interestingly, the quartz does not show any obvious evidence of shock features (PDFs). This matches Grieve's analysis of quartz from the core of the dome, and these PDF's were likely erased by high post-shock thermal action. The zircons in this sample are preferentially found within or directly related to the biotite grains.

Figure C-6: V15-16 hand sample.

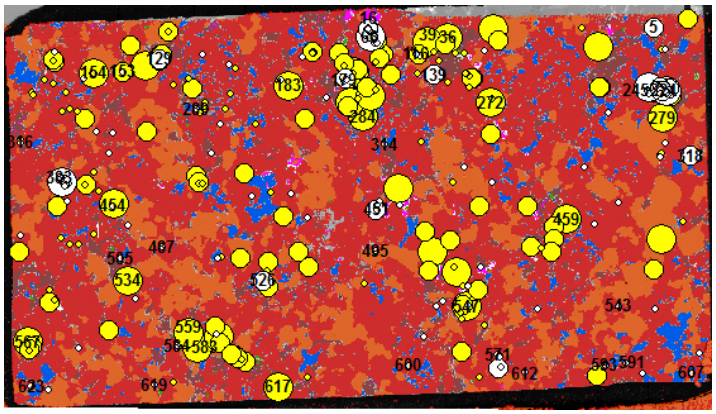

Figure C-7: Phase map of V15-16 showing plagioclase (red), quartz (orange), biotite (brown), orthoclase (blue), and clinopyroxene (pink). Yellow dots (zircon), white dots (monazites).

Mineral	Shape	Modal % Estimate	Colour in PPL
Plagioclase	subhedral	~58%	white
Quartz	euhedral-subhedral	~23%	white-yellow
Biotite	sub-anhedral	~8%	light-dark brown
Orthoclase	sub-anhedral	~8%	colourless
Clinopyroxene	subhedral	<1%	light green

Table C-3: Mineralogy of V15-16.

V49-1:

V49-1 is a deformed tonalitic gneiss dated at ~3.1 Ga (Moser et al., 2001). Further information is provided by Moser et al. (2001).

V2-1:

V2-1 is a coarse-grained green-grey rock. There appears to be some type of gneissic foliation, with bands of predominantly quartz cutting through the rock. This rock is located at approximately the gradational change from granulite-amphibolite facies rocks. It is assumed that this rock underwent granulite facies metamorphism. The mineralogy that is seen in hand sample includes quartz, plagioclase, and hypersthene (orthopyroxene) with minor clinopyroxene. The proper name for this rock would be charnockitic gneiss. In thin section, the mineralogy is plagioclase feldspar + quartz + pyroxene (hypersthene) + minor titanomagnetite. The zircons (and monazites) in V2-1 are primarily concentrated within or near the pyroxene grains. Very seldom are they found in the feldspar or quartz-dominated zones.

Figure C-9: V2-1 hand sample.

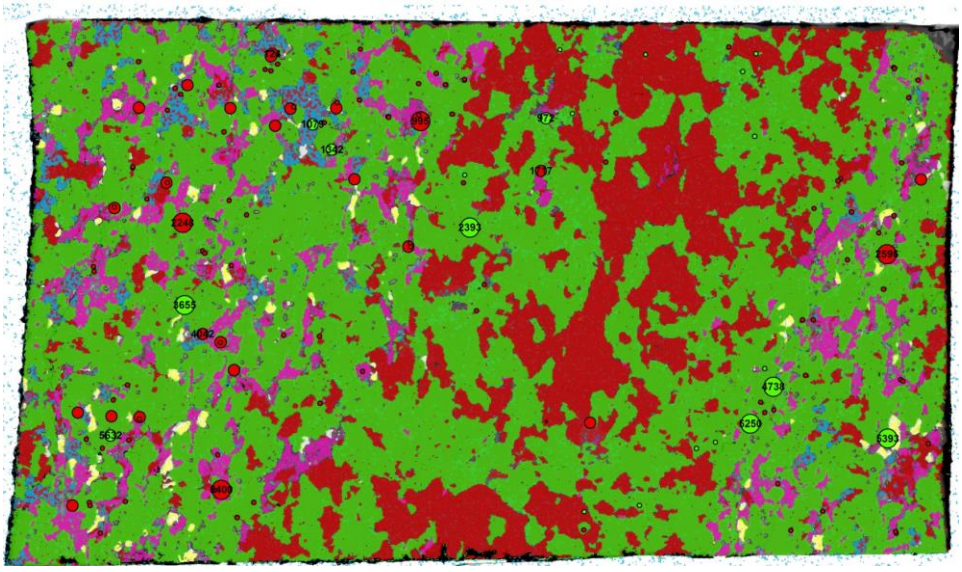

Figure C-10: V2-1 phase map. Red=quartz, opx=purple, cpx=blue, plagioclase=green, yellow=titanomagnetite. Red dots=zircon, green dots=monazite.

V15-46:

This rock is a predominantly white-grey, medium-grained granitic rock composed of plagioclase, quartz, and orthoclase. There appears to be a considerable contribution of biotite as well, with potentially some hornblende. In thin section, the mineralogy identified is plagioclase + quartz + orthoclase + biotite + muscovite + minor horneblende. V15-46 is a medium-coarse grained (with some minor fine-grained areas) granitoid rock. It appears as though there is a weak foliation delineated predominantly by the alignment of the darker biotite grains. This is also apparent in hand sample. This rock belongs to the Outer Granite Gneiss (OGG), and as such, has been weakly amphibolitized. The high presence of quartz indicates that the amphibolite-facies metamorphic event was not that

strong, which is also indicated by the low percentage of hornblendes. Quartz grains quite obviously display PDF's (planar deformation features), multiple orientations of which appear to be found in each individual grain. There is some myrmekite, which is common in amphibolite-facies rocks. The zircons in this sample are preferentially found within the feldspars (plagioclase and orthoclase), and along grain boundaries with quartz.

Figure C-11: V15-46 hand sample.

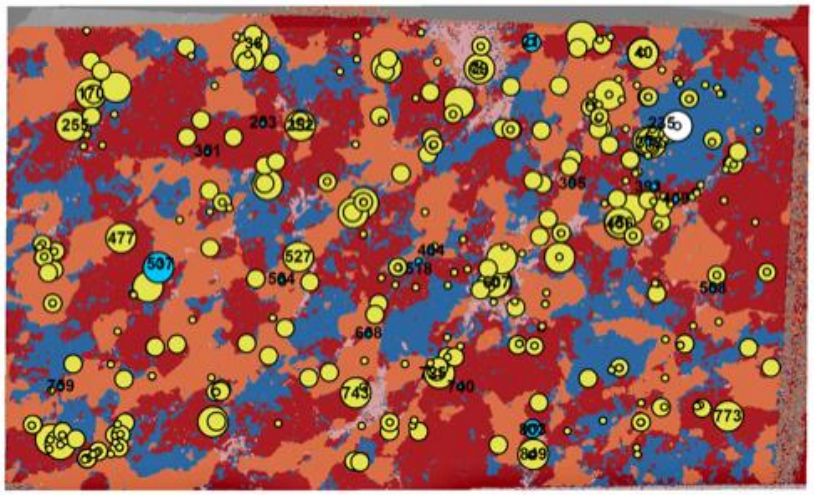

Figure C-12: V15-46 phase map showing plagioclase (red), quartz (orange), orthoclase (blue), and biotite/muscovite (pink). Horneblende not shown (minor phase). Yellow dots (zircon), white dots (monazite), blue dots (baddeleyite).

Mineral	Shape	Modal %	Colour in PPL

		Estimate	
Plagioclase	anhedral	~30	colourless
Quartz	subhedral-anhedral	~20-25	colourless-yellow (thickness)
Orthoclase	subhedral-anhedral	~20	colourless
Biotite	subhedral-anhedral	~5	brown
Muscovite	subhedral-anhedral	less than 1	colourless
Hornblende	anhedral-subhedral	less than 1	green-brown

Table C-4: Mineralogy of V15-46.

V15-56:

The V15-56 hand sample displays a typical gneissic form, with some potassium feldspar, quartz, plagioclase, muscovite and hornblende. The sample is coarse grained, with mm to cm-scale grain size. The obvious compositional banding of orthoclase tells us this sample is a gneiss (Outer Granite Gneiss-OGG). V15-56 is a typical OGG rock, metamorphosed to ~amphibolite facies (hornblende). The gneissic form is seen in thin section as well, delineated best by the amphiboles and feldspars. There has not been much evidence of large-scale melting or recrystallization in this sample. The feldspars appear to be riddled with inclusions. Orthoclase is only found locally in one section of the thin section, as it is present in gneissic bands. Quartz grains show extensive undulose extinction, as well as obvious PDF's (annealed). Plagioclase is quite abundant, and is also riddled with inclusions. Zircons in this sample appear to be preferentially found within plagioclase or spatially related to biotite grains. They appear to avoid congregation within the quartz grains and orthoclase.

Figure C-13: V15-56 hand sample

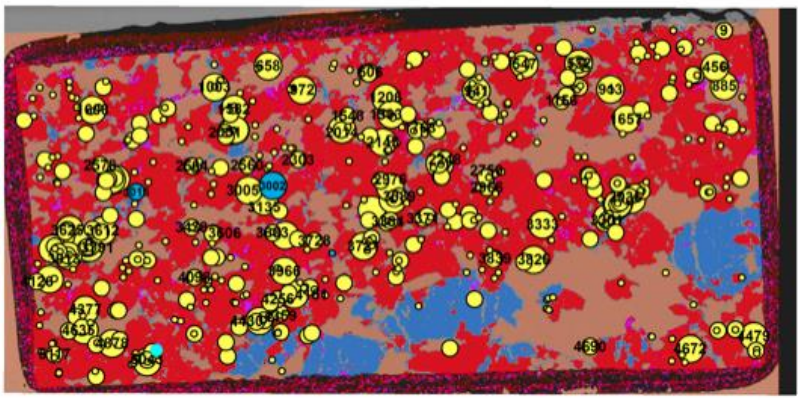

Figure C-14: V15-56 phase map showing plagioclase (red), quartz (orange), orthoclase (blue), horneblende (purple). Zircons (yellow dots), monazites (blue)

Mineral	Shape	Modal %	Colour in PPL

		Estimate	
Plagioclase	anhedral	55-60	colourless
Quartz	subhedral-euhedral	20	colourless
Orthoclase	anhedral	10-15	colourless
Muscovite	sub-anhedral	less than 1	colourless
Hornblende	sub-euhedral	5 or less	green-brown

Table C-6: Mineralogy of V15-56

V-62:

V-62 (2.052 Ga; Graham et al, 2005) is a primarily dark grey-green rock with some pink zones (feldspar). The grey-green appearance of the bulk of the rock comes from the quartz (grey-white) and acmite (green). V-62 is a coarse grained rock with a massive appearance, lacking the typical gneissic foliation seen in the granite gneisses from the core. The zircons in this sample are preferentially found within or directly related to the acmite grains. Interestingly, the acmite seems to have preserved similar planar features as those seen within the zircons, and there is often a 'moat' of material around zircons that appears similar in composition to the melt inclusions in zircons. Further information is provided in Moser et al. (2011).

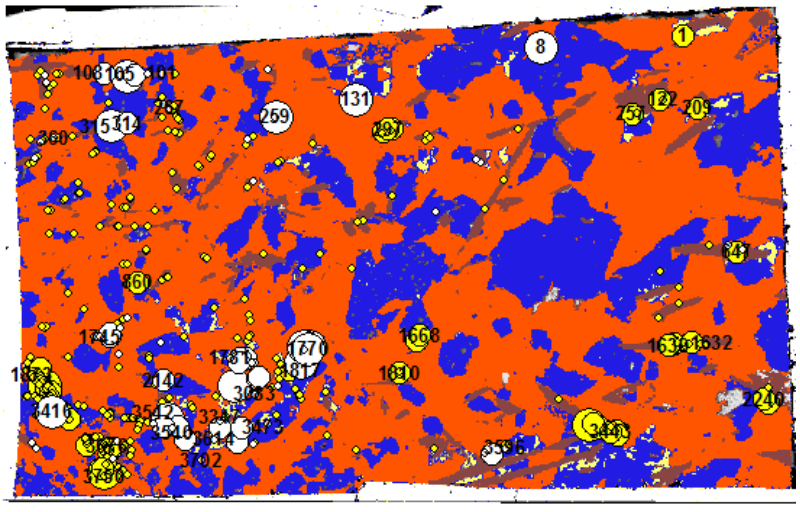

Figure C-14: Phase map of V-62 showing quartz (orange), orthoclase (blue), apatite (white), and acmite (brown). Plagioclase was difficult to differentiate from quartz in this phase map, and is also shown as orange. Zircons are yellow dots, monazites are white dots.

Mineral	Modal % Estimate
Quartz	~45
Plagioclase Feldspar	~15-20
Alkali Feldspar	~30
Acmite	~5
Apatite	~less than 1

Table C-7: Mineralogy of V-62

V15-55:

V15-55 is a quartzite from an area of the Witwatersrand Supergroup that is known to host stishovite and coesite (Martini, 1978). No evidence of stishovite or coesite was specifically found in the thin section analyzed. This rock is a medium-grained quartzite, defined by triple junctions between quartz grains. A phase map for this sample was not created, as it was evident that the sample was entirely consisting of quartz.

Appendix D: Shock Survey Results

Sample	Area (sq. um)	Shocked?	Zonation Pattern Type	Planar Features	Microtwins	Curviplanar Features	Melt inclusions	Granular/polycrystalline texture	CPD	Displacement/shear
V15-39			*Oscillatory or Sector*				note if polyphase or pods	partial (P) or total (T)		
6032	2266	X	mostly secondary	X	probably	?	appear primary	Partial	?	none
5434	1951	X	secondary, some oscillatory preserved in rim	none	none	none	appear primary	P (almost complete, rim preserved)	mostly between 'granules'	none
5348	1832	X	Oscillatory with secondary	none	none	none	appear primary	partial	X	none
6007	1677	X	Oscillatory with secondary	X	probably	X	X	none	?	none
5474	1131	X	Secondary	X	?	none	none	none	?	none
5983	876	X	Oscillatory with secondary	X	probably	none	primary	partial (minor)	?	none
5627	815	X	Oscillatory with secondary	?	?	?	priamry	partial	?	?
5688	793	?	?	none	none	none	none	Total	?	((minor, along recrystallized granule area)
5840	761	X	Oscillatory with secondary	?	?	?	primary	Partial	?	none
5529	760	X	none	none	none	none	primary?	Total	?	none
6033	691	X	?	none	none	none	primary	total (or close to)	X	none
5913	544	X	Oscillatory	X	X	X (minor)	X	none	?	none
5587	515	X	Oscillatory with secondary	none	none	possible	X	partial	?	none
5417	467	X	oscillatory	none	none	none	some small inclusions	none (to partial)	?	none
5680	437	X	oscillatory with disturbed core	none	none	none	primary	none	?	none
5739	424	?	Oscillatory	?	none	none	primary and along fractures	none	?	none
6006	386	?	Oscillatory	none	none	none	primary	partial	?	none
5962	349	X	Oscillatory	none	none	none	primary and along fractures	partial	?	none
5984	332	X	Oscillatory	none	none	none	primary with one odd incl	partial	?	none
5897	329	X	Oscillatory	none	none	none	primary	partial	?	none
5985	315	X	Oscillatory	none	none	none	primary	none	?	none
5767	294	X	Oscillatory	none	none	none	primary	partial	?	none
5896	262	X	Oscillatory	none	none	none	primary	some partial at bottom of grain	?	none
5382	248	X	none	? maybe	none	none	primary	partial in core, outer as well?	?	none
5487	239	?	Oscillatory	maybe	none	none	primary	none	?	none
5898	238	X	none? Sector?	none	none	none	none	total	?	none
5963	224	X	Oscillatory	none	none	none	primary	partial	?	none
5590	222	?	Oscillatory	none	none	none	primary	none	?	none
5544	215	?	Oscillatory	none	none	none	primary	none	?	none
5812	213	X	Oscillatory	none	none	none	none	partial	?	none
5770	210	X	Oscillatory	none	none	none	primary	partial	?	none
5839	193	X	Oscillatory	none	none	none	none	none	?	none
5609	188	X	Oscillatory	none	none	none	none	none	?	none
5681	175	X	Oscillatory	none	none	none	none	none	?	none
5853	158	X	Oscillatory	none	none	none	none	partial	?	none
5555	148	X	Oscillatory	none	none	none	none	partial	?	none
5402	136	X	Oscillatory	none	none	none	none	total	?	none
5444	135	?	Oscillatory	none	none	none	none	none	?	none
6036	135	X	Oscillatory	none	none	none	none	partial	?	none
5769	135	X	Oscillatory	none	none	none	none	none	?	none
5386	130	X	Oscillatory	none	none	none	none	partial	?	none
5705	129	X	Oscillatory	none	none	none	none	partial	?	none
5687	102	X	Oscillatory	none	none	none	none	partial	?	none
5489	100	X	Oscillatory	none	none	none	none	partial	?	none
5383	88	X	Oscillatory	none	none	none	none	partial	?	none
% microstructure:		94%		11%		7%	9%	~70%		2%

Total number of grains analyzed:	45
Number of "shocked grains":	42
% of shocked grains in V15-39:	94%

Sample	Area (sq. um)	Shocked?	Zonation Pattern Type	Planar Features	Microtwins	Curviplanar Features	Melt inclusions	Granular/polycrystalline texture	CPD	Displacement/shear
V15-16			*Oscillatory or Sector*		*1set or 2 sets*		note if polyphase or pods	partial (P) or total (T)		
36	8822	X	Oscillatory	X (+wedges)	2 sets	X	X	none	X	none
154	8302	X	Oscillatory	X	none	X	X	none	X	none
274	6732	X	Oscillatory	X (+wedges)	none	X	X	none	X	none
583	6590	X	indistinguishable	X	none	X	X	?	?	none
279	5839	X	Oscillatory	X (+wedges)	none	X	X	none	X	none
459	5024	X	Oscillatory	X	?	X	X	?	?	none
617	4932	X	Oscillatory	X (+wedges)	2 sets	X	X	Partial (along displacement)	X	X
272	4745	X	Oscillatory	?	?	X	X	none	?	Minor displacement
8	4639	X	Oscillatory	?	?	X	X	none	?	none
145	4611	X	Oscillatory	?	?	X	X	none	?	none
435	4508	X	Oscillatory	X	?	X	X	none	?	none
547	4370	X	Oscillatory	X	?	X	X	none	?	none
567	4091	X	Oscillatory	?	?	X	X	none	?	none
275	4075	X	Oscillatory	X	?	X	X	none	?	none
545	3931	X	Oscillatory	X	?	X	X	none	?	none
260	3839	X	Oscillatory	X	?	X	X	none	?	X
559	3835	X	Oscillatory	X	?	X	X	none	?	none
39	3828	X	Oscillatory	X	?	X	X	none	?	none
582	3799	X	Oscillatory	X	?	X	X	none	?	none
183	3704	X	Oscillatory	X	none	X	X	none	?	none
521	3629	X	Oscillatory	X	?	X	X	none	?	none
284	3536	X	Oscillatory	X	?	X	X	none	?	none
77	3503	X	Oscillatory	X	?	X	X	none	?	none
151	3342	X	Oscillatory	X	?	X	X	none	?	none
534	3240	X	Oscillatory	X	?	X	X	none	?	displacement along PF's?
252	2900	X	Oscillatory	X	?	X	X	none	?	none
493	2870	X	Oscillatory	X	?	X	X	none	?	none
471	2793	X	Oscillatory	X	?	X	X	none	?	X
460	2746	X	Oscillatory	X	?	X	X	none	?	none
565	2673	X	Oscillatory	X	?	X	X	none	?	X
127	2634	X	Oscillatory	X	?	X	X	none	?	none
91	2527	X	Oscillatory	X	?	X	X	none	?	none
276	2505	X	Oscillatory	X	?	X	X	none	?	none
167	2499	X	Oscillatory	X	?	X	X	none	?	none
445	2465	X	Oscillatory	X	?	X	X	none	?	none
297	2441	X	Oscillatory	X	?	X	X	none	?	none
604	2403	X	Oscillatory	X	?	X	X	none	?	none
482	2345	X	Oscillatory	X	?	X	X	none	?	none
507	2311	X	Oscillatory	X	?	X	X	none	?	none
305	2310	X	Oscillatory	X	?	X	X	none	?	none
388	2280	X	Oscillatory	X	?	X	X	none	?	none
121	2188	X	Oscillatory	X	?	X	X	none	?	none
231	2138	X	Oscillatory	X	?	X	X	none	?	none
205	2071	X	Oscillatory	X	?	X	X	none	?	none
130	2060	X	Oscillatory	X	?	X	X	none	?	none
506	2048	X	Oscillatory	X	?	X	X	none	?	none
513	1880	X	Oscillatory	X	?	X	X	none	?	none
527	1844	X	Oscillatory	X	?	X	X	none	?	none
% microstructure:		**100%**		**92%**		**100**	**100**	**2%**		**12.50%**

Total number of grains analyzed: **48**
Number of "shocked grains": **48**
% of shocked grains in V15-16: **100%**

Largest 50 grains (by area) analyzed

Sample V49-1	Area (sq. um)	Shocked?	Zonation Pattern Type *Oscillatory or Sector*	Planar Features	Microtwins *1set or 2 sets*	Curviplanar Features	Melt inclusions note if polyphase or pods	Granular/polycrystalline texture partial (P) or total (T)	CPD	Displacement/shear
3890	6396	X	Oscillatory	X	possible	X	along CP and PF	Partial along displacement?	X	X
3881	5050	X	Oscillatory	?	?	X	along CP	none	?	none
3481	2381	X	Oscillatory	X	possible	X	along CP and PF	Along displacement partial	?	X
2941	2178	?	Oscillatory	?	?	?	none (primary)	none	?	none
1145	1874	X	Oscillatory	?	?	X	along CP	none	?	none
4230	1741	X	Oscillatory	X	possible	X	along CP	none	?	X
3275	1716	X	Oscillatory	X	possible	X	along CP	none	?	none
1866	1622	X	Oscillatory	X	?	X	along CP	none	?	none
3785	1566	X	Oscillatory	X	?	X	along CP	none	?	none
1441	1539	X	Oscillatory	X	?	X (minor)	some along CP	none	?	none
3945	1503	X	Oscillatory	X	?	X	along CP	none	?	none
1517	1359	X	Oscillatory	X	?	X	along CP and PFs (as lenses along PFs)	none	?	none
1442	1276	X	Oscillatory	?	?	?	?	none	?	none
4258	1153	X	Oscillatory	X	?	X	along CP and PF (as lenses)	none	?	none
967	1041	X	Oscillatory	X	?	X	along CP and PF	none	?	none
3980	1031	X	Oscillatory	X	?	X	along CP	none	?	none
4030	951	X	Oscillatory	X	?	X	along CP primarily	none	?	none
1933	823	X	Oscillatory	X	?	X	along CP	none	?	none
4157	797	X	Oscillatory	X	?	X	along CP (very few)	none	?	none
2089	763	?	Oscillatory	?	?	?	possible along CP	none	?	none
541	715	X	Oscillatory	X	?	X	along CP (and possibly PF)	possible along displ.	?	X
3548	700	X	Oscillatory	X	?	none	none	none	?	none
1437	698	X	Oscillatory	X	?	?	none	none	?	none
3225	679	X	Oscillatory	X	?	X	along CP	none	?	X
2792	679	X	Oscillatory	?	?	X	along CP	none	?	none
2073	675	X	Oscillatory	X	?	X (very few)	very few along CP	none	?	none
2126	673	X	Oscillatory	ıpears as though ther	?	none	none	none	?	none
1253	667	X	Oscillatory	hard to say	?	X	minor along CP	none	?	none
2962	662	X	Oscillatory	X	?	X (minor)	along CP	none	?	none
2697	636	X	Oscillatory	ough to say, probabl	?	X	along CP (minor)	none	?	none
3909	606	X	Oscillatory	Looks like it	?	X	along CP	none	?	none
1083	511	X	Oscillatory	X	?	X	along CP	none	?	none
3260	496	X	Oscillatory	X?	?	X	along CP	none	?	none
929	483	?	Oscillatory	?	?	?	?	none	?	none
3709	460	X	Oscillatory	X	?	X	along Cp	none	?	none
1792	452	?	Oscillatory	?	?	?	?	none	?	none
945	424	X	Oscillatory	X	?	X	along CP in one area	none	?	none
4104	419	X	Oscillatory	X	?	X (minor)	some along CP	none	?	none
1181	328	X	Oscillatory	X	?	X	along CP	none	?	none
1874	323	X	Oscillatory	X	?	X	along CP	none	?	none
949	321	X	Oscillatory	X	possibly	X	along CP (few)	none	?	none
% microstructure:		90%		66%		80.50%	82.90%	7.30%		12.20%

Total number of grains analyzed: 41
Number of "shocked grains": 37
% of shocked grains in V49-1: 90.20%

All grains over 300 sq um noted

Sample	Area (sq. um)	Shocked?	Zonation Pattern Type	Planar Features	Microtwins	Curviplanar Features	Melt inclusions	Granular/polycrystalline texture	CPD	Displacement/shear
V15-46			*Oscillatory or Sector*		*1set or 2 sets*		note if polyphase or pods	partial (P) or total (T)		
725	8749	X	Oscillatory	X	none	some	hase in middle, traces of melt along pl	none	X	none
41	2562	X	Oscillatory	X	none obvious	X	primary and along fractures	possibly Partial in core	?	none
252	2484	X	Oscillatory	X	?	X	appear to be primary	none	?	none
607	2019	X	Oscillatory (faint)	X	?	X	along CF and PF	none	?	minor potentially
849	2013	X	Oscillatory	X	?	X	along CP	none	?	none
527	1871	X	Oscillatory	difficult to say	?	X	along CP	none	?	none
773	1825	X	Oscillatory	X	?	X	along CP	e (maybe some along 'eaten off' are	?	none
40	1787	X	Oscillatory	X	?	X	mostly along CP	none	?	none
36	1759	?	Oscillatory	none	none	none	none	none	?	none
477	1372	X	Oscillatory	X	?	X	along CP and PF	none	?	none
79	1102	X	Oscillatory	?	?	X	primary? along CP and possible PF	none	?	none
10	1006	X	Oscillatory	X (faint)	?	X	X along CP, very tiny	none	?	none
456	1004	X	Oscillatory	X	?	X	along CP	none	?	none
622	942	X	Oscillatory	X	?	X	along CP	none	?	none
515	908	X	Oscillatory	looks like it	?	X	along CP	none	?	none
295	850	?	Oscillatory (very tight)	none	none	none	none	none	?	none
743	843	X	Oscillatory	X	?	X	along CP adn PF	none	?	none
90	840	X	Oscillatory	?	?	X	along CP	none	?	none
842	803	X	Oscillatory	X	?	X	along Cp	none	?	none
200	801	?	Oscillatory	none	none	none	none	none	?	none
431	769	X	Oscillatory	X	?	X	hard to say	possibly some along displacement	?	X
400	767	X	Oscillatory	none	none	X	along CP	none	?	none
255	724	X	Oscillatory	X	?	X	along PF and Cp	none	?	a displacement on margins along PF's
608	682	X	Oscillatory	X	?	X	along PF and CP	none	?	along CP
169	620	X	Oscillatory	X	?	X	along PF and Cp	none	?	none
880	593	X	Oscillatory	X	?	X	X along CP and PF (and primary)	none	?	X (minor)
820	574	X	Oscillatory	X	?	X	along both PF and CP	none	?	none
727	544	X	Oscillatory	X	?	X	along PF and CP	none	?	none
256	542	X	Oscillatory	X	?	X	along Cp and PF	none	?	none
311	538	X	Oscillatory	X	?	X	along cp and pf	none	?	none
885	537	X	Oscillatory	X	?	X	along CP mostly (very small)	none	?	none
438	495	X	Oscillatory	X	?	?	along PF's	none?	?	X (minor)
58	483	X	oscillatory	X	?	X	along Cp and Pf	none	?	none
244	481	X	oscillatory	X (minor)	?	X (minor)	Very few along CP and Pf	none	?	none
96	472	X	oscillatory	X (minor)	?	X (minor)	few along CP and PF	none	?	none
423	468	X	Oscillatory	?	?	X	along CP (very few and very small)	none	?	none
700	447	X	Oscillatory	X	?	X	along CP	none	?	?
510	431	?	Oscillatory	?	?	?	?	none	?	none
144	397	?	Oscillatory	?	?	?	?	none	?	none
617	389	X	Oscillatory	X	(probably)	X	along CP and PF	none	?	X
360	378	X	Oscillatory	none	?	X	along CP	none	?	none
223	376	?	Oscillatory	?	?	X	along CP?	none	?	none
857	373	X	Oscillatory	X	?	?	along CP?	none	?	none
195	372	X	Oscillatory	X	?	X	along CP	none	?	X (minor)
501	354	X	Oscillatory	X	?	X	along CP	none	?	none
329	346	X	Oscillatory	X	?	X	along CP	none	?	none
699	346	?	Oscillatory	?	?	?	?	none	?	none
189	340	X	Oscillatory	X	?	X	along CP and PF?	none	?	none
% microstructure:		**85%**		**73%**		**83%**	**87.50%**	**4%**		**17%**

Total number of grains analyzed:	**48**
Number of "shocked grains":	**41**
% of shocked grains in V15-46:	**85**

Sample	Area (sq. um)	Shocked?	Zonation Pattern Type	Planar Features	Microtwins	Curviplanar Features	Melt inclusions	Granular/polycrystalline texture	CPD	Displacement/shear
V-62			*Oscillatory or Sector*		*1set or 2 sets*		note if polyphase or pods	partial (P) or total (T)		
2185	43050	X	Sector	X	?	X	X	none	?	none
3313	19908	X	Oscillatory	X	X	X	X (with pods)	none	X	none
3448	18414	X	Both	X	?	X	X (with pods)	none	?	none
3719	14483	X	Both	X	X	X	X (with pods)	none	?	none
3440	12007	X	Sector	X	X	X	X (with pods)	some recrystallization along displacement	X	X
1676	10997	X	Both	X	?	X	X	none	?	none
3445	7133	X	Both	X	X	X	X	none	?	none
123	6809	X	Both	? possible	none	X	X	none	X	none
209	4962	X	Sector	X	?	X	X	some recrystallization along displacement	?	X *minor
295	4799	X	Both	X	?	X	X	none	?	none
299	4797	X	Both	X	none	X	X	none	?	none
296	4589	X	Both	?	?	X	X	none	?	none
1637	3787	X	Both	X	?	X	X	none	?	none
1825	3746	X	difficult to say	?	?	X	X	X	?	none
860	2994	?	Both	?	?	?	?	none	?	none
1849	2727	X	?	X	?	X (minor)	X (minor)	none	?	none
297	2590	X	Both	X	?	X	X	none	?	none
3443	2046	X	Sector	?	?	X	X	none	?	none
1639	1830	X	Both	?	?	X	X	none	?	X
257	1826	X	Oscillatory	X	?	X	X	none	?	none
1638	1659	X	Oscillatory	possibly	?	X	X	none	?	X
1810	1512	X	?	X	?	X	X	none	?	X
1668	1408	X	Oscillatory	X	?	X	X	none	?	X
647	1092	X	Sector	?	?	X	X	at edges of grain, associated with melt	?	X
3690	1077	X	hard to tell	none	none	none	none	granular zircon	?	none
1	990	X	hard to tell	none	none	none	none	?	?	none
1632	983	X	Oscillatory	?	?	X	X	none	?	none
3675	936	X	Oscillatory	?	?	X	X	none	?	none
3676	838	X	Both	?	?	X	X	none	?	none
1811	716	X	can't tell	none	none	X	X	none	?	none
256	656	X	Oscillatory	?	?	X	X	none	?	none
122	635	X	Sector?	?	?	X	X	none	?	none
1634	632	X	Oscillatory	?	?	X	X	none	?	none
% microstructure:		**97%**		**55%**		**91%**	**91%**	**15%**		**15%**

Total number of grains analyzed: **33**
Number of "shocked grains": **32**
% of shocked grains in V-62 **97%**

Sample V15-55	Area (sq. um)	Shocked?	Zonation Pattern Type *Oscillatory or Sector*	Planar Features	Microtwins *1set or 2 sets*	Curviplanar Features	Melt inclusions note if polyphase or pods	Granular/polycrystalline texture partial (P) or total (T)	CPD	Displacement/shear
F397	2794	X	Oscillatory	X (open fractures)	?	?	none	none	?	none, (possibly some along planar frac)
1147	2140	unshocked	Oscillatory	none	none	none	none	none	?	none
1171	1657	unshocked	Oscillatory	none	none	none	primary	none	?	X
77	1511	unshocked	Oscillatory	?	?	doesn't appear so	primary	none	?	none
904	624	X	Oscillatory	?	?	?	none	none	?	X
415	749	X	Oscillatory	X	?	?	primary	none	?	none
494	1035	X	Oscillatory	X	?	?	none	none	?	X
1138	1117	X	Oscillatory?	X	?	?	none	none	?	none
272	729	?	Oscillatory	?	?	?	none	none	?	none
267	248	X	Oscillatory	X	?	?	none	none	?	none
308	435	unshocked	Oscillatory	none	none	none	none	none	?	none
274	394	unshocked	Oscillatory	none	none	none	none	none	?	none
452	701	unshocked	Oscillatory	none	none	none	none	none	?	none
1178	534	unshocked	Oscillatory	?	none	none	none	none	?	missing half the grain, not sure if polished off
101	438	X	Oscillatory	X	none	none	none	none	?	none
440	599	unshocked	Oscillatory	none	none	none	none	none	?	none
1288	224	X	Oscillatory	X	?	none	none	none	?	none
1173	198	X	Oscillatory	X	?	none	none	none	?	none
787	471	unshocked	Oscillatory	?	?	?	none	none	?	none
32	333	unshocked	Oscillatory	none	none	none	none	none	?	none
700	215	unshocked	Oscillatory	none	none	none	primary	none	?	none
1159	353	unshocked	Oscillatory	none	none	none	none	none	?	none
1156	546	X	Oscillatory	X	?	none	none	none	?	none
273	256	unshocked	Oscillatory	?	?	none	none	none	?	none
1108	272	X	Oscillatory	X	?	?	none	none	?	none
133	210	X	Oscillatory	?	?	?	none	none	?	X
348	389	X	Oscillatory	X	?	?	none	none	?	none
421	610	X	difficult to say	none	none	none	none	none	?	X
1	172	unshocked	Oscillatory	none	none	none	none	none	?	none
180	583	unshocked	Oscillatory	?	?	none	none	none	?	none
1213	467	X	Oscillatory	?	?	none	none	none	?	X
132	273	X	Oscillatory	X	?	none	none	none	?	none
138	374	X	Oscillatory	X	?	?	none	none	?	none
1176	541	unshocked	Oscillatory	none	none	?	?	none	?	none
322	180	unshocked	Oscillatory	?	?	none	none	none	?	none
1053	298	unshocked	Oscillatory	?	?	none	none	none	?	none
% microstructure:		**50%**		**39%**		**0%**	**0%**	**0%**		**17%**

Total number of grains analyzed:	**36**
Number of "shocked grains":	**18**
% of shocked grains in V-62	**50%**

Appendix E: Quantitative Energy Dispersive Spectroscopy Results

V2-1 Quantitative EDS Results

V2-1

Site: Site of Interest 2

Processing option : Oxygen by stoichiometry (Normalised)

All results in weight%

Spectrum	Mg	Al	Si	Fe	Zr	O	Total	
Spectrum 1				14.36		51.3	34.35	100
Spectrum 2				14		51.85	34.14	100
Spectrum 3				14.19		51.55	34.25	100
Spectrum 4		10.3	5.5	18.16	26.17		39.86	100
Spectrum 5		10.53	5.42	19.33	24.05		40.67	100
Spectrum 6		9.72	6.14	22.78	18.3		43.06	100
Spectrum 7		9.78	7.13	23.89	14.92		44.27	100
Spectrum 8		9.64	7.19	24.99	13.19		44.99	100
Spectrum 9		10.41	5.28	19.93	23.43		40.96	100
Spectrum 10		9.93	4.7	21.3	22.62		41.46	100
Spectrum 11		9.91	5.56	20.84	22.14		41.55	100
Spectrum 12		10.63	6.08	20.49	21.02		41.77	100
Spectrum 13		11.04	5.98	20.9	19.96		42.12	100
Spectrum 14		9.95	6.27	22.48	18.33		42.98	100
Spectrum 15		11.2	5.87	20.17	21.14		41.62	100
Spectrum 16		11.83	5.79	20.95	19.16		42.28	100
Spectrum 17		10.21	6.07	20.2	22.07		41.45	100
Spectrum 18		9.59	12.5	18.08	16.95		42.88	100
Spectrum 19		10.29	12.21	20.73	12.05		44.71	100
Spectrum 20		10.37	9.59	21.62	14.33		44.09	100
Spectrum 21		9.09	9.99	15.48	25.61		39.84	100
Spectrum 22		9.45	11.19	16.48	21.72		41.16	100
Spectrum 23		8.86	10.82	16.37	23.21		40.75	100
Spectrum 24		8.1	5.18	20.1	12.75	12.87	41	100
Spectrum 25		7.69	4.79	20.79	14.44	11.21	41.08	100
Spectrum 26		6.89	5.26	18.76	14.64	14.56	39.89	100
Spectrum 27		11.51	6	22.53	16.61		43.35	100
Spectrum 28		10.67	6.32	24.02	14.75		44.24	100
Spectrum 29		11.24	5.53	23.69	15.72		43.81	100
Spectrum 30		5.15	5.25	18.82	11.49	19.63	39.67	100
Spectrum 31		4.9	3.9	18.66	9.94	23.54	39.06	100
Spectrum 32		5.01	4.28	21.26		28.22	41.23	100
Spectrum 33		9.74	5.82	19.45	24.3		40.7	100
Spectrum 34		10.53	5.68	21.24	20.51		42.05	100
Spectrum 35		10.13	5.12	21.9	20.74		42.11	100
Spectrum 36			19.75	10.41		29.92	39.92	100
Spectrum 37			19.56	10.47		30.09	39.88	100
Spectrum 38			17.77	10.3		32.86	39.07	100
Spectrum 39		10.06	6.16	19.35	23.53		40.89	100
Spectrum 40		10.21	6.95	21.01	19.42		42.4	100
Spectrum 41		10.27	6.79	19.26	22.49		41.19	100
Spectrum 42				14.56		50.97	34.47	100
Spectrum 43				14.99		50.28	34.72	100
Spectrum 44				13.89		52.03	34.08	100
Max.		11.83	19.75	24.99	26.17	52.03	44.99	
Min.		4.9	3.9	10.3	9.94	11.21	34.08	

Site: Site of Interest 3

Processing option : Oxygen by stoichiometry (Normalised)

All results in weight%

Spectrum	In stats.	Na	Mg	Al	Si	K	Ca	Fe	Zr	O	Total	
Spectrum 1	Yes					14.15				51.63	34.23	100
Spectrum 2	Yes					13.83				52.13	34.04	100
Spectrum 3	Yes					13.82				52.15	34.03	100
Spectrum 4	Yes								77.73		22.27	100
Spectrum 5	Yes								77.73		22.27	100
Spectrum 6	Yes								77.73		22.27	100
Spectrum 7	Yes		5.32		12.49	28.68		5.64			47.88	100
Spectrum 8	Yes		5.41		13.17	31.71					49.72	100
Spectrum 9	Yes		5.43		11.94	29.68		4.73			48.21	100
Spectrum 10	Yes			6.98	6.75	16.05	7.52		25.09		37.61	100
Spectrum 11	Yes			7.11	7.15	17.27	7.84		22.01		38.62	100
Spectrum 12	Yes			7.77	6.64	17.5	7.29		22.06		38.76	100
Spectrum 13	Yes				9.13	31.44	12.86				46.57	100
Spectrum 14	Yes				9.19	31.26	13.09				46.46	100
Spectrum 15	Yes				9.62	31.48	12.02				46.88	100
Spectrum 16	Yes			6.42	6.75	16.38			15.75	15.76	38.93	100
Spectrum 17	Yes			6	6.09	16.45			15.4	17.43	38.63	100
Spectrum 18	Yes			5.75	6.3	14.89			16.62	18.76	37.69	100
Spectrum 19	Yes			9.91	8.11	20.56			18.87		42.56	100
Spectrum 20	Yes			10.13	7.37	22.06			17.17		43.27	100
Spectrum 21	Yes			10.13	7.35	24.43			13.27		44.83	100
Spectrum 22	Yes			10.5	5.65	19.89			22.82		41.14	100
Spectrum 23	Yes			9.67	5.46	19.92			24.11		40.83	100
Spectrum 24	Yes			10.18	5.38	22.16			19.85		42.42	100
Spectrum 25	Yes				50.14	2.46					47.4	100
Spectrum 26	Yes				50.55	2.09					47.35	100
Spectrum 27	Yes				50.48	2.16					47.36	100
Spectrum 28	Yes		5.23		11.93	30.39		3.87			48.59	100
Spectrum 29	Yes		4.71		12.2	30.2		4.28			48.61	100
Spectrum 30	Yes		4.56		11.88	31.11		3.47			48.98	100
Spectrum 31	Yes			7.11	6.59	16.88	8.68		22.69		38.05	100
Spectrum 32	Yes			7.26	6.45	16.45	8.04		24.01		37.78	100
Spectrum 33	Yes			7.84	6.79	17.83	7.81		20.68		39.04	100
Spectrum 34	Yes			7.05	6.89	18.2	6.18		22.48		39.21	100
Spectrum 35	Yes			7.26	6.82	17.32	6.72		23.27		38.61	100
Spectrum 36	Yes			6.88	6.68	17.26	6.97		23.83		38.38	100
Spectrum 37	Yes				8.88	32.23	11.85				47.04	100
Spectrum 38	Yes				8.95	32.03	12.09				46.93	100
Spectrum 39	Yes				9.33	32.06	11.45				47.16	100
Max.			5.43	10.5	50.55	32.23	13.09	5.64	77.73	52.15	49.72	
Min.			4.56	5.75	5.38	2.09	6.18	3.47	13.27	15.76	22.27	

Site: Site of Interest 4

Processing option : Oxygen by stoichiometry (Normalised)

All results in weight%

Spectrum	In stats.	Mg	Al	Si	Fe	Zr	O	Total	
Spectrum 1	Yes				14.88		50.46	34.66	100
Spectrum 2	Yes				14.6		50.91	34.49	100
Spectrum 3	Yes		4.55	8.88	14.16	19.07	15.45	37.9	100
Spectrum 4	Yes		5.3	9.09	14.31	13.13	19.63	38.53	100
Spectrum 5	Yes		4.98	8.01	13.84	18.27	17.39	37.51	100
Spectrum 6	Yes		9.19	10.01	16.69	23.43		40.68	100
Spectrum 7	Yes		9.75	9.78	16.71	23.01		40.75	100
Spectrum 8	Yes		9.88	9.55	16.33	23.82		40.42	100
Spectrum 9	Yes		9.18	9.28	17.6	23.01		40.93	100
Spectrum 10	Yes		8.97	9.89	17.45	22.63		41.06	100
Spectrum 11	Yes		9.54	9.55	17.63	22.1		41.18	100
Spectrum 12	Yes		10.77	7.04	18.21	23.23		40.75	100
Spectrum 13	Yes		10.08	7.32	18.81	22.71		41.08	100
Spectrum 14	Yes		9.55	6.82	18.9	23.98		40.75	100
Spectrum 15	Yes		7.64	15.37	16.21	18.35		42.43	100
Spectrum 16	Yes		7.48	15.12	16.73	18.06		42.61	100
Spectrum 17	Yes		8.15	15.49	16.67	16.76		42.93	100
Spectrum 18	Yes		9.35	6.54	22.39	18.84		42.88	100
Spectrum 19	Yes		7.88	6.3	20.91	15.51	7.65	41.74	100
Spectrum 20	Yes		7.06	5.54	19.49	17.6	9.98	40.32	100
Spectrum 21	Yes		9.35	8.45	23.19	14.71		44.3	100
Spectrum 22	Yes		8.47	7.96	24.12	15		44.44	100
Spectrum 23	Yes		8.44	8.06	26.03	11.73		45.74	100
Spectrum 24	Yes		5.72	20.9	19.15		7.43	46.79	100
Spectrum 25	Yes		6.68	18.75	19.59		8.58	46.4	100
Spectrum 26	Yes		6.4	18.19	20.04		8.99	46.38	100
Spectrum 27	Yes		4.89	5.66	16.85	14.74	19.39	38.47	100
Spectrum 28	Yes		4.91	4.3	17.57	10.78	23.91	38.54	100
Spectrum 29	Yes		4.89	3.89	17.35	13.03	22.7	38.14	100
Max.			10.77	20.9	26.03	23.98	50.91	46.79	
Min.			4.55	3.89	13.84	10.78	7.43	34.49	

V09-237 Quantitative EDS Results

Site: Site of Interest 2

Processing option : Oxygen by stoichiometry (Normalised)

All results in weight%

Spectrum	In stats.	Na	Al	Si	K	Ca	Zr	O	Total
Spectrum 1	Yes				14.09			51.72	34.19	100
Spectrum 2	Yes				13.82			52.14	34.04	100
Spectrum 3	Yes				13.44			52.75	33.81	100
Spectrum 4	Yes			9.63	31.97	11.13			47.27	100
Spectrum 5	Yes		1.14	9.31	31.55	11.11			46.89	100
Spectrum 6	Yes			9.66	32.37	10.37			47.6	100
Spectrum 7	Yes			10.55	32.83	8.17			48.45	100
Spectrum 8	Yes		1.27	9.5	33.6	7.03			48.61	100
Spectrum 9	Yes			9.38	34.56	6.92			49.14	100
Spectrum 10	Yes			11.39	33.69	5.32			49.6	100
Spectrum 11	Yes		1.14	9.86	35.34	3.52			50.15	100
Spectrum 12	Yes			10.82	35.39	3.19			50.6	100
Spectrum 13	Yes			11.83	36.3				51.87	100
Spectrum 14	Yes			11.83	36.29				51.87	100
Spectrum 15	Yes			12.28	35.89				51.82	100
Spectrum 16	Yes		0.83	10.1	34	5.85			49.21	100
Spectrum 17	Yes			9.41	35.45	5.29			49.85	100
Spectrum 18	Yes			10.43	35.03	4.45			50.09	100
Spectrum 19	Yes			12.56	35.65				51.79	100
Spectrum 20	Yes			11.55	36.54				51.91	100
Spectrum 21	Yes			11.75	36.36				51.88	100
Spectrum 22	Yes			12.85	35.39				51.75	100
Spectrum 23	Yes			12.38	35.81				51.81	100
Spectrum 24	Yes			13.1	35.18				51.73	100
Spectrum 25	Yes		1.57	9.31	33.89	6.48			48.76	100
Spectrum 26	Yes		1.34	9.62	34.07	5.92			49.05	100
Spectrum 27	Yes		1.07	10.06	34.16	5.36			49.34	100
Spectrum 28	Yes		6.33	12.58	31.64				49.44	100
Spectrum 29	Yes		6.15	12.03	32.24				49.57	100
Spectrum 30	Yes		5.96	11.44	30.64		3.44		48.52	100
Spectrum 31	Yes			10.72	37.28				52	100
Spectrum 32	Yes			11.98	36.16				51.86	100
Spectrum 33	Yes			11.27	36.79				51.94	100
Spectrum 34	Yes		3	12.62	33.71				50.67	100
Spectrum 35	Yes		2.63	12.81	33.77				50.79	100
Spectrum 36	Yes		2.74	12.18	34.26				50.82	100
Spectrum 37	Yes			7.81	28.53	6.36		12.24	45.05	100
Spectrum 38	Yes			8.07	28.89	4.49		12.99	45.56	100
Spectrum 39	Yes			7.48	31.06	3.6		11.17	46.69	100
Spectrum 40	Yes		4.24	8.11	28.19			13.81	45.65	100
Spectrum 41	Yes		3.86	7.82	27.27			16.05	45	100
Spectrum 42	Yes		3.05	8.01	28.44			14.74	45.76	100
Spectrum 43	Yes			6.96	30.56			15.9	46.58	100
Spectrum 44	Yes			6.84	29.53			17.71	45.93	100
Spectrum 45	Yes			7.91	31.31			13.39	47.4	100
Max.			6.33	13.1	37.28	11.13	3.44	52.75	52	
Min.			0.83	6.84	13.44	3.19	3.44	11.17	33.81	

Processing option : Oxygen by stoichiometry (Normalised)

All results in weight%

Spectrum	In stats.	Na	Al	Si	K	Ca	Zr	Pt	O	Total
Spectrum 1	Yes				13.96			51.92	34.12	100
Spectrum 2	Yes				14.86			50.5	34.64	100
Spectrum 3	Yes		0.87	9.06	31.98	11.05			47.05	100
Spectrum 4	Yes			9.21	32.89	10.17			47.74	100
Spectrum 5	Yes			9.38	31.5	12.35			46.76	100
Spectrum 6	Yes			9.33	31.82	11.87			46.98	100
Spectrum 7	Yes			8.9	31.83	12.54			46.74	100
Spectrum 8	Yes		0.82	8.87	31.8	11.72			46.8	100
Spectrum 9	Yes			9.43	31.79	11.77			47.01	100
Spectrum 10	Yes			9.23	31.96	11.79			47.03	100
Spectrum 11	Yes			9.28	33.1	9.69			47.94	100
Spectrum 12	Yes			9.38	32.49	10.6			47.53	100
Spectrum 13	Yes			9.62	31.95	11.18			47.25	100
Spectrum 14	Yes			9.29	31.42	12.64			46.65	100
Spectrum 15	Yes		1.29	8.36	31.64	12.26			46.44	100
Spectrum 16	Yes		1	9.21	31.86	10.87			47.06	100
Spectrum 17	Yes			8.81	31.37	13.49			46.33	100
Spectrum 18	Yes			9.22	31.69	12.26			46.82	100
Spectrum 19	Yes			8.89	31.88	12.45			46.78	100
Spectrum 20	Yes			10.12	34.66	5.58			49.63	100
Spectrum 21	Yes			9.97	35.23	4.82			49.99	100
Spectrum 22	Yes			9.99	35.32	4.62			50.07	100
Spectrum 23	Yes		0.92	9.45	31.3	11.59			46.75	100
Spectrum 24	Yes			9.58	31.92	11.3			47.2	100
Spectrum 25	Yes			9.43	32.64	10.26			47.67	100
Spectrum 26	Yes		0.92	9.68	32.53	9.03			47.84	100
Spectrum 27	Yes		0.94	8.84	29.82	10.02		4.57	45.81	100
Spectrum 28	Yes		1.03	8.81	32.97	9.49			47.7	100
Spectrum 29	Yes			10.84	37.17				51.99	100
Spectrum 30	Yes			10.77	37.24				52	100
Spectrum 31	Yes			11.2	36.85				51.95	100
Spectrum 32	Yes		2.16	8.59	32.4	9.59			47.26	100
Spectrum 33	Yes		1.73	9.18	31.44	10.83			46.81	100
Spectrum 34	Yes		1.32	10.03	31.94	9.1			47.62	100
Spectrum 35	Yes		2.75	9.83	33.4	5.2			48.82	100
Spectrum 36	Yes		2.48	9.57	33.97	4.91			49.08	100
Spectrum 37	Yes		2.36	9.73	33.44	5.73			48.74	100
Spectrum 38	Yes		1.32	8.73	31.61	11.73			46.63	100
Spectrum 39	Yes		1.4	9.45	31.04	11.51			46.61	100
Spectrum 40	Yes		1.2	9.15	31.6	11.19			46.85	100
Spectrum 41	Yes		0.97	11.42	36.05				51.56	100

Spectrum 42 Yes		11.66	36.45					51.89	100
Spectrum 43 Yes		12.12	36.04					51.84	100
Spectrum 44 Yes	6.67	12.09	31.86					49.38	100
Spectrum 45 Yes	6.95	11.48	30.28		2.98			48.31	100
Spectrum 46 Yes	7.04	12.2	31.53					49.23	100
Spectrum 47 Yes	5.5	9.69	29.18			8.78		46.85	100
Spectrum 48 Yes	5.12	10.12	28.14			10.19		46.42	100
Spectrum 49 Yes	5.47	9.27	30.68			7.02		47.56	100
Spectrum 50 Yes	5.7	8.75	29.71			9.05		46.79	100
Spectrum 51 Yes	5.61	8.59	29.44			9.79		46.57	100
Spectrum 52 Yes	5.09	8.49	29.71			10.03		46.68	100
Spectrum 53 Yes	1.05	9.23	30.8	12.66				46.26	100
Spectrum 54 Yes		9.06	32.03	11.93				46.99	100
Spectrum 55 Yes		9.13	32.35	11.25				47.28	100
Spectrum 56 Yes			14.34			51.31		34.34	100
Spectrum 57 Yes	2.49	10.13	30.83	9.59				46.96	100
Spectrum 58 Yes	1.77	9.24	31.45	10.7				46.85	100
Spectrum 59 Yes	2.05	9.59	31.45	9.82				47.09	100
Spectrum 60 Yes	7.72	10.06	33					49.23	100
Spectrum 61 Yes	8.33	10.03	32.64					49	100
Spectrum 62 Yes	8.1	10.35	32.5					49.05	100
Spectrum 63 Yes	5.44	9.8	31.46	5.69				47.61	100
Spectrum 64 Yes	4.76	11.02	31.17	5.06				48	100
Spectrum 65 Yes	4.63	10.32	31.3	6.05				47.69	100
Spectrum 66 Yes	0.91	9.29	31.04	12.31				46.46	100
Spectrum 67 Yes	0.98	9.28	31.08	12.16				46.49	100
Spectrum 68 Yes		9.21	31.38	12.84				46.57	100
Spectrum 69 Yes	0.89	9.02	31.4	12.1				46.58	100
Spectrum 70 Yes	0.84	9.46	31.18	11.86				46.66	100
Spectrum 71 Yes	0.94	9.48	30.61	12.72				46.24	100
Spectrum 72 Yes	2.67	10.35	32.26	6.51				48.21	100
Spectrum 73 Yes	2.83	10.53	33.02	4.68				48.93	100
Spectrum 74 Yes	2.6	10.05	33.35	5.12				48.88	100
Spectrum 75 Yes	5.3	10.83	27.98			9.27		46.61	100
Spectrum 76 Yes	5.39	9.84	30.55				7.54	46.67	100
Spectrum 77 Yes	5.05	8.94	28.32			11.63		46.06	100
Spectrum 78 Yes		9.61	31.55	11.91				46.93	100
Spectrum 79 Yes		9.6	31.79	11.49				47.11	100
Spectrum 80 Yes		9.41	32.26	10.97				47.36	100
Max.	8.33	12.2	37.24	13.49	2.98	51.92	7.54	52	
Min.	0.82	8.36	13.96	4.62	2.98	4.57	7.54	34.12	

Processing option : Oxygen by stoichiometry (Normalised)

All results in weight%

Spectrum	In stats.	Na	Al	Si	K	Ca	Zr	O	Total	
Spectrum 1	Yes				15.16			50.02	34.82	100
Spectrum 2	Yes				14.15			51.62	34.23	100
Spectrum 3	Yes			9.01	31.7	12.58			46.71	100
Spectrum 4	Yes			9.23	30.88	13.7			46.19	100
Spectrum 5	Yes			9.1	31.54	12.73			46.63	100
Spectrum 6	Yes		5.6	10.27	34.15				49.99	100
Spectrum 7	Yes		5.01	10.12	34.65				50.22	100
Spectrum 8	Yes		4.35	10.18	33.3	3.04			49.13	100
Spectrum 9	Yes		7.82	9.41	33.5				49.26	100
Spectrum 10	Yes		8.25	9.85	32.85				49.06	100
Spectrum 11	Yes		7.9	9.52	33.36				49.22	100
Spectrum 12	Yes		1.01	8.99	30.99	12.75			46.26	100
Spectrum 13	Yes		0.92	9.16	31.04	12.5			46.38	100
Spectrum 14	Yes			9.84	32.1	10.58			47.48	100
Spectrum 15	Yes			9.25	32.97	9.96			47.82	100
Spectrum 16	Yes			9.67	32.1	10.84			47.39	100
Spectrum 17	Yes			8.75	32.31	11.92			47.03	100
Spectrum 18	Yes			9.09	32.71	10.68			47.53	100
Spectrum 19	Yes			9.34	30.95	13.39			46.31	100
Spectrum 20	Yes			9.74	30.46	13.65			46.15	100
Spectrum 21	Yes			11.66	36.45				51.89	100
Spectrum 22	Yes			11.68	36.43				51.89	100
Spectrum 23	Yes			10.8	37.21				51.99	100
Spectrum 24	Yes		6.58	11.42	32.51				49.49	100
Spectrum 25	Yes		6.06	11.62	30.45		3.37		48.49	100
Spectrum 26	Yes		6.14	11.89	29.73		4.04		48.2	100
Spectrum 27	Yes		6.46	10.45	31.08		3.61		48.4	100
Spectrum 28	Yes		6.85	11.84	29.58		3.66		48.07	100
Spectrum 29	Yes		7.05	11.5	32.15				49.31	100
Spectrum 30	Yes			9.15	32.05	11.75			47.05	100
Spectrum 31	Yes			9.33	30.2	14.74			45.72	100
Spectrum 32	Yes			9.01	32.09	11.9			47	100
Spectrum 33	Yes			9.5	31.49	12.19			46.82	100
Spectrum 34	Yes			9.05	31.21	13.4			46.34	100
Spectrum 35	Yes			9.94	31.64	11.24			47.18	100
Spectrum 36	Yes			9.59	31.4	12.21			46.8	100
Spectrum 37	Yes		0.95	9.37	31.17	11.9			46.61	100
Spectrum 38	Yes		1.25	8.96	31.24	12.1			46.46	100
Spectrum 39	Yes		6.55	11.26	30.57		3.23		48.4	100
Spectrum 40	Yes		6.93	11.89	31.87				49.3	100
Spectrum 41	Yes		6.59	11.29	30.52		3.21		48.39	100
Spectrum 42	Yes		7.72	11.31	31.89				49.08	100
Spectrum 43	Yes		7.4	10.74	32.59				49.26	100
Spectrum 44	Yes		7.21	10.69	32.76				49.34	100
Spectrum 45	Yes		3.62	8.69	31.94	8.6			47.14	100
Spectrum 46	Yes		3.52	9.54	31.86	7.53			47.55	100
Spectrum 47	Yes		3.43	9.23	32.42	7.13			47.79	100
Spectrum 48	Yes			15.36	29.23	7.02			48.39	100
Spectrum 49	Yes			14.69	30.04	6.62			48.65	100
Spectrum 50	Yes			15.34	29.7	6.22			48.75	100
Spectrum 51	Yes			7.63	28.9	9.41		9.18	44.87	100
Spectrum 52	Yes		0.99	7.13	27.75	9.56		10.59	43.97	100
Spectrum 53	Yes		0.74	6.59	27.42	11.28		10.59	43.38	100
Spectrum 54	Yes			8.55	32.01	12.77			46.68	100
Spectrum 55	Yes		1.01	7.9	29.62	10.62		5.6	45.26	100
Spectrum 56	Yes		1.25	9.52	31.4	10.91			46.91	100
Max.			8.25	15.36	37.21	14.74	4.04	51.62	51.99	
Min.			0.74	6.59	14.15	3.04	3.21	5.6	34.23	

Appendix F: Energy Dispersive Spectroscopy Glass Standards

Standard ID	Si	O	Na	Mg	Al	P	K
K-411	25.38±0.09	42.37±0.15		8.85±0.12			
K-412	21.20±0.09	42.76±0.18		11.66±0.12	4.91±0.11		
K-495	23.08	31.93			10.58		
K-496		53.79		5.45	6.05	34.71	
K-373	31.85	42.34	10.43				
K-375	31.83	42.32	10.42				
NMNH Rhyolite (VG-568)	35.8573	49.55894	2.782	>0.0603	6.3828		3.5614
NMNH Basalt (VG-99)	23.81	43.5474	1.97	3.0636	6.61	0.1658	0.68

Table F-1 cont'd:

Ca	Mn	Fe	Zn	Ba	U	Ti	H	Total
11.06±0.14		11.21±0.16						98.9±0.3
10.90±0.14		7.74±0.16						99.2±0.3
			3.07					100
								100
			4.94	10.38	0.054			100
			4.94	10.37	0.11			100
0.3574	0.0232	0.9575		negligible		0.0719	0.10656	99.659
6.6467	0.1162	10.3402				2.43	0.017	99.39

Table F-1: Glass standard compositions. Standards provided by SPI supplies and C.M. Taylor Company. See Jarosewich (2012) for further information on many of these standards.

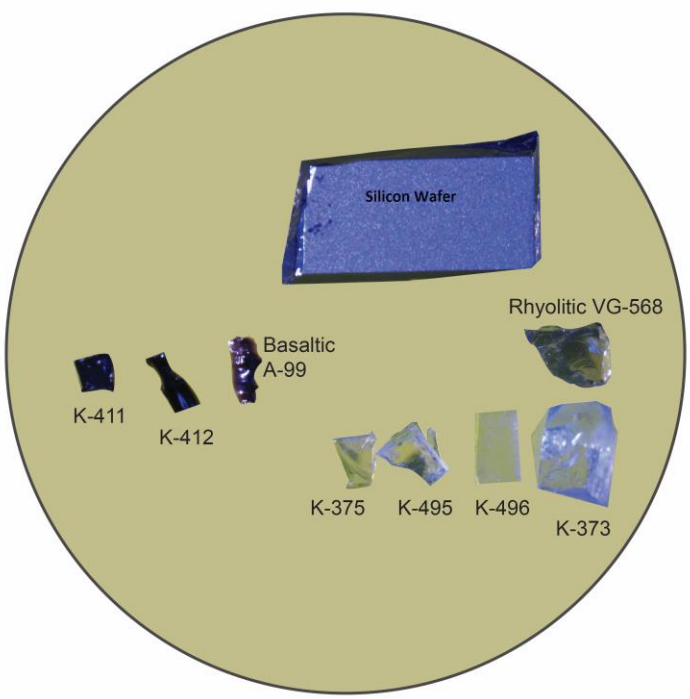

Figure F-1: Standard epoxy mount (bottom view), with silicon chip used for the carbon coat thickness measurements done on both the samples and standards.

Curriculum Vitae

Name: Connor Davis

Post-secondary Education and Degrees:

The University of Western Ontario
London, Ontario, Canada
2010-2014 BSc. Geology for Professional Registration

The University of Western Ontario
London, Ontario, Canada
2014-2016 MSc. Geology

Honours and Awards:

Dean's Honours List (2014)

Related Work Experience

Graduate Teaching Assistant
The University of Western Ontario
2014-2016

CSA-ASTRO Summer Student
The University of Western Ontario
2014